EXPERIMENTAL INVESTIGATION OF AIR-COOLED CONDENSERS

A Thesis
Presented to
The Academic Faculty

by

Taylor Steven Kunke

In Partial Fulfillment
of the Requirements for the Degree
Master of Science in the
School of Mechanical Engineering

Georgia Institute of Technology
August 2017

EXPERIMENTAL INVESTIGATION OF AIR-COOLED CONDENSERS

Approved by:

Dr. Srinivas Garimella, Advisor
School of Mechanical Engineering
Georgia Institute of Technology

Dr. Peter Loutzenhiser
School of Mechanical Engineering
Georgia Institute of Technology

Dr. Sheldon Jeter
School of Mechanical Engineering
Georgia Institute of Technology

Date Approved: July 27th, 2017

ACKNOWLEDGEMENTS

First and foremost, I would like to thank my adviser, Dr. Garimella, for his relentless support throughout the last two years. Dr. Garimella has challenged me to produce the highest quality of work, provided countless learning opportunities, and advocated on my behalf numerous times. While my time at STSL has come to an end, I look forward to taking the skills and abilities I have gained with me on to the next adventure. I would also like to thank EPRI and NSF for their project funding and administrative support, without whom this work would not have been possible.

Lab member composition can make a world of a difference in the knowledge gleaned from an experience such as this. I would like to thank my fellow current and former STSL lab members, particularly Allison Mahvi, Daniel Kromer, Dhruv Hoysall, Alex Rattner, and Jennifer Lin for their individual contributions to this environment and opportunity. I have had the opportunity to work along-side some of the most capable and intelligent people one could ever meet, and I am endlessly appreciative for this.

Finally, I would like to thank Mom, Dad, Rian, and Kristen for all your love and support throughout this process. I could not have done it without you.

TABLE OF CONTENTS

LIST OF TABLES

LIST OF FIGURES

LIST OF SYMBOLS AND ABBREVIATIONS

Symbols

A	Area, m^2
D	Diameter, m
f	Darcy friction factor
g	Gravity, $m\ s^{-2}$
G	Mass flux, $kg\ m^{-2}\ s^{-1}$
h	Heat transfer coefficient, $W\ m^{-2}\ K^{-1}$
H	Height, m
k	Thermal conductivity, $W\ m^{-1}\ K^{-1}$
K	Loss coefficient
Nu	Nusselt number
num	Number
P	Pressure, kPa
Pitch	Pitch, m
Per	Perimeter, m
Pr	Prandtl number
R	Thermal resistance, $K\ W^{-1}$
Re	Reynolds number
t	Thickness, m
T	Temperature, °C
U	Velocity, $m\ s^{-1}$
UA	Overall thermal conductance, $W\ K^{-1}$
W	Width, m

Abbreviations

ACC	Air-cooled condenser
AD	Absolute deviation
AFR	Auto-fluttering reed
EES	Engineering Equation Solver
HRSG	Heat Recovery Steam Generator
ITD	Initial temperature difference, K
NTU	Number of transfer units
PCM	Phase change material
RAB	Reed attachment block
RTD	Resistance temperature detector
TC	Thermocouple

Greek Symbols

α	Aspect ratio
Δ	Differential

ε	Effectiveness
η	Efficiency
μ	Viscosity, kg m^{-1} s^{-1}
ρ	Density, kg m^{-3}

Subscripts

ACC	Air-cooled condenser
air	Air/Air-side
bare	Bare, without extended surfaces
cond	Conduction
cs	Cross section
cycle	Cycle
eff	Effective
ff	Free flow
fin	Fin
fr	Frontal
hy	Hydraulic
in/inlet	Inlet
min	Minimum
max	Maximum
os	Outside surface
out/outlet	Outlet
rib	Rib
sat	Saturation
steam	Steam
total	Total
tube	Tube
water	Water

SUMMARY

As global energy consumption grows, new generation power plants are continually being constructed to ensure that the electrical grid is capable of meeting increasingly high consumer demand for electricity. With thermal power plants accounting for nearly forty percent of the United States' freshwater withdrawals, the potential environmental impact of thermal pollution resulting from increased power plant heat rejection on freshwater resources has become an increasingly tangible concern. While alternatives to water-cooled condensation exist, historically they have underperformed and largely remain uneconomical in comparison. Air-cooled condensers (ACCs) rely on the forced convection of ambient air across inclined and finned tube bundles to condense the process steam, withdrawing and consuming no freshwater in the process, but resulting in higher required steam condensation temperatures and lower overall plant efficiency. To offset future global water constraints, it is important to further facilitate the installation of ACCs by improving their overall performance characteristics.

The focus of the present study is to evaluate the effectiveness of auto-fluttering reeds (AFRs) in enhancing the air-side heat transfer coefficient of an air-cooled power plant condenser, as well as the plant level efficiency improvements realized from reed installation. Flexible oscillating reeds, which are inserted directly into the air channels between the ACC fins, disrupt the air flow field by creating vortical structures that enhance the local heat transfer coefficient as well as the bulk fluid mixing process. A test section representative of a typical power plant ACC geometry was fabricated to analyze the heat transfer enhancement and pressure drop increase due to AFR installation over the baseline ACC geometry. A preliminary reed attachment device, which could be retrofitted and

installed directly onto existing ACC modules, was designed and manufactured using a combination of rapid prototyping techniques and electrical discharge machining (EDM) technology. The results for heat transfer and pressure drop from the test section were incorporated into a segmented condenser model on the *Engineering Equation Solver* platform to calculate the predicted ACC condensation temperature to transfer the steam condensation load. The standalone condenser performance predictions were then incorporated into a Rankine cycle model to determine plant-level enhancements realized with AFR installation.

The implementation of AFR assemblies into the ACC test section yielded heat transfer coefficient increases of approximately 25% at a pressure drop increase of 40%. Heat transfer gains were realized across a range of Reynolds numbers from 700 to 1700. While pressure drop penalties were significant, minor losses through the condenser cell were demonstrated to still be much larger than the pressure drop incurred across the ACC fins. Nusselt number and friction factor relationships were developed as a function of the channel Reynolds number. These relationships were implemented into the ACC computational model and Rankine cycle analysis program, demonstrating nominal plant efficiency gains of 0.4% due to AFR installation.

CHAPTER 1: INTRODUCTION

Climate change-induced drought, in addition to increased population density in urban areas, poses a critical threat to national security and international stability in the immediate future. Meanwhile, global energy demand continues to grow at an increasingly fast pace, prompting the construction and operation of hundreds of new thermal power plants that typically rely on large amounts of freshwater withdrawal and/or consumption to condense the steam used for energy generation. A transition to air-cooled power plant condensers (ACCs) is one method by which the historic and increasing reliance of the thermal power plant industry on freshwater usage can be significantly reduced.

ACCs utilize ambient air that is forced across finned steam condensation tubes by large diameter, low speed fans to condense the steam leaving the turbines to a liquid. The use of ambient air as the cooling medium for condensation presents several advantages and drawbacks in comparison with water. Where wet-cooled condensation results in massive water withdrawal rates, followed by large amounts of thermal pollution deposited back to the source in the form of elevated water temperatures, ACCs reject the waste heat to the atmosphere, which has a negligible impact on surrounding ecosystems. Siting requirements are also better in some aspects for ACCs in comparison with water-cooled condensers as they can be in regions lacking access to large and renewable freshwater resources without the concern for high rates of thermal pollution. Thermal power plants with ACCs also tend to have less rigorous and expensive maintenance and repair schedules due to the lack of water treatment chemicals necessary for water-cooled condensation (Mortensen, 2011). While these advantages have sparked a significant amount of interest in air-cooled condensation, there are several distinct disadvantages that must be addressed before further adoption of dry-cooled condensation technology.

1.1 Thermal Power Generation

The thermal power plants under consideration provide high-grade electrical energy to consumers by converting chemical potential energy, such as that stored in coal or natural gas, into the more readily usable form of electrical power. Governed by Carnot's theorem and the second law of thermodynamics, a certain amount of the chemical potential released by the fuel must be rejected to the environment as thermal energy, with the theoretical minimum rejected quantity of heat being proportional to the absolute temperature of heat addition and rejection (T_H and T_L, respectively) as demonstrated in Equation (1.1).

$$\dot{Q}_{L,\min} = \left(\frac{T_L}{T_H}\right)\dot{Q}_H \tag{1.1}$$

The most common system for thermal power generation is the Rankine cycle. The basic Rankine cycle consists of four primary components: a boiler, turbine-generator, condenser, and condensate pump. While industrial power plants consist of far more components, increasing the relative complexity of construction and design, these four primary cycle components provide a fundamental basis for thermodynamic analysis and assessment. The process fluid, typically water, is first sent through the boiler where the chemical potential energy in the fuel is converted into heat, boiling the working fluid into a high-pressure vapor. The high pressure and temperature superheated vapor is then routed through a turbine coupled with an electric generator, where the vapor expands in the turbine, allowing the generator to convert mechanical work into electrical power. At the exit of the turbine, a high quality two-phase fluid mixture is sent to the condenser, which returns the mixture to a sub-cooled liquid that is pumped back to the inlet of the boiler to repeat the cycle. Figure 1.1 illustrates the basic layout of a coal-fired Rankine cycle power plant.

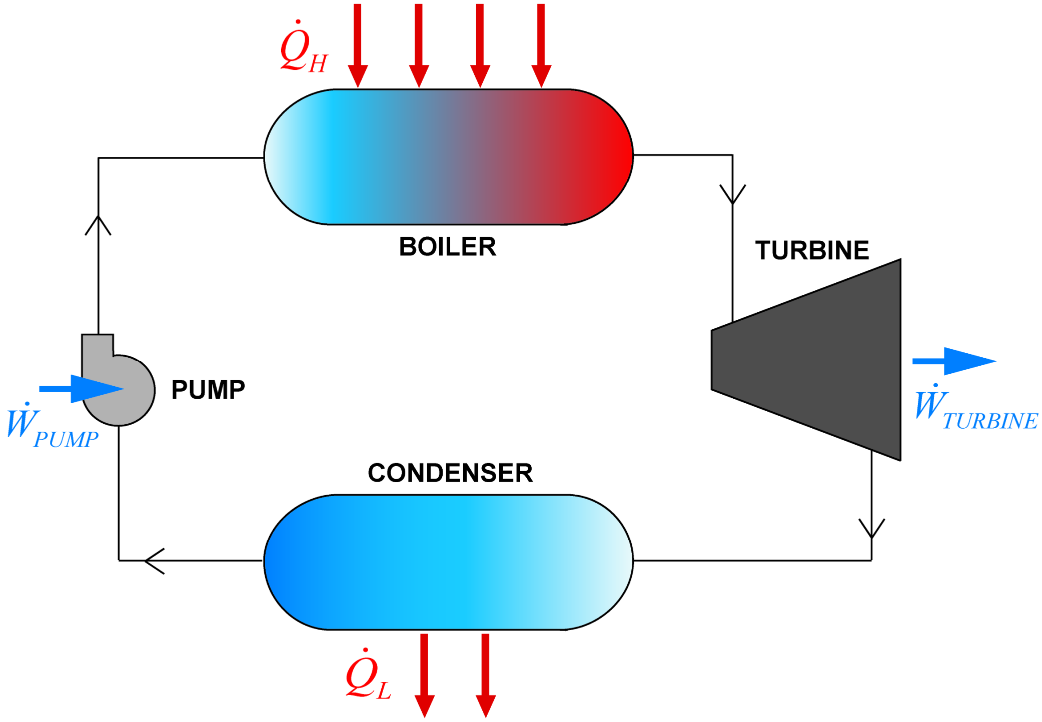

Figure 1.1 Basic Rankine cycle power plant schematic

The basic Rankine cycle can be modified to increase the overall plant efficiency while simultaneously decreasing the required heat rejection to the environment. One of the modified Rankine cycles is the reheat cycle, which employs the use of two turbines operating at a high pressure and lower pressure, respectively. In between the turbine stages the steam is reheated by being routed once-more through the boiler. The reheating process results in increased boiler saturation pressure while maintaining a high overall steam quality at the turbine exit. Entrained condensed liquid droplets in low quality steam can damage the expensive turbine internal components, forcing restrictions on allowable turbine exit quality. Specifically, turbine exit quality is typically required to be greater than

88%, below which a number of methods must be employed to remove liquid droplets from the steam (Dechamps, 1996). Multi-stage turbines, some with as many as three independent pressure levels with numerous intermediate reheat stages, require a higher initial investment but can significantly improve overall plant performance resulting from the higher average temperatures for heat addition to the cycle.

Another method by which the basic Rankine cycle can be improved is the use of a feedwater heating scheme, also known as a regenerative Rankine cycle. After the steam expands through the high-pressure turbine, a portion of the flow is routed to another heat exchanger where it transfers some of its thermal energy to the feedwater flow entering the boiler. Similar in principle to the reheat cycle, the average temperature of heat addition is increased relative to the baseline Rankine cycle. By decreasing the mean temperature difference across which the heat is added to the boiling water in the boiler, regeneration reduces the rate of entropy generation in the boiler and increases the overall cycle efficiency (Habib and Zubair, 1992). The concept of feedwater heating can be extended to include multiple feedwater heaters, and the regenerative Rankine cycle can also be combined with the reheat/superheated Rankine cycle to maximize the cycle efficiency.

There are several thermal power plant designs that operate on similar thermodynamics principles but which result in increased plant efficiency relative to the Rankine cycle, one of which is the combined cycle thermal power plant. Combined cycle plants utilize a Brayton topping cycle with a Rankine bottoming cycle to convert some of the waste heat from the topping cycle into usable electricity. The Brayton cycle in a combined power plant, shown in Figure 1.2, relies on four primary components: the compressor, combustor, turbine-generator, and heat recovery steam generator (HRSG). Air is compressed to a high pressure in the compressor, at which point fuel is added and ignited in the combustor. This high pressure and temperature mixture is routed through the turbine, generating electrical power as well as the required cycle compressor work. The combustion products exiting the turbine stage are cooled in the HRSG and then re-routed to the compressor. The rejected heat from the HRSG, $\dot{Q}_L$, is input to the Rankine bottoming cycle as the heat is transferred into the Rankine cycle boiler, and a portion of this rejected heat is then converted to electrical power as described in the above sections discussing the baseline and enhanced Rankine cycles.

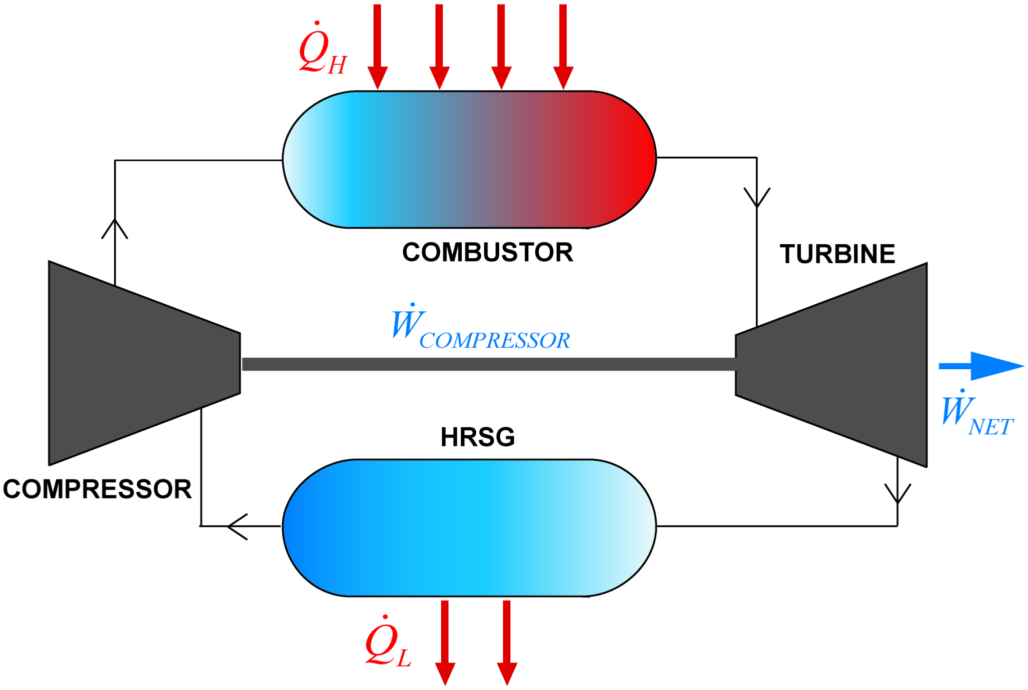

Figure 1.2 Brayton topping cycle for combined power plant schematic

While the capital costs for combined cycle plants tend to be higher than those for standard Rankine cycle power plants, there are several distinct advantages in comparison. The high temperatures in the gas turbine cycle offer high Carnot efficiencies, and the Rankine bottoming cycle allows the minimization of rejected waste heat, which can prove to be particularly valuable, especially in plants with air-cooled condensers where the average unit cost of heat rejection tends to be higher due to the elevated steam saturation temperatures. Combined cycle plants can achieve overall plant efficiencies ranging from 50 – 60%, meaning increased capital investments are realized in a shorter return period in comparison with basic Rankine cycle plants. Another advantage of gas-turbine installation is the rapid start-up time that can be achieved, making them an attractive option for load-following power supply schemes or as an emergency power supply source to the electrical grid under beyond-design-basis demand.

1.2 Water-Cooled Condensers

Water-cooled power plants condensers outperform air-cooled condensers in efficiency and reduced capital cost investment, but the environmental consequences related to thermal pollution as well as the limited siting availability in locations lacking access to freshwater resources have led recent investigators to once again consider air-cooled condensers as an increasingly promising alternative to water-cooled condensers. Figure 1.3 illustrates the general layout for the primary wet-cooled condensation technologies, once-through and recirculating/evaporative condensers.

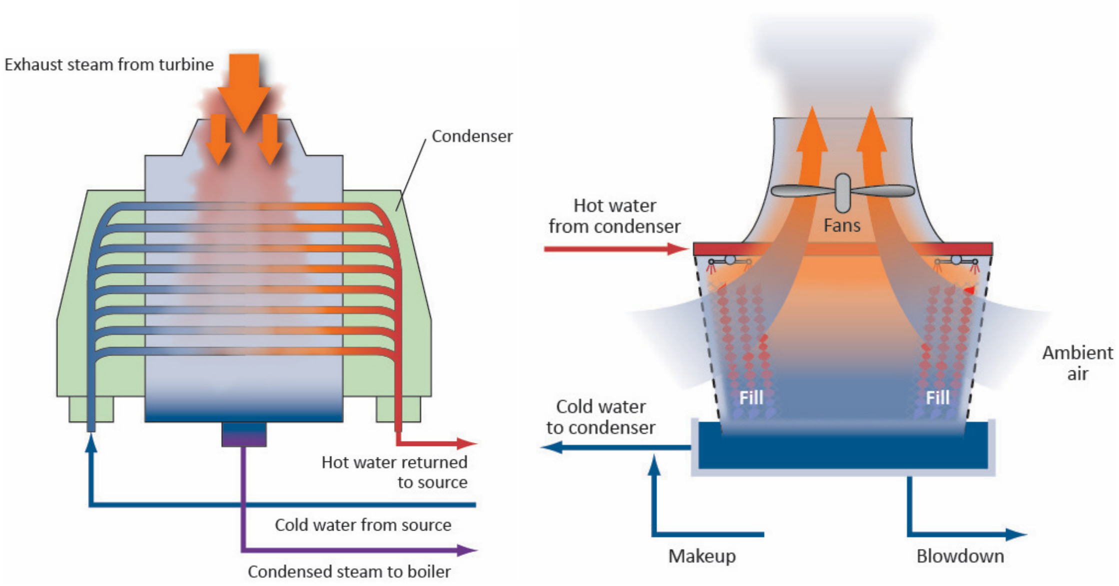

Figure 1.3 Schematics for wet-cooled power plant condenser technologies (once-through at left, recirculating at right) (Bushart, 2014)

Of the United States fleet of thermal power plants, over 99% utilize water-cooled condensers to maximize the decrease in steam condensation temperature afforded by the cooling at wet bulb, instead of dry bulb temperature, while requiring lower capital installation costs (Lin, 2016). There are two primary forms of water-cooled power plant condensers: once-through, and recirculating cooling tower designs. Once-through condensers withdraw water from a source, use it to remove heat from the condensing steam, and then pump it back to the water source without consuming or vaporizing the water. The water returning to the source is thus increased in bulk temperature, typically on the order of one to ten degrees Celsius (World Nuclear Association, 2016). In contrast, evaporative cooling towers rely on the evaporation of water from a liquid to a vapor state, taking advantage of the high latent heat of evaporation to reject the waste heat from the condensing steam to a heat sink at approximately the wet bulb temperature. While a portion of the water used in the evaporative-cooling towers is lost from the source as vapor through the stack, they typically withdraw up to 95% less water by volume than once-through steam generators. Thermal power plants account for upwards of 38% of freshwater withdrawals in the United States, withdrawing more than two-hundred billion gallons per day, which makes them the single largest source of water withdrawal (Maupin *et al.*, 2014). More than 90% of the freshwater withdrawal for power plants is directly used for steam condensation purposes.

In a typical Rankine cycle thermal power plant, around 60 – 65% of the chemical energy released from the combustion of fuel is rejected to the environment as thermal energy. To combat the negative environmental effects associated with high levels of rejected heat, regulatory limits are imposed on the maximum return temperature of the cooling water to its source, typically being limited to 30°C (World Nuclear Association, 2016). Particularly in the summer months coinciding with serious drought conditions, the restrictive temperature limits imposed on once-through condensers often require the total power output of a plant to be de-rated to avoid fines or other regulatory measures stemming from thermal pollution of the freshwater resources utilized for steam condensation. These months of potentially reduced plant capacity often coincide with the highest grid load due to increased consumer air-conditioning electricity needs. Consequently, even small amounts of power reduction at the plant level can be very troublesome to the consumer.

The other method by which excess heat from combustion can be rejected is by utilizing the large latent heat of vaporization of water during liquid-to-vapor phase change. The heat of vaporization of water, being orders of magnitude greater than the sensible heat required to raise the water temperature, is very effective at rejecting large amounts of heat. While the steam condensation temperature can be significantly reduced with evaporative condensers relative to entirely dry-cooled systems, a significant portion of the withdrawn freshwater is vaporized by the condenser, and can lead to aquifer and resource depletion. Figure 1.4 demonstrates the relative magnitudes for water withdrawal and consumption corresponding to various condensation technologies.

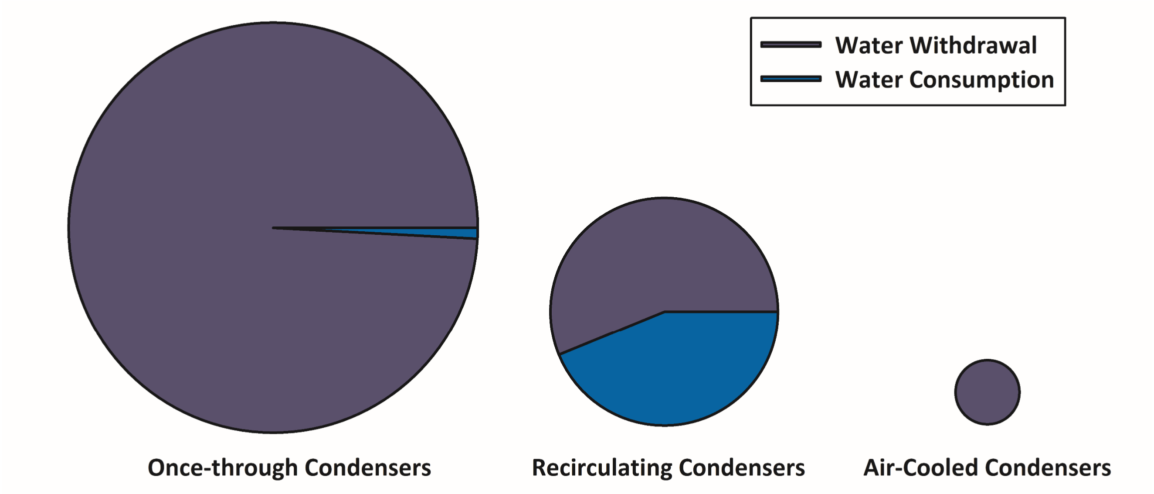

Figure 1.4 Relative water withdrawal and consumption rates for various condenser technologies (Force, 2003)

1.3 Air-Cooled Condensers

Air-cooled condensers are one of the technologies by which waste heat can be rejected from a thermal power plant without the need for withdrawal of water from rivers or lakes. In contrast to water-cooled power plant condensers, ACCs utilize ambient air as the cooling fluid for steam condensation, which results in significantly higher condensation temperatures, driving down the overall plant efficiency. Additionally, the low thermal capacity of air demands large heat transfer surface areas, resulting in an increased condenser footprint relative to water-cooled technology as well as significantly higher capital costs associated with construction and installation. It has been shown, however, that an eight-fold increase in water withdrawal cost from the average cost would result in equal return on investment periods for ACC plants in comparison with plants utilizing water-cooled solutions to condensation (Zhai and Rubin, 2010).

The typical A-frame ACC module ground footprint under consideration is approximately 144 m^2 with a module height of approximately eleven meters. At the top of each module, a large duct routes steam from the exit of the turbine-generators to the vertically inclined flat condenser tubes. The total inclined tube length is typically limited by the steam-side pressure drop, which results in a corresponding drop in saturation temperature and requires an increased initial temperature difference (ITD), defined as the difference between the inlet steam saturation temperature and inlet air temperature, for a given heat duty. Figure 1.5 illustrates the layout of a standard ACC module.

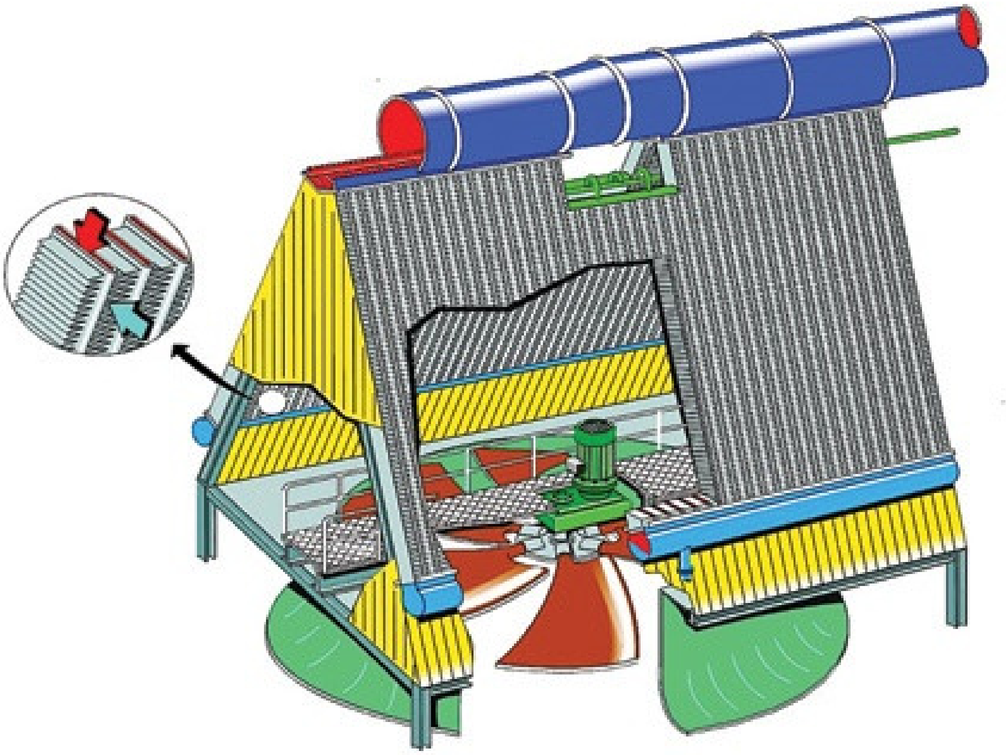

Figure 1.5 Representative ACC unit cell with auxiliary components (SPX, 2015)

A thermal power plant has numerous ACC modules in parallel and series based on the total heat load that must be rejected, as well as other critical design factors, including the anticipated environmental conditions in which the plant is situated. The array of condenser modules is elevated above ground level, as demonstrated by Figure 1.6, to allow for maximum air flow through the array while minimizing the pressure drop up to and through the condenser cell, which is proportional to the total fan power required for each unit cell. Minimizing the pressure drop penalty across the ACC finned tube bundle is one of the critical design factors in maximizing the overall power plant efficiency while mitigating the need for withdrawal of freshwater resources.

Figure 1.6 Elevated air-cooled condenser array (SPX, 2015)

The last decade has been witness to a renaissance of dry-cooled condenser technology with an increasingly fast adoption of ACCs for use in power generation industries. Assuming a conservatively linear increase in ACC installation based on extrapolation of the recent rate of new installations, the United States fleet of power plants will use ~ 5% dry-cooling condensation technologies between 2020 and 2095 (Davies *et* *al.*, 2013). Other regions, particularly those that lack access to large quantities of freshwater for withdrawal, anticipate far greater maximum dry-cooling shares as water scarcity becomes an increasingly tangible possibility. To illustrate this effect, Table 1.1 tabulates the USA and Middle East current and predicted future shares of dry-cooling technology in thermal power generation to illustrate the massive increase in anticipated dry-cooling growth rates. The development of more efficient dry-cooled condensation techniques will be critical to the continued adoption of water-free thermal power plant operation.

Table 1.1 Dry-cooling share of total thermoelectric generation (Davies *et al.*, 2013)

Region	*Dry-Cooling Share (2005) [%]*	*Projected Dry-Cooling Share (2020-2095) [%]*	*Percent Increase (%)*
USA	0.2	5.0	2500
Middle East	1.8	30.0	1566

1.4 Difficulties in Air-Cooled Condensation

While the stringent siting availability requirements and environmental concerns associated with water-cooled condensation are largely negated by the installation of ACCs, there are numerous drawbacks inhibiting their widespread implementation. The use of ambient air as the coupling fluid for steam condensation decreases the overall heat transfer rate per unit surface area, requiring an increase in steam condensation temperature to achieve the required amount of heat rejection from the condenser module. With increasing global demand for clean energy as well as continued desire to save costs in power plants, the overall plant efficiency is a critical factor in future power plant design. As such, the impact of a one to two percent decrease in plant efficiency from the use of air-cooled condensation technology is significant. Decreased power plant efficiency effectively results in higher pollution rates per unit of electrical energy produced and can negate the environmental benefits of ACC implementation.

Despite air-cooled condensers typically not relying on external water sources for power plant heat rejection, certain scenarios do in fact require the use of water in an air-cooled condenser cell. Particularly in summer months where the ambient temperature of the air is higher than the design condition for a given condenser, air-cooled condensers rely on water spray-nozzles to reduce the inlet air temperature. During the phase-change process, with the overall energy in the air-water mixture remaining constant, the evaporation of the sprayed water into the air/water mixture draws energy from the air, resulting in a decreased bulk air temperature limited to the wet-bulb temperature of the ambient air. Although the effect of cooling the inlet air does allow for operation even in relatively high ambient temperature conditions, large amounts of water are required to maintain adequate plant performance. Previous studies have shown this value to be as high as 3.4 – 5.7 $m^3 s^{-1}$ per ACC module in ambient temperatures as high as 40°C (Maulbetsch and DiFilippo, 2003).

The capital costs associated with ACC construction are higher than those for once-through or evaporative water cooled condensers. Where water-cooled condensers can achieve the required heat transfer with a relatively small heat transfer area and a low driving temperature difference, ACCs require relatively larger modules with significant heat transfer enhancements efforts to achieve similar performance levels even at higher initial temperature differences. Despite significant water savings, the overall capital cost increase of ACCs relative to water-cooled condensers can range from around \$8 – \$27 million, which often overshadows the incentives for installation of this technology (Maulbetsch and DiFilippo, 2006). The increased capital cost, in addition to the significant decreases in both plant efficiency and power output, leads to longer returns on investment for utilities analyzing the implementation of ACCs. The impact of increased capital expenditures was shown to result in an increased cost of electricity for the end-consumer from \$69.1 MWh^{-1} to \$73.1 MWh^{-1} for power plants with dry-cooled condensers in comparison with plants outfitted with water-cooled condensation technology (Zhai and Rubin, 2010).

There are several other environmental factors that can negatively impact the performance of ACCs, the most severe of which is related to high ambient air temperatures requiring evaporative cooling for the air or lowered plant capacity. The effect of external wind on ACC performance has also been the focus of several recent studies. Investigators have discovered that wind drafts surrounding an ACC module can result in large recirculation patterns as well as degraded fan performance due to distorted inlet velocity fields (Maulbetsch *et al.*, 2010). ACC modules are typically outfitted with several barriers and structures to prevent the negative effects of blowing or recirculation across the tube bundle. Other weather features including rain, hail, and snow, as well as biological hazards such as birds and insects, have also been shown to have large negative impacts on ACC and plant-level performance. Pollen, dust, and other fouling sources are known to create a measurable increase in overall thermal resistance and corresponding increase in required steam condensation temperature.

1.5 Scope of Present Work

The present work is focused on the investigation of air-side heat transfer enhancement of air-cooled condenser tube bundles using auto-fluttering reed technology.

A scaled test section representative of a power plant ACC dimensions was designed and manufactured, and tested in a temperature and humidity controlled wind tunnel test facility to evaluate the heat transfer and pressure drop characteristics of baseline and AFR-enhanced ACC geometries. These performance metrics were then used to evaluate the plant-level performance gains realized by AFR installation by means of a Rankine cycle analysis program developed on the Engineering Equation Solver (EES) platform.

1.6 Thesis Organization

This thesis is organized into the following chapters:

Chapter Two presents a comprehensive review of the literature related to air-cooled condensers, air-side heat transfer enhancement, and the impact of ACC performance on overall thermal cycle efficiency.

Chapter Three describes the wind tunnel test facility and the ACC test section developed at the Sustainable Thermal Systems Lab (STSL), and the experiments to investigate the impact of auto-fluttering reeds (AFRs) on ACC performance.

Chapter Four describes the data reduction methods used to analyze the measurements obtained in the wind tunnel test facility and fully instrumented ACC test section.

Chapter Five presents an analysis and discussion of the results gathered from the ACC wind tunnel test facility relating to individual condenser performance, as well as the impact on overall cycle efficiency.

Chapter Six presents conclusions from this research and also presents suggestions for further research related to AFRs and ACC performance enhancement.

CHAPTER 2: LITERATURE REVIEW

This chapter presents a comprehensive review of the literature on ACC implementation, steam-side heat transfer and pressure drop analysis, air-side heat transfer and heat transfer enhancements techniques, and ACC performance and its impact on overall plant performance.

2.1 Air-Cooled Condenser Heat Transfer and Pressure Drop

The heat transfer and pressure drop characteristics of both the air- and steam-side flows have been shown to be critical to the overall performance of the ACC module. Despite air-side resistances typically being considered as the limiting factor for condenser performance, it is important to accurately evaluate the steam-side performance, particularly when considering scenarios in which the air-side thermal-hydraulic performance is greatly improved over baseline conditions. Of the convective transport processes, the analysis of the steam-side phenomena is more complicated due to the two-phase condensation process. Nevertheless, accurate steam-side analysis is important to understanding the performance of an ACC.

2.1.1 Steam-Side Literature

Until recently, the steam-side heat transfer and pressure drop characteristics of an air-cooled condenser have not been considered to be the limiting factor relating to the overall ACC thermal-hydraulic performance, based on the assumption that high steam-side condensation heat transfer coefficients would result in the steam-side thermal resistance accounting for less than 5 – 6% of the total thermal resistance in an air-cooled condenser tube (Bustamante *et al.*, 2015). A significant amount of research has been focused on characterizing condensation in a variety of tube-side flow regimes, tube orientations, and working fluids. Many of the correlations and analytical models developed to address condensation phenomena are focused on small hydraulic diameter tubes with relatively high mass fluxes (Mahvi *et al.*, 2015). Steam condensation within an ACC module, however, occurs in somewhat larger hydraulic diameter, high aspect ratio flat tubes with significantly lower mass fluxes than those in the majority of the literature (Shah, 1979; Yang *et al.*, 1997; Chen *et al.*, 2002; Akhavan-Behabadi *et al.*, 2007). It is thus important to understand and accurately characterize both the steam-side and air-side heat transfer and pressure drop characteristics to confirm the assumption that the steam-side heat transfer characteristics do not limit the overall total condenser effectiveness, as well as to provide more accurate characterization of cycle efficiency gains resulting from the various enhancement techniques applicable to ACC geometry.

Shah (1979) proposed an empirical correlation for condensing internal flows in circular tubes with hydraulic diameters ranging from 7 – 40 mm. This correlation, developed by curve-fitting a large database of condensation literature, utilized data from horizontal, vertical, and partially inclined tubes. The reduced pressure and mass flux in a representative ACC tube are below the lower end of the correlation's applicability ($\boldsymbol{P}_{r,ACC} = 0.001$ vs. $0.002 < \boldsymbol{P}_{r,Shah} < 0.440$ and $\boldsymbol{G}_{ACC} = 5$ kg m^{-2} s^{-1} vs. 11 kg m^{-2} s^{-1} $< \boldsymbol{G}_{Shah} < 1600$ kg m^{-2} s^{-1}, respectively). The impact of flow regime on heat transfer coefficient can be significant, particularly in large hydraulic diameter tubes. For the low mass fluxes experienced in air-cooled condensation tubes, it may be appropriate to use falling film condensation correlations for ACC steam-side heat transfer coefficient calculation (Mahvi *et al.*, 2015). Chen *et al.* (1987) used analytical solutions combined with experimentally gathered data to develop an accurate and comprehensive correlation for condensate heat transfer in falling films. Vertically and horizontally oriented tubes were investigated in concurrent condensation arrangements.

A comprehensive literature review on condensation heat transfer and pressure drop characteristics in air-cooled condenser tubes was presented by Mahvi *et al.* (2015). A computational model in EES that implemented several steam-side heat transfer and pressure drop correlations to demonstrate the large variation in predicted plant-level performance was developed. Figure 2.1 illustrates the significant variations between predicted heat transfer coefficients along the length of the inclined air-cooled condensation tube from seven independent investigations.

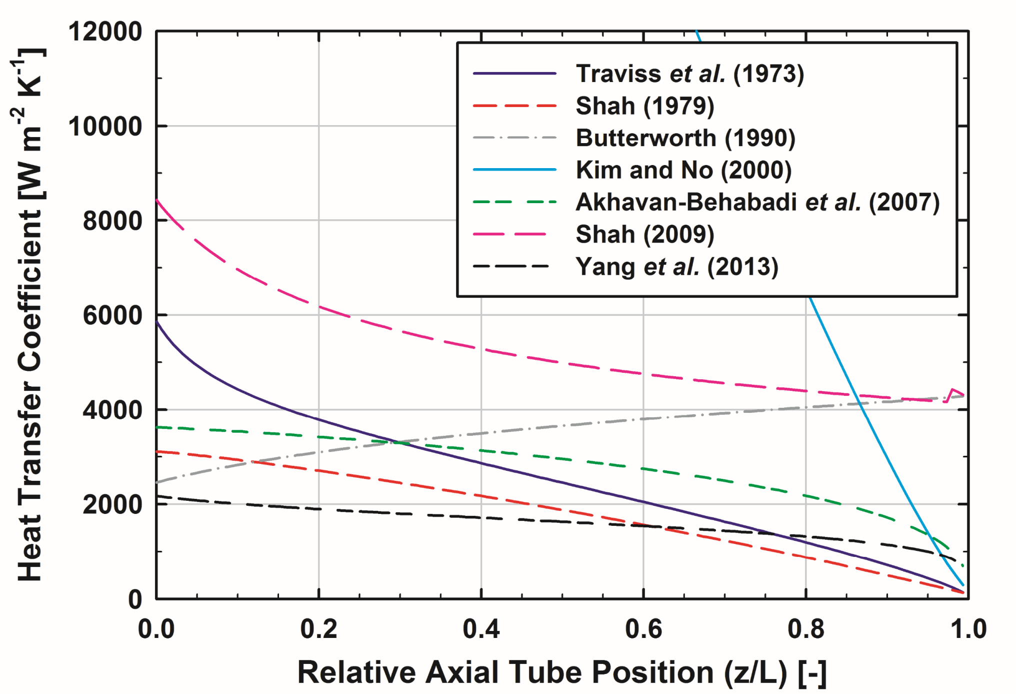

Figure 2.1 Steam-side heat transfer coefficient along condenser tube length (Mahvi *et al.*, 2015)

With variations of greater than 300% between the most and least conservative heat transfer coefficient estimates, Mahvi *et al.* (2015) determined that the corresponding overall Rankine cycle plant efficiencies ranged from 33 to 33.75%. More importantly, the thermal resistance fractions for both the steam-side and air-side varied significantly along the length of the steam condensation tubes based on the selected condensation heat transfer coefficient. By comparing the most and least conservative correlations (Yang et al. (2013) and Shah (2009), respectively) it is observed that the air-side heat transfer is not necessarily the only significant limiting thermal resistance factor when the average condensation heat transfer coefficient is less than 2500 W m^{-2} K^{-1}. As the steam condenses along the length of the inclined tubes, the vapor-phase mass flux and corresponding flow velocity decreases due to the large drop in specific volume, which leads to large decreases in the steam-side heat transfer coefficient inside the condenser tube. Figure 2.2 demonstrates the convergence of the steam-side and air-side thermal resistance fractions for the most and least conservative heat transfer coefficient estimates, particularly in the last 40% of the condenser tube, where the individual thermal resistances range from approximately 20 – 40% and 75 – 60%, respectively.

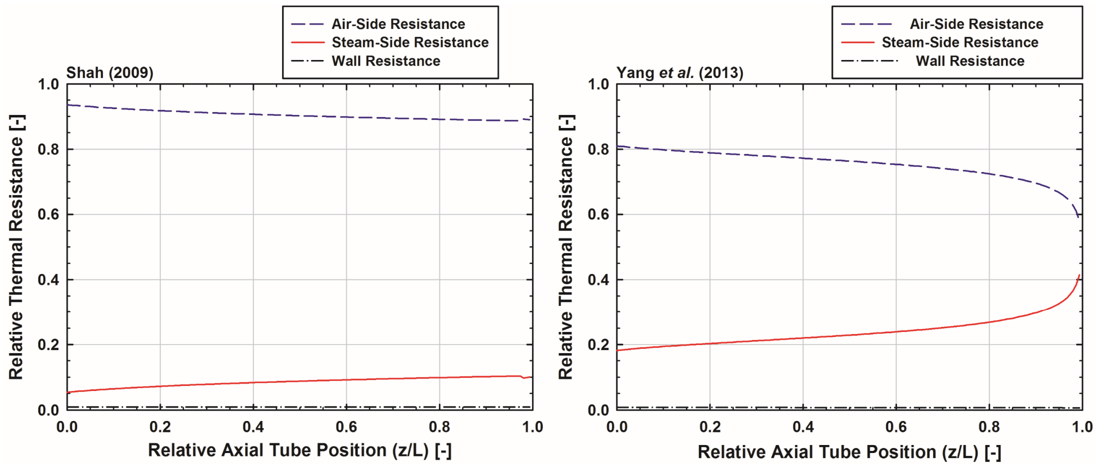

Figure 2.2 Thermal resistances along length of condensation tube (Mahvi *et al.*, 2015)

If air-side heat transfer performance continues to improve through various enhancement techniques, the steam-side heat transfer would have a more significant influence on the overall heat transfer coefficient. Consequently, local steam-side heat transfer resistance reductions may also help in improving the thermal-hydraulic performance of the ACC cell. As the steam-side resistance increases toward the low-quality regions of the condenser, improvements in this area would be particularly useful.

One of the primary mechanisms by which steam-side condensation heat transfer can be drastically inhibited is the ingress of non-condensable gases into the condensing flow. ACCs operate at sub-atmospheric pressures associated with steam saturation temperatures ranging from 30 – 60°C, and thus ambient air can enter the condenser. The presence of air inside the condenser tubes introduces an additional mass transfer resistance between the liquid and vapor phases of the condensing steam, inhibiting the condensation heat and mass transfer phenomena. Mahvi *et al.* (2015) quantified the negative impact of air ingression on the steam-side heat transfer performance of ACCs using the data and correlations from Caruso (2005). They noted that at steam qualities greater than 50%, ambient air ingress on a mass basis of just 1 – 2% resulted in significant decreases in steam-side heat transfer coefficient, which would lead to the steam-side heat transfer performance becoming a significant limiting factor in the total thermal resistance between the condensing steam and forced air flow. ACC modules are outfitted with mechanisms to purge non-condensable gases from the condenser tubes, but it should be noted that decreased condensation temperatures and pressures due to improved ACC performance would likely result in higher rates of air ingression and require a more effective means by which air could be purged from the condensing flow. The negative impact of non-condensable gases is less significant at the low qualities toward the outlet of the A-frame condenser (Mahvi *et al.*, 2015). While the majority of non-condensable gas investigations have been conducted on flat and vertical tubes, Caruso *et al.* (2013) studied the impact of these gases on inclined tubes, noting that the heat transfer coefficients at a given level of air ingression were the highest at angles of 15° and 30° above the horizontal, and lowest at inclination angles of 7° and 45°. An R^2 value of approximately 0.92 represented an average error of less than 20% between the correlation developed for heat transfer inhibition and the data at all inclination angles investigated.

Steam-side pressure drop also adversely affects overall condenser performance. Excessive pressure drop along the length of the condenser decreases the steam-side saturation temperature, which results in a lower driving temperature difference between the steam and the air, in turn lowering the effective heat transfer capacity from the condensing flow. The saturation temperature gradient with respect to pressure at 20 kPa $\left[\left(dT_{\text{sat}}/dP\right)_{20\text{ kPa}}\right]$ is approximately 1.1 K kPa^{-1}, demonstrating the significance of small changes in steam pressure on condenser performance at the steam saturation pressure encountered in an ACC module (Mahvi *et al.*, 2015). Furthermore, this value is increased to nearly 4.25 K kPa^{-1} as the steam pressure is reduced to four kilopascals, a result of lowered saturation temperatures due to increased condenser performance. Two-phase pressure drop is one of the driving design aspects for the steam-side geometry and condenser performance, particularly at the sub-atmospheric pressures experienced in the ACC condenser tube.

The two-phase pressure drop along an ACC tube can be described as shown in Equation (2.1), with the terms corresponding to the frictional, gravitational, and fluid deceleration pressure losses, respectively.

$$-\left(\frac{dP}{dz}\right)_{total} = \underbrace{-\left(\frac{dP}{dz}\right)}_{Frictional} + \underbrace{\left[(1-\alpha)\rho_{l} + \alpha\rho_{v}\right] g\sin\beta}_{Gravitational} + \underbrace{\frac{d}{dz}\left[\frac{G^2x^2}{\rho_{v}\alpha} + \frac{G^2(1-x)^2}{\rho_{l}(1-\alpha)}\right]}_{Deceleration} \quad (2.1)$$

The gravitational and deceleration pressure drop terms increase the saturation pressure (and temperature, accordingly) along the length of the vertically inclined condensation tube, while the frictional pressure drop decreases the total steam pressure. Unlike the gravitational and deceleration pressure drop terms, the frictional pressure drop is calculated empirically based on experiments performed under operating conditions similar to those of interest in ACCs; however, the number of investigations on low mass flux condensation in large hydraulic diameter tubes is fairly limited. Chisholm (1967) presented a two-phase multiplier, which when multiplied with the single-phase vapor friction factor, yields the two-phase frictional pressure drop. The two-phase liquid and vapor multipliers are calculated using Equations (2.2) – (2.3), where the constant C accounts for the variation between liquid and vapor flow regimes.

$$\phi_L^2 = 1 + \frac{\boldsymbol{C}}{\boldsymbol{x}} + \frac{1}{\boldsymbol{x}^2} \quad (2.2)$$

$$\phi_G^2 = 1 + \boldsymbol{Cx} + \boldsymbol{Cx}^2 \quad (2.3)$$

Friedel (1979) proposed a set of correlations for vertical downward flows that may be applicable to ACC tubes, noting that wave structures in the downward condensate flow affected the liquid-vapor interface dynamics and must be accounted for in the frictional pressure drop analysis. Over 25,000 data points were used to generate the correlations, with approximately 5% of these data points corresponding to downward condensing flows for two-phase mixtures. Improving upon previous attempts at characterizing the two-phase frictional pressure drop, Chen *et al.* (2002) introduced several new dimensionless parameters into the formulation, including the Bond and Weber numbers, as shown in Equations (2.4) and (2.5), respectively.

$$Bo = \frac{\Delta \rho g L^2}{\sigma} \tag{2.4}$$

$$We = \frac{\rho v^2 l}{\sigma} \tag{2.5}$$

The resulting correlation for two-phase flows in small hydraulic diameter tubes predicted the data with an average deviation of approximately 19%. Despite the relatively significant two-phase frictional pressure drop correlation variance in the literature, the predicted plant-level efficiency only changes from 33.02 to 33.09% from the most to least conservative correlations at elevated ambient temperatures (Mahvi *et al.*, 2015). At lower ambient temperatures, however, the variance in power plant efficiency related to the variance in two-phase pressure drop correlations is far greater. Figure 2.3 illustrates the variance in predicted plant efficiency amongst four independent empirical correlations for frictional pressure drop under varying ambient temperature conditions ranging from -10 to 30°C.

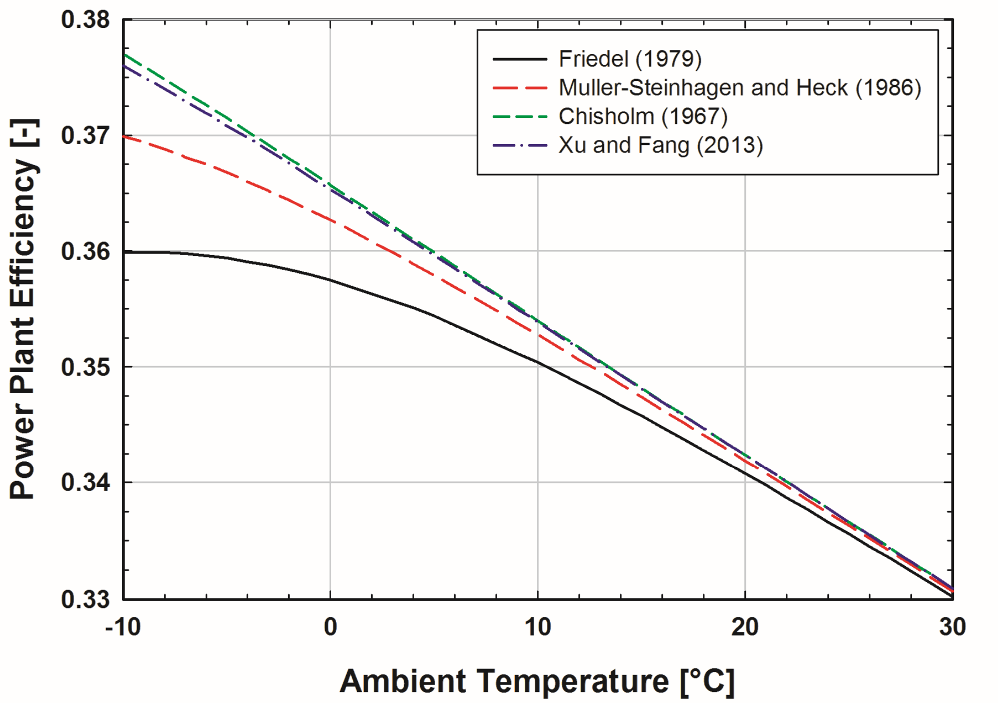

Figure 2.3 Steam-side pressure drop correlation impact on efficiency (Mahvi *et al.*, 2015)

Steam-side condensation heat transfer and pressure drop at low mass fluxes is relatively poorly understood. The variance amongst correlations makes it difficult to accurately predict thermal hydraulic performance within any measure of certainty. While several of the condensation heat transfer coefficient correlations evaluated by Mahvi *et al.* (2015) demonstrate the significance of steam-side heat transfer thermal resistance to the total thermal resistance, the majority of the predictions as well as those of other literature sources argue that significant improvements in ACC performance can only be realized by focusing on air-side heat transfer effectiveness until it has reached a point where its relative thermal resistance is comparable to that of the tube-side thermal resistance.

2.1.2 Air-Side Literature

The body of literature on maximizing ACC performance is significant, with most studies focusing specifically on air-side improvements. Air-side characteristics are typically viewed as the limiting performance factors in the present generation of air-cooled condensers. Many of these studies attempt to decrease the air-side thermal resistance using external heat transfer enhancements to the ACC condenser tubes.

To maximize the effective air-side heat transfer surface area of an ACC module, condensation tubes are outfitted with external fins. Lin (2016) demonstrated the effectiveness of parametric optimization with fin geometry, proving that simple geometry variation would result in overall plant efficiency gains of approximately one percent, based on the geometric variations shown in Table 2.1.

Table 2.1 Baseline and Enhanced Plain Fin Geometric Parameters (Lin, 2016)

Geometry	*Fin Height (mm)*	*Fin Spacing (mm)*	*Fin Thickness (mm)*	*Rankine Cycle Efficiency (%)*
Baseline	25.4	2.54	0.254	32.9
Enhanced	25.4	1.143	0.254	34.0

By decreasing the fin spacing along the length of the ACC tube from 2.54 mm to 1.143 mm, the overall cycle efficiency was demonstrated to increase by 1.1%. The plant efficiency increase due to optimized spacing corresponded to an ITD decrease of 13 K and increased electrical power input to the fan from 10.17 MW to 16.5 MW. The increased fan power consumption is primarily a result of increased mean air flow velocity; a lower fin pitch results in a decrease in free flow area, and for a given volumetric flow rate an increase in average air channel velocity. The hydraulic diameter of the air-side fin channels also decreases, increasing the air-side pressure drop along their length. While variation of other parameters, including fin height and thickness, yielded generally lower steam ITDs for the ACC module, the performance enhancements realized in the turbine-generator were counteracted to some extent by the increased fan power required to provide sufficient air flow across the module, and as such the variation of these parameters was not determined to be as beneficial as the variation of the fin pitch. The combined cycle plant analysis yielded results for efficiency optimization similar to those for the Rankine cycle investigations, with an increase in overall plant efficiency from 52.68 to 53.52%. Combined cycle plants reject less heat in the bottoming cycle relative to Rankine cycle plants because the high-grade waste heat from the Brayton topping cycle is recovered and utilized for increased net power output. With less heat rejected to the ambient, the benefits of improving condenser performance are less significant than those for Rankine cycle power plants.

Investigations on the enhancement of air-side heat transfer coefficient can be grouped into two categories based on the method of enhancement actuation, specifically passive and active enhancement. Passive heat transfer enhancements do not use external actuation and rely on geometry and intrinsic aspects of the air flow to cause increased heat transfer rates, while active enhancements utilize an external power source to produce the desired increase in heat transfer effectiveness. While the increase in heat transfer performance varies significantly amongst different enhancement methods, in all methods, increases in heat transfer coefficient are associated with increased air-side pressure drop and input power.

Two of the most common passive enhancement techniques for designing finned heat exchangers are the utilization of wavy or louvered fin surfaces. These surfaces act to disrupt the thermal boundary layer and increase mixing within the bulk fluid stream. This technology is easy to implement, but typically results in lower enhancement factors in heat transfer coefficient and in some cases, decreased condenser performance (Lin, 2016). Additionally, the use of different fin geometries is not suitable for retrofit applications.

Jacobi and Shah (1995) presented the results for different means of both active and passive heat transfer enhancement from longitudinal vortex generating structures mounted on a heat transfer surface. In studies evaluating single tubes in cross-flow arrangements and hydraulic conditions similar to those experienced in ACC modules, calculations indicated than an equivalent heat transfer rate could be achieved at Re = 1200 with passive vortex generators as tubes without passive enhancement at Re = 2000. Similarly, at Re = 5000, the overall heat transfer could be increased by approximately 20% while decreasing the commensurate pressure drop increase across the tube by 10%. The resulting decrease in fan power consumption for an ACC module could be significant, but implementation of such an enhancement method would prove difficult: an average ACC module consists of approximately 2.44×10^6 independent air channels, each of which would need to be outfitted with vortex generators prior to module construction if this method were selected for implementation in air-cooled condensers. While passive vortex generators are a proven method by which heat transfer can be improved, the complexity of implementing such a method on the scale of power plant ACCs would likely lead to it being better suited for small-scale applications.

Focusing on the design of condenser tubes, Sohal and O'Brien (2001) investigated the realizable performance gains in air-coupled heat transfer through the use of winglets and circular- and oval-shaped tube cross-sections. Varying combinations of winglet design, location, and tube shape were parametrically evaluated in a laboratory-scale test facility to obtain the Nusselt number and friction factor with and without local enhancements. The introduction of winglets at an angle of 45° relative to the air flow direction increased the air heat transfer coefficient by approximately 35% while increasing the effective friction factor by 5 – 10% for Reynolds numbers ranging from 500 – 5000. It was noted by them that the measured heat transfer coefficients were lowest in experiments without winglet pairs, for both circular and oval-shaped tubes.

Torii *et al.* (2002) evaluated the enhancement due to vortex generators on finned tube banks consisting of sixteen parallel plates and three rows of circular tubes, arranged either inline or staggered with a square pitch. At Reynolds numbers ranging from 300 to 2500, the heat transfer enhancement factor in the test section was calculated to range from 10 – 25% with a corresponding increase in pressure drop from 20 – 35%. The heat transfer enhancement factor demonstrated significant reduction at lower Reynolds number flows, suggesting that novel enhancements may be necessary for improving the heat transfer characteristics in ACC modules or other heat exchangers with Reynolds numbers lower than 1000. The flow acceleration associated with the vortex generating winglets was demonstrated to have the effect of delaying streamline separation from the circular tubes and subsequently improved heat transfer in the flow wake on the tube’s trailing edge. The staggered tube test section demonstrated better performance with vortex generating winglets at low Reynolds number flows, including a 55% pressure-loss reduction and 30%

heat transfer enhancement at Re = 350. The study focused on circular tubes with a fin pitch of 5.6 mm and tube pitch of 75 mm. As such, the applicability of vortex generators in long, straight fin channels with a fin pitch of 2.54 mm may not be accurately predictable by the results of their investigations.

Active enhancement methods offer one particular advantage over passive enhancement techniques: the actuation and control of the enhancement can be varied based on the required plant load requirements and ambient conditions in real-time (Jacobi and Shah, 1995). One method by which active enhancement can be achieved is the use of jet injection into the thermal boundary layer developing on the heat transfer surface. Previous studies demonstrated that a synthetic jet injected at 45° from the surface in the direction of the air flow produces two distinct vortical flow structures that lead to improved bulk fluid mixing and heat transfer in the boundary layer. The physical shape of the jet was determined to have little effect on the quantitative enhancement in heat transfer. Actual installation of jet producing devices on a large-scale heat exchanger has yet to be evaluated from effectiveness and cost standpoints.

The use of electrostatic fields was also posited as a means for active heat transfer enhancement, with Allen and Karayiannis (1995) providing the governing theories and equations required for a thorough understanding of electrohydrodynamics enhancement. The three primary techniques by which heat transfer rates can be improved with EHD enhancement include the following: corona wind flows, electrophoresis, and dielectric phoretic forces. Other AC field patterns (such as the square-wave) can have a similar hydrodynamic enhancement effect, although there are no experimental investigations of such a mechanism. Jacobi and Shah (1995) also proposed the use of electrohydrodynamics

(EHD) to produce a uniform body force on the air flow, which could increase the heat transfer performance at a given air-side volumetric flow rate. In EHD enhancement schemes, a body force imparted on the air flow from an external electric field produces a secondary flow structure within the heat exchanger. The stream-wise vorticity induced by the secondary flow field could significantly increase the heat transfer by sending longitudinal vortical structures along the length of an air-channel in an ACC module. Despite these postulated advantages, the literature on actively enhanced air-side heat transfer is limited, with almost no experimental investigations on the implementation of these techniques and the enhancements that can be expected. Furthermore, the economics of these methods, including the capital investment and operating costs, has not been assessed, and must be evaluated before widespread implementation can be considered.

Another method for active enhancement of heat transfer stems from the use of piezoelectric materials for surface excitation and boundary layer disruption. These externally powered mechanisms rely on the mechanical deformation of a material as a result of an applied voltage, and have the potential for significant heat transfer enhancement. Steinke and Kandlikar (2004) noted that the piezoelectric material could either be imbedded in the wall of the flow channel, or even surface coated, to achieve the desired boundary layer disturbance. The power requirements and capital costs associated with active enhancements such as piezoelectric material vibrations and EHD must be considered to assess the overall benefit of implementing this technique.

Introduction of materials into the forced air flow can also have a significant impact on overall heat transfer effectiveness by increasing the effective air heat capacity rate for a given volumetric air flow. Small phase-change materials (PCMs) are injected into the air flow in solid phase. Upon absorbing heat from the air equal to the latent heat of fusion of the solid, they melt. The effective heat capacity rate of air at a given mass flow rate is therefore significantly increased, increasing the heat capacity rate ratio $\boldsymbol{C_r}$ and improving the heat transfer effectiveness of a given heat exchanger geometry (Steinke and Kandlikar, 2004). This method allows for simple retrofitting of existing condenser infrastructure. The use of volatile liquids injected into the fluid stream can also have a significant impact on heat transfer effectiveness and could be used in situations where high grid demand is compounded by elevated ambient temperatures in summer months. While introduction of other materials in the air flow can result in higher rates of heat transfer from the ACC module, they may have detrimental effects on the condenser if any of the PCMs are deposited onto the fan or condenser surfaces as they pass through the module, leading to an increase in fan power input and total thermal resistance between the condensing steam and air.

Active and passive enhancements both have the potential to decrease the required condensation temperature for ACCs, but until now, they have not been implemented on a scale that would be significant to electrical power generation utilities. It has been demonstrated that passive enhancements typically suffer from lower effectiveness gains than active enhancements, but it is possible that active enhancements and their increased complexity for installation and operation would not be preferred for use in an ACC for thermoelectric power generation.

Heat transfer enhancement through the use of fluttering flag-like structures has been studied both from fluid and solid mechanics perspectives. Flutter is loosely defined in the literature as the result of the positive response of a body’s deformation to the body forces imparted by the fluid flow. Displacement or deformation in one direction results in net body forces imparted by the fluid flow on the flag in the opposite direction, resulting in the unstable oscillating motion associated with flag flutter mechanics. Steinke and Kandlikar (2004) presented the results of a study in which flow velocities were varied from 4.4 to 5.5 m s^{-1}, comparing the heat transfer from a heat sink with and without a passively driven, vibrating microfin array. They demonstrated heat transfer enhancements of approximately 11.5% over a plain heat sink. In addition, they noted that the microfins were vibrating at their natural frequency of oscillation of 1.17 kHz until a flow velocity of 6 m s^{-1} (Go, 2003). The pressure drop characteristics of these microfin arrays were not included in their discussion of the investigation, but they demonstrated heat transfer performance gains with flow-induced vibrations in a thermal heat sink.

Along with mechanical properties of the material selected for implementation, the design and geometry of the flag has a significant impact on the flutter frequency and fluid performance. Argentina and Mahadevan (2005) studied the solid and fluid mechanics principles associated with flag flutter in a confined fluid stream, determining that the critical velocity beyond which the reed will begin to flutter, and the corresponding flutter frequency proportionalities can be described as shown in Equation (2.6) and Equation (2.7), respectively.

$$U_c \sim \sqrt{\frac{Eh^3}{\rho_{air} L^3}} \tag{2.6}$$

$$\omega \sim \sqrt{\frac{\rho_f U^2}{\rho_s h L}} \tag{2.7}$$

The use of autonomously fluttering reeds (AFRs) for heat transfer enhancement has been demonstrated to provide significant improvements relating to heat transfer enhancement and commensurate pressure drop penalty reduction (Herrault *et al.*, 2012). AFRs, when placed within a fluid flow stream, oscillate unstably, generating vortical structures on their tip, which are sent longitudinally down the length of the confined air stream. The maximum deflection of the fluttering reed, as well as the vortical structure diameter, is bound by the walls of the air channel in which the reeds are placed. The vortices released from the AFR improve heat transfer by improving mixing in the bulk fluid stream as well as by disrupting the boundary layer at the channel walls. Figure 2.4 illustrates a qualitative example of the oscillation of an AFR within an air channel.

Figure 2.4 Representative AFR motion (in blue) within air channel (Mahvi *et al.*, 2015)

Hidalgo *et al.* (2010) demonstrated the effectiveness of piezoelectric reed elements within a small-scale finned heat sink. Active reed technology was selected for investigation because of its relatively low power consumption, low noise emission levels, and high power density capabilities with better than 100% heat transfer coefficient enhancement over equivalent finned heat sinks without active reed inserts. For a given power dissipated in the heat sink, the heat transfer coefficient with active reed actuation was comparable to the heat transfer coefficient without reed actuation at twice the flow rate. Thermal performance was also compared at equal fluid power of the air flow, with the active reed demonstrating a 42% increase in heat transfer coefficient at half the flow rate of the baseline heat sink, which corresponded to a decrease in the total thermal resistance of up to 21%. In other words, the required fluid power was nearly three times greater for the baseline heat sink than for the active reed enhanced heat sink to reject the same amount of heat from the air channels. They also used the concept of a coefficient of performance (COP) for the reed technology, defined as the ratio of dissipated heat to the total fluid power invested in the heat sink, to describe specific reed performance. With piezoelectric reed actuation, the COP of the heat sink increased by a factor of 1.4, demonstrating an overall increase in efficiency associated with this technology including the electrical losses due to the piezoelectric power system.

Following the demonstration of the actively powered reed technology, Herrault *et al.* (2012) expanded the scope of application and demonstrated the effectiveness of passively powered AFRs. Instead of utilizing the piezoelectric actuation as described previously, these AFRs utilized power from the air flow to oscillate unstably within the channel, producing similar longitudinal vortex structures as the actively powered reed technology. Flow-powered actuation results in less installation complexity and capital cost, albeit at the cost of lower heat transfer gains. Without the brittle piezoelectric material required to actuate the reeds, material fatigue and reliability issues were also largely mitigated with the use of flow-powered reeds. While the heat transfer enhancement ratio varied along the length of the test section due to the fluid dynamics of the traveling vortices downstream, local heat transfer coefficient enhancements of up to 2.5 times were calculated at the exit of the air channel with a self-oscillating reed.

In an attempt to maximize the performance of the self-oscillating AFRs, Hidalgo *et al.* (2015) studied the elastic oscillations associated with the reeds using a CCD camera to digitize the flag-like motion of an oscillating reed. For reed thicknesses and lengths ranging from 19 – 38 μm and 30 – 35 mm, respectively, the reed oscillation frequency increased from a minimum of about 105 Hz at Re = 2000 to a maximum of about 142 Hz at Re = 6000. Reed-to-surface interactions were shown to lower the performance of the reed oscillations, as the force imparted by the reed on the wall represents a loss in kinetic energy of the reed and requires more fluid power input to achieve the same frequency and energy of oscillation. Particle image velocimetry (PIV) was then used to measure the flow profile through the centerline of the air channel at ten locations along its length. The turbulent kinetic energy (TKE) was plotted and compared with and without reeds, as shown in Figure 2.5, to demonstrate the effectiveness of the reeds at improving local mixing and boundary layer disruption at the walls of the air channels. Particularly at the lower Reynolds number flow rates, the presence of the reed significantly increased the relative turbulent kinetic energy near the air channel wall (shown in light green at top right of Figure 2.5), indicating the effectiveness of the shedding vortices at penetrating the boundary layer in the air channel and improving the bulk mixing characteristics of the flow.

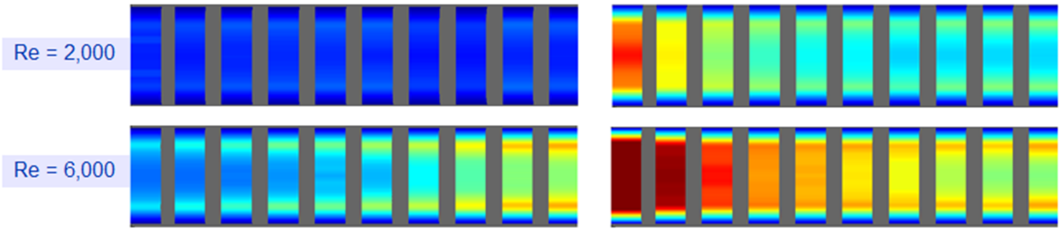

Figure 2.5 Turbulent kinetic energy comparison from PIV analysis comparing channels with (right column) and without AFRs (Hidalgo *et al.*, 2015)

Reynolds numbers ranging from 2,000 to 10,000 were evaluated for the total heat transfer enhancement from reed installation. Wall temperatures along the length of the test section channels downstream from the reed location decreased monotonically with increased Reynolds number, clearly demonstrating the decreased air-side convective thermal resistance. The predicted heat transfer coefficient increased across a range of

Reynolds numbers ranging from 2000 – 6000. Table 2.2 illustrates the percent increase calculated across the range of Reynolds numbers.

Table 2.2 Nusselt Number Enhancement (Hidalgo *et al.*, 2015)

Reynolds Number	*Percent Increase of Nu (%)*
2000	178
4000	182
6000	181

At the lower range of Reynolds numbers evaluated by Hidalgo *et al.* (2015), the COP for heat transfer in reed-enhanced channels was increased by a factor of 2.4, demonstrating equivalent heat transfer rates with a reduction in channel flow velocity of approximately 50%. While the low Reynolds numbers investigated in this study are closest in terms of representing the aerodynamics within air channels of ACC modules, higher enhancement in COP (up to a nine-fold increase) was demonstrated as the Reynolds number approached 6000.

While the ACC module fin and tube geometry can be optimized and enhanced to reject as much heat as possible for a given driving temperature difference, the overall ACC site construction and design also plays a significant part in minimizing the negative effects of the ambient environmental weather conditions such as wind, rain, and snow and can even outweigh the performance gains realized by other techniques if not carefully accounted for. The impact of these weather conditions on air-cooled condenser heat duty and fan power consumption was investigated by Mortensen (2011), who performed computational fluid dynamics (CFD) simulations to analyze the effect of ambient wind conditions on ACC cell thermal hydraulic performance. Wind conditions external to the

ACC module can result in recirculation of air around the cell, resulting in an overall degradation in fan performance. The primary mechanism for the loss in performance due to ambient wind was determined to be increased pressure drop caused by the cross-flow orientation of air entering the ACC cell. In some cases, the measured volumetric flow rate through the condenser cell at a given electrical power input was decreased by 50 – 60%, resulting in higher electrical draw from the fans and a decrease in plant efficiency to ensure the plant could meet the consumer energy demand.

Ambient wind conditions and plant operating characteristics were measured at a representative ACC module on-site at a Black Hills Power thermal power generating station and it was determined that poor wind dynamics resulted in an increased turbine back pressures of up to 3.8 cm H_2O with total turbine back pressure often reaching the operational limit of 21.59 cm H_2O (Mortensen, 2011). Increased turbine back pressure requires plant operators to de-rate or throttle back the fuel input to the boiler, lowering the net plant power output. To mitigate these impacts, wind vanes were installed on-site to limit the effect of recirculation and cross-flow of ambient air on ACC performance. The wind vane assemblies were shown to improve the effective air-side heat transfer coefficient by up to 5%. Black Hills Power determined that overall plant efficiency was less critical of a factor to the power plant operators than the total, time-averaged power output as the fuel costs are passed on directly to the customers of the utility in increased electricity costs.

2.1.3 Plant Level Performance Implications

Several studies have investigated the plant-level economic implications of ACC installation with the most significant being a report prepared for the California Energy Commission (Davis, 2002). One of the most widely recognized drawbacks to ACC installation is the decreased condenser performance at high ambient temperatures that results in elevated steam condensation temperatures above those practical for plant performance (Bustamante *et al.*, 2015). To mitigate these performance shortcomings, several systems that use the latent heat of fusion of water to lower the air temperature to the wet bulb temperature before it is sent across the condenser tube bundle have been investigated. While these hybrid wet/dry systems do offer increased performance in elevated ambient temperature conditions, they can require significant quantities of freshwater withdrawal and consumption. As such, the development of purely dry-cooled condenser technology is a critical next stop towards energy security in water-stressed regions and to improving the efficacy of ACC installation for future power plants.

Blanco-Marigorta *et al.* (2011) presented an exergetic analysis of a solar-thermal power plant, comparing the second law efficiency of power plants with and without dry-cooled condenser technology. The GateCycle software package was used to evaluate the exergy destruction rates in a Rankine cycle with feedwater and regenerative heating. Given the input efficiency parameters of components other than the air-cooled condenser, it was determined that the turbine efficiency decreases from 34.2 to 32% when air-cooled condensers are implemented in place of evaporative condensers. Exergetic analysis demonstrated that air-cooled condenser performance matches that of wet-cooled condensers at elevated turbine outlet pressures; however, higher turbine backpressure results in a correspondingly lower overall plant efficiency and is therefore not desirable. Comparing wet-cooled and dry-cooled technology at a turbine outlet pressure of 0.063 bar, a cooling tower represented only 6.8% of total fuel exergy destruction, whereas an air-cooled condenser would represent 25.5% of total exergy destruction in the same cycle resulting from the demonstrable increase in the parasitic losses in the large diameter, low static head fans in the condenser module. The minimum rate of exergy destruction is related to the ITD which is considerably larger in dry-cooled systems resulting from the mismatched heat capacity rates between the air and steam flows. Exergy destruction rates in components other than the turbine and condenser were not strongly dependent on the condenser technology selected, and therefore, turbine and condenser performance is of primary interest when determining overall cycle performance metrics in dry-cooling schemes.

Bustamante *et al.* (2015) presented several probable causes and potential solutions for the low plant efficiency associated with air-cooled condensers. Citing the low specific heat of air (~1.1 kJ kg^{-1} K^{-1}) compared to the high specific heat and heat of vaporization of water (~4200 kJ kg^{-1} K^{-1} and ~2.252×10^6 kJ kg^{-1} K^{-1}, respectively), they presented means by which equivalent plant performance can be obtained with dry-cooling technology. The large difference in specific heats results in high volumetric air flow to condense a relatively low mass flow rate of steam, resulting in increased parasitic fan losses in comparison with the electrical losses in the pumps used with water-cooled condensers. The initial temperature difference must also be increased to ensure adequate heat rejection from the condensing steam, which they noted led to increased turbine backpressure and decreased thermal efficiency. Noting that an increase in ambient temperature of just 10°C resulted in an estimated 4.2% decrease in net power output, it was determined that the use of combined wet/dry cooling technology could mitigate the impact of increased ambient temperature conditions. A 68% increase in air flow rate, 66% decrease in convective heat transfer resistance, and a 24% increase in pressure losses across the finned tube bundle would result in a dry-cooled plant efficiency comparable to that which is realized by wet-cooled power plants.

Standalone condenser performance has been demonstrated to have a significant impact on overall plant performance and efficiency. (Lin, 2016) investigated the plant-level impact by analyzing an ACC thermal-hydraulic performance model in conjunction with Rankine and combined cycle power plant thermodynamic models. Air-side and steam-side heat transfer correlations were selected based on their applicability to the geometry of an ACC, and air-side pressure losses were calculated based on the analysis by Kröger (1998) to obtain the electrical fan power required to condense the steam. She analyzed an ACC module and compared several air-side geometries and enhancement solutions to determine the one that would maximize heat rejection performance of the condenser. It was determined that by optimizing the fin pitch, height, and thickness the ITD for a given condenser could be decreased by roughly 15°C with an associated air-side pressure drop increase of less than 50% (from 144 Pa to 261 Pa). With a more thorough understanding of how ACC performance maintains a critical role in maximizing overall plant efficiency, Rankine and combined cycle thermoelectric power plant models were developed and coupled with the ACC design code to calculate the net power outputs and cycle efficiencies based on the varied parameters in the standalone condenser models. Figure 2.6 compares the maximum predicted Rankine and combined cycle efficiencies for baseline, optimized, louvered, and wavy fin geometries.

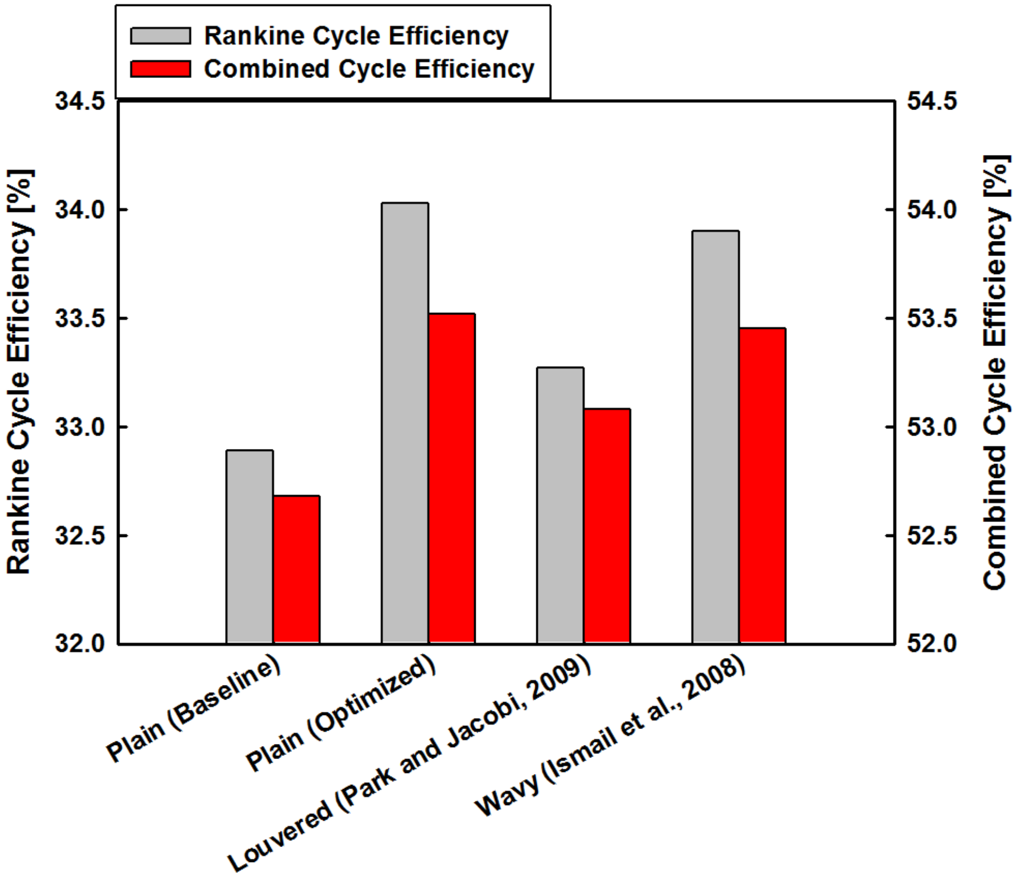

Figure 2.6 Rankine and combined cycle efficiencies (Lin, 2016)

While louvered and wavy fin geometries offered increased cycle efficiencies relative to the baseline fins, the optimized plain fin geometry was shown to realize the largest increase in Rankine and combined cycle efficiencies, with increases ranging from approximately 32.9 to 34% and 52.7 to 53.5%, respectively. This is primarily a result of the large increase in fan power caused by increased pressure drop across the louver- and wavy- fin ACC geometries. Despite having improved ITDs and decreased back pressure at the turbine exit in comparison with the baseline geometry, the wavy and louvered fins cost the plant in net work output, a result of the increased fan power required to force air across the ACC module, and subsequently lowered the overall energy efficiency.

The siting restrictions resulting from poor ACC performance in elevated ambient temperatures have a major impact on the feasibility of ACC selection for use in thermal power plants. To alleviate these issues, Gadhamshetty *et al.* (2006) introduced a method of thermal energy storage (TES) for pre-cooling the inlet air to the ACC module. Using low-grade waste heat from a 500 MW combined cycle power plant, an absorption refrigeration unit was designed to maintain a low temperature coolant reservoir for precooling purposes upstream of the ACC fans. A lithium-bromide/water (LiBr-H_2O) working pair was selected for use in the TES absorption cycle, and analysis demonstrated a required coolant storage volume of approximately 4,500 m^3 to ensure adequate air precooling in all anticipated ambient conditions. They found that this volume of stored refrigerant would allow for consistent preconditioning of air to 20°C in ambient temperatures up to 40°C. Based on subsequent sensitivity analyses, it was determined that the coolant storage tank volume is heavily sensitive to the required inlet air temperature to the ACC module, and the volume of the tank can be reduced by approximately 25% if the required inlet air temperature is increased to just 21°C, with further gains realized at higher inlet air temperatures. The use of a LiBr-H_2O absorption refrigeration system would lead to significantly higher capital costs during plant construction; therefore, minimizing the required tank volume would play a significant role in facilitating the installation and use of such a system. Using the TES absorption system, the power losses would be approximately 2.5% less than those associated with the current practice of throttling the turbine outlet flow to change the total turbine backpressure and corresponding steam saturation temperature. The effect of the pre-cooling heat exchanger on upstream fan pressure losses was not evaluated, and if significant, would have a large detrimental impact on fan power consumption.

2.3 Summary

Numerous investigations have focused on maximizing the air-side heat transfer characteristics in air-coupled heat exchangers. While large variation exists between tube-side condensation heat transfer coefficient correlations, the literature review presented here has demonstrated that air-side convective transport enhancement is currently most critical to maximizing ACC performance. While standalone performance of an air-cooled condenser is important, the primary factor determining widespread implementation is the extent of enhancement that can be achieved without excessive fan power penalties to yield improved plant-level performance. Several investigators have focused on the plant-level performance of dry-cooled Rankine and combined cycle power plants.

Auto-fluttering reed technology is one of the proposed technologies that has the potential to improve ACC performance by lowering the ITD without a commensurately large increase in air-side pressure drop and the corresponding parasitic fan losses. Enhancement factors on the heat transfer coefficient of up to 1.8 times have been reported in previous experimental studies, with the effective coefficient of performance (defined as the ratio of heat transfer output to fluid power input required) increasing by a factor of approximately 2.4. Minimizing the fluid power required to reject a given amount of heat from a condenser tube was determined to be a critical factor in ACC performance, particularly in regions where large ambient temperature swings can have a large impact on the steam condensation temperature as well the resulting overall plant efficiency.

Previous evaluations of autonomously fluttering reeds have yet to investigate the plant level impacts of their implementation, as well as the feasibility of inserting a flag-like structure into the millions of air channels on an ACC. These criteria are important to determining the potential for AFRs to improve air-cooled condenser performance. The investigation described in the later chapters of this thesis reports plant-level performance gains that can be realized using AFRs, as well as insight into the installation feasibility of such a system modification.

CHAPTER 3: EXPERIMENTS

A wind tunnel coupled heated water test facility was designed and manufactured to investigate the air-side heat transfer and pressure drop characteristics representative of ACC tube bundles. This chapter describes the design and development of the heated water test facility and ACC test section, as well as the testing procedures used for heat transfer and pressure drop measurements and analyses.

3.1 Air-Cooled Condenser Wind Tunnel Test Facility

A wind tunnel coupled heated water test facility was fabricated to measure the heat transfer and pressure drop characteristics of an ACC with and without AFR enhancement. The test facility had a total heat supply capacity of approximately 15 kW with water flow rates up to 0.45 kg s^{-1}. High accuracy pressure transducers and a flow meter, along with thermocouples and RTDs for temperature measurement, recorded the test section temperatures and pressures from which the air-side heat transfer coefficient of the baseline and reed-enhanced condenser was calculated. An air-side flow meter and differential pressure transducer recorded the flow rate and pressure drop across the test section, from which the friction factor was evaluated. The following sections describe the water- and air-side components and instrumentation that allow for accurate measurements.

3.1.1 Heated Water Loop Infrastructure

A pressurized single-phase water facility was designed and constructed to provide heated water to the inlet of the ACC test section. Single-phase water was selected over the use of condensing steam for several reasons, the most significant of which is the increased uncertainty associated with the measurement of phase-change heat duty on the tube side, compared to single-phase heat duty measurement. Two-phase flow instabilities through the test section could also have led to intermittency and flow distribution problems. The test facility would also have been much more complicated with the need for upstream and downstream conditioning of the condensing steam, and the associated higher heat load and test loop components.. The water leaving the pump is first heated by two 10.5 kW Watlow electric resistance circulation heaters (Model: CBDNF29R3S) to the temperature desired at the test section inlet. Figure 3.1 demonstrates the overall test facility configuration and instrumentation locations.

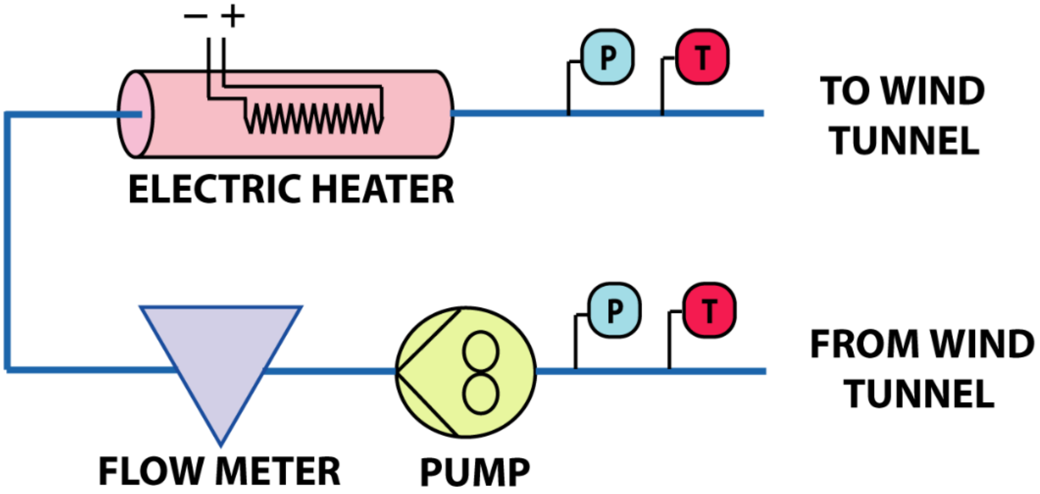

Figure 3.1 Schematic of wind tunnel test facility

The electric heater power levels were established using a Watlow PID controller (Model: PM6C2CJ) connected to a T-type thermocouple at the outlet of each heater. These thermocouples are used for control of the heaters and are not calibrated. The PID controller determined the time averaged state of the Watlow solid-state relay (SSR) device (Model: DB20-24C0), an electric switch that opens and closes at a variable frequency based on the required heat load, allowing an electric current to pass through the resistive circuit within the circulation heaters. The installation of PID controllers ensured safe operation of the heaters and precise control of wind tunnel inlet water temperature. An auxiliary 1 kW cartridge pre-heater was installed immediately upstream of the first circulation heater, which enabled an increase in the overall power input capabilities of the test facility.

The heated water flows into the wind tunnel before entering the test section at the top of the first tube, where it is distributed amongst the parallel rectangular flow channels in the test section tubes. At the exit of the rectangular channels, the flow is recombined and directed to the return bend at the bottom of the test section. The flow pattern is repeated until the water exited the test section at the top of the fourth ACC tube section. T-type thermocouple measurements at the inlet and exit of the test section provided a redundant heat transfer measurement with which the RTD measurements are validated. Figure 3.2 presents a view of the ACC test section as seen from the downstream direction, demonstrating the water flow direction along the length of the tubes.

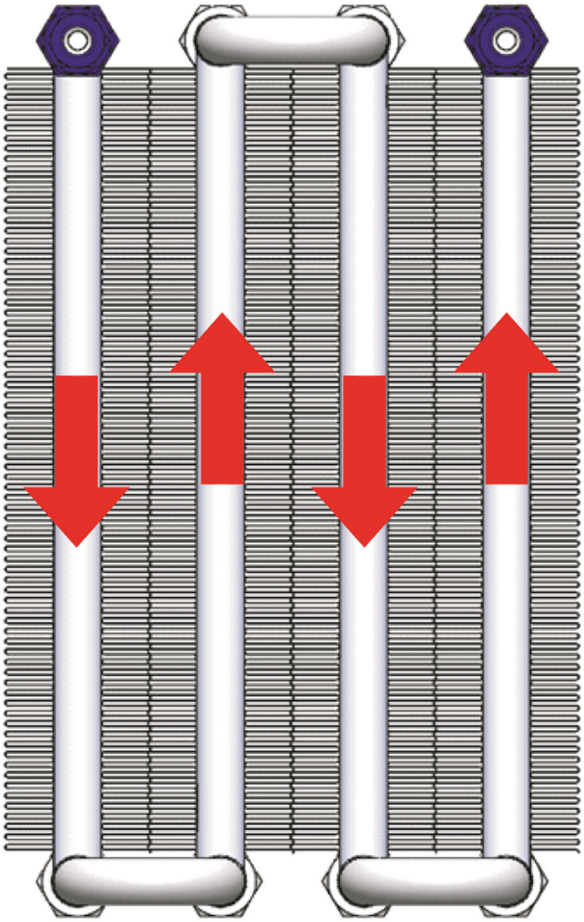

Figure 3.2 Serpentine flow path through test section

Heat is transferred from the hot liquid water through the fin channels to the air flow supplied by the wind tunnel. The water flow is driven by a Liquiflo (Model: H7F) positive displacement pump located immediately downstream of the exit of the wind tunnel. The pump is magnetically coupled to a Leeson Motors variable voltage DC motor (Model: C4D17FC42B) with a manual controller. Temperature trimmed gears, shaved at the gear tips to allow for thermal expansion at high temperatures, are selected for use in the pump to avoid excess mechanical wear during testing at the elevated temperature conditions.

A Parker high-pressure piston-accumulator (Model: ACP05) installed immediately downstream from the discharge port of the pump allowed for thermal expansion of the water during facility start-up as well as pressure control by adding compressed air to the reservoir or by bleeding off compressed air from the accumulator.

Table 3.1 includes the manufacturers and model numbers for the various test facility components and assemblies described above.

Table 3.1 Water Loop Instrumentation and Uncertainty Information

Facility Component	*Manufacturer*	*Model Number*
Pump Head	Liquiflo	H7F
Pump Motor	Leeson Motors	C4D17FC42B
Piston Accumulator	Parker	ACP05
Circulation Heater	Watlow	CBDNF29R3S
PID Controller	Watlow	PM6C2CJ
Solid-state Relay (SSR)	Watlow	DB20-24C0

3.1.2 Heated Water Loop Instrumentation

The primary source of uncertainty in the air-side heat transfer coefficient is the temperature difference along the length of the test section. Data reduction and the minimization of uncertainty in the heat transfer calculations required accurate characterization of the water flow rate and temperature difference across the ACC test section. Temperatures at the inlet and exit of the condenser are measured using high-accuracy four-wire platinum RTD sensors. Four-wire RTDs benefit from higher accuracy and superior lead wire resistance cancelation compared to the standard three-wire RTD. The RTD sensors were inserted in the water flow in the header region at the inlet and outlet of each finned test section tube. Figure 3.3 illustrates the orientation and insertion of the 228.6 mm long RTD as situated within the flow path.

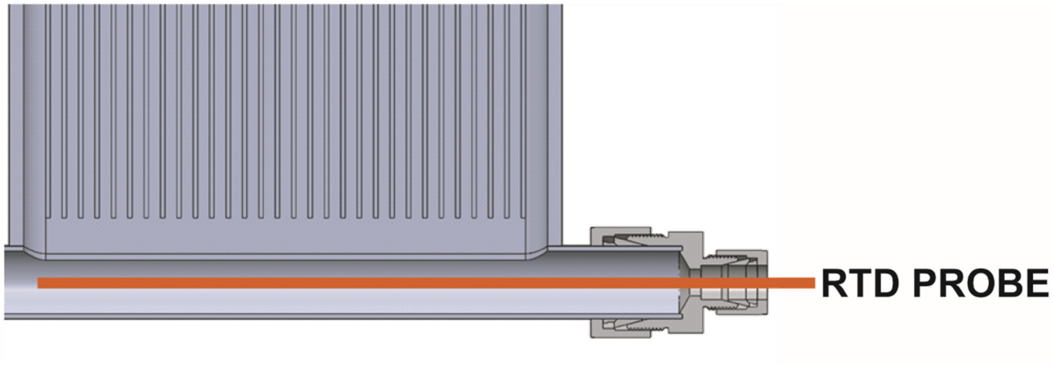

Figure 3.3 RTD installation shown at bottom of test section tube

While the RTDs measure the temperature variation along the length of the ACC test section, there are also thermocouples at the inlet and exit of the test section that measure the temperature drop across the unit for validation of the RTD measurements. Figure 3.4 demonstrates the locations of the temperature measurements relative to the area of the test section exposed to air flow within the AHU.

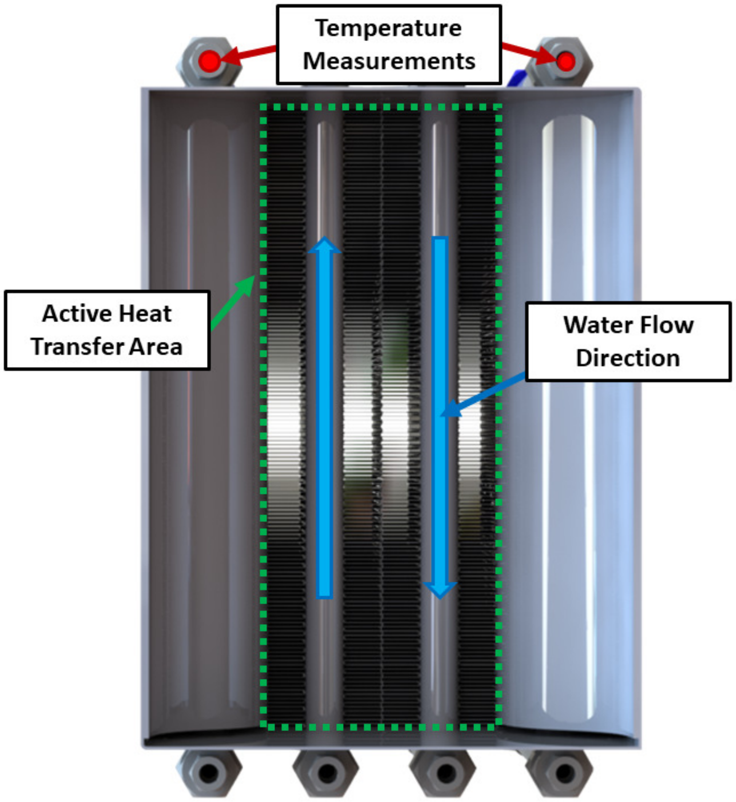

Figure 3.4 Temperature sensor locations in test section

Another important parameter that contributes to the uncertainty in the air-side heat transfer coefficient is the water flow rate. The volumetric flow rate was measured with a high accuracy Micro Motion Coriolis flow meter and transmitter with uncertainty equal to 0.2% of the measurement. Table 3.2 includes the manufacturer and model information and associated uncertainty and measurement ranges for each instrument used to characterize the water-side parameters in the test facility.

Table 3.2 Water Loop Instrumentation and Uncertainty Information

Measurement Type	*Manufacturer*	*Model*	*Uncertainty*	*Range*
Absolute Pressure	Rosemount	2088	0.25%	0 – 5515 kPa
Flow Rate	Micro Motion	CMF025K319 NQBUEZZZ	0.2%	0 – 30 Lpm
Temperature (TC)	Omega Engineering, Inc.	TT-T-30-SLE	± 0.25°C	50 – 120°C
Temperature (RTD)	Omega Engineering, Inc.	P-M-A-1/4-3-1/2-PS-12	± 0.12°C	50 – 120°C

The thermocouples and RTDs used in the test section were calibrated in a Hart Scientific silicone oil bath (Model: 7340) across a temperature range from 50 – 120°C to encompass the conditions encountered by the sensors during testing, accounting for hysteresis by obtaining calibration points with increasing and decreasing bath temperatures. The calibrated oil bath accuracy was 0.10°C. The water pressure and flow rate measurement uncertainties were based on factory calibration settings. Facility-level temperatures used for controlling the specific data point testing conditions were measured using T-type thermocouples. These measurements were not directly used in calculation of the air-side heat transfer or pressure drop and as such were not critical to minimizing the heat transfer coefficient uncertainty.

The water pressure was measured from the test facility piping immediately upstream and downstream of the wind tunnel penetrations. Rosemount pressure transducers were used, with the lower span calibration point set to the ambient pressure of the room while disconnected from the test facility. The differential water pressure across the two pressure taps was assumed to vary linearly throughout the length of the test section for the purposes of calculating the thermophysical properties of the water as a function of pressure and temperature. The thermophysical properties are weak functions of pressure and as such this assumption does not adversely affect the accuracy of the results.

3.1.3 Air-Handling Unit

The air-handling unit (AHU) supplied air flow through the ACC test section fin channels. The AHU consists of a variable speed fan, chilled water and steam heat exchangers, and a converging section with inlet and outlet flow straighteners. The flow rate, temperature and relative humidity of the flow in the wind tunnel were monitored using a Johnson Controls User Interface. To minimize air-side maldistribution, the air flow was smoothly reduced in area from the full cross-sectional area of the wind tunnel to the total frontal area of the ACC test section upstream of the final flow straightener located immediately before the test section. Figure 3.5 illustrates the overall configuration and air flow path of the STSL AHU, as well as the location of the flow straighteners, heat exchangers, humidity controls, and measurement instrumentation.

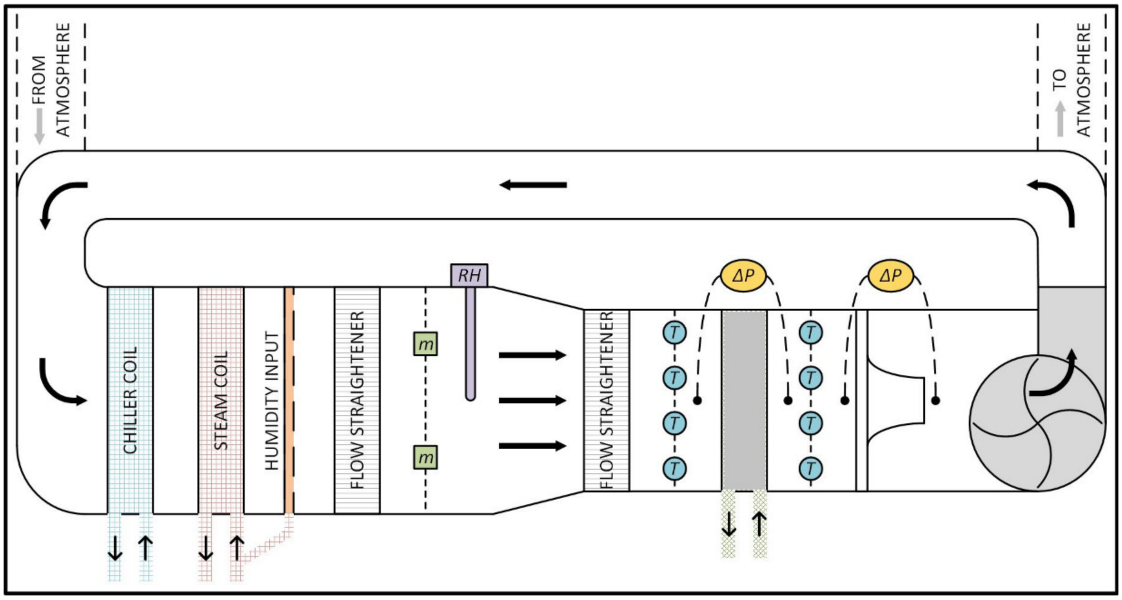

Figure 3.5 Air-handling unit layout demonstrating location of ACC test section (Forinash, 2015)

The AHU offered the flexibility to adjust air flow over a wide range of temperature, velocity, and humidity conditions. These conditions were recorded simultaneously with the water-side measurements for data reduction using EES. For this study, the air was pre-cooled before flowing through the heated test section to ensure adequate heat rejection rates, thereby minimizing heat transfer coefficient uncertainties. The pre-cooled air temperature was controlled by adjusting the cutoff valve on the chilled water lines connected to a five-row chilled water heat exchanger located in the wind tunnel as well as by adjusting the chilled water supply temperature set-point in the chiller control system.

3.1.4 Air-Side Instrumentation

The air-side measurements play a critical role in understanding the heat transfer and pressure drop through the air channels with and without reeds. A nozzle flow meter with low-span differential pressure transducer located immediately downstream of the ACC test section was used to calculate the air mass flow rate through the core of the condenser test section. Bernoulli’s equation was applied along a streamline down the center of the converging section assuming steady and incompressible, inviscid, and adiabatic flow conditions along a streamline through the nozzle. The nozzle was assumed to be an ideal contraction with predicted discharge equal to actual discharge through the nozzle. The variance of discharge rate with the inclusion of a discharge coefficient is minimal, with most predictions for discharge coefficient ranging from 0.95 – 0.97. The nozzle discharge coefficient was calculated by the approach of Hall (1959), yielding an approximate discharge coefficient of 0.964 as demonstrated by Appendix A. With a high discharge coefficient, the uncertainty applied to the nozzle flow meter encompasses the variation of discharge rates due to viscous effects and boundary layer development through the length of the nozzle.

With the differential pressure measured and inlet and exit nozzle areas known, the test section mass flow rate was calculated by solving the following system of three equations and three unknowns, neglecting the gravitational terms.

$$\dot{m}_{nozzle} = \rho_{nozzle} \cdot A_{nozzle,in} \cdot V_{nozzle,in} \tag{3.1}$$

$$\dot{m}_{nozzle} = \rho_{nozzle} \cdot A_{nozzle,out} \cdot V_{nozzle,out} \tag{3.2}$$

$$\Delta P_{nozzle} = \left(\frac{\rho_{\mathrm{nozzle}}}{2}\right) \cdot \left(\mathrm{V_{nozzle,out}}^{2} - \mathrm{V_{nozzle,in}}^{2}\right) \tag{3.3}$$

One of the concerns pertaining to air-side measurements is flow maldistribution across the height and width of the wind tunnel cross-section. While the air flows through several components, including the multi-row chilled water heat exchanger as well as flow straighteners before entering the test section, transverse temperature and velocity variations are still possible. The characterization of these variations and corresponding adjustment to the data reduction techniques was critical to accurately determining the enhancements due to AFR installation. An uncertainty of 10% was applied to the differential pressure measured across the nozzle flow meter to account for slight imperfections in the location of pressure taps at the inlet and exit of the nozzle.

To validate the air-side flow rate measurements and characterize the velocity variations across the face of the ACC test section, steady-state vane anemometer readings were recorded with an Omega Metal Vane Anemometer (Model: HHF803) at nine locations over the flow area before installation of the test section. The velocity measurements yielded an average flow velocity of 2.27 m s^{-1} corresponding to a predicted nozzle-measured velocity of 2.24 m s^{-1}. The standard deviation of measurements was 0.061 m s^{-1}. A velocity profile, in the horizontal and vertical directions, within the wind tunnel flow area was expected to develop based on the boundary layer development along the length of the wind tunnel leading up to the test section. The effect of this boundary layer was minimal, demonstrated by the small variation in velocity measured at the nine locations across the flow area. The close agreement between nominal flow velocity and average flow velocity, in addition to the low standard deviation amongst the nine measurements, confirmed the relatively low maldistribution in the air-side flow. Installation of the test section could impact the flow distribution, and as such, maldistribution could not be entirely discounted.

Air-side absolute pressure measurements were obtained at the inlet to the ACC test section with an Omega pressure transducer (Model: PX02K1-26A5T). Absolute pressure plays a minimal role in the heat transfer calculations, and this measurement is only used for the evaluation of thermophysical properties of the bulk air-flow. The absolute pressure varies slightly along the length of the ACC test section.

An array of wire T-type thermocouples was constructed and installed approximately 25 mm from both the leading and trailing edges of the ACC test section to measure the air-side temperature distribution entering and leaving the fin channels. Three 0.32 mm diameter metal wires were strung vertically along the test section to secure the thermocouples in place while minimizing the impact on air-side flow distribution. Thermocouples were made with 0.254 mm thermocouple wire with a thermocouple welder before calibration in a silicone oil bath across the range of testing conditions. The calibrated T-type thermocouples were attached to the metal wire strung along the height of the test section with shrink tubing. An array of thermocouples was installed in front and behind of each bank of aluminum fins across the width of the test section, and the air-side temperature was measured along the height of the tube at three locations vertically, as illustrated in Figure 3.6. This yielded nine thermocouple measurements (solid red circles) in a three by three grid, which was used to calculate the average air temperatures at the inlet and outlet of the test section.

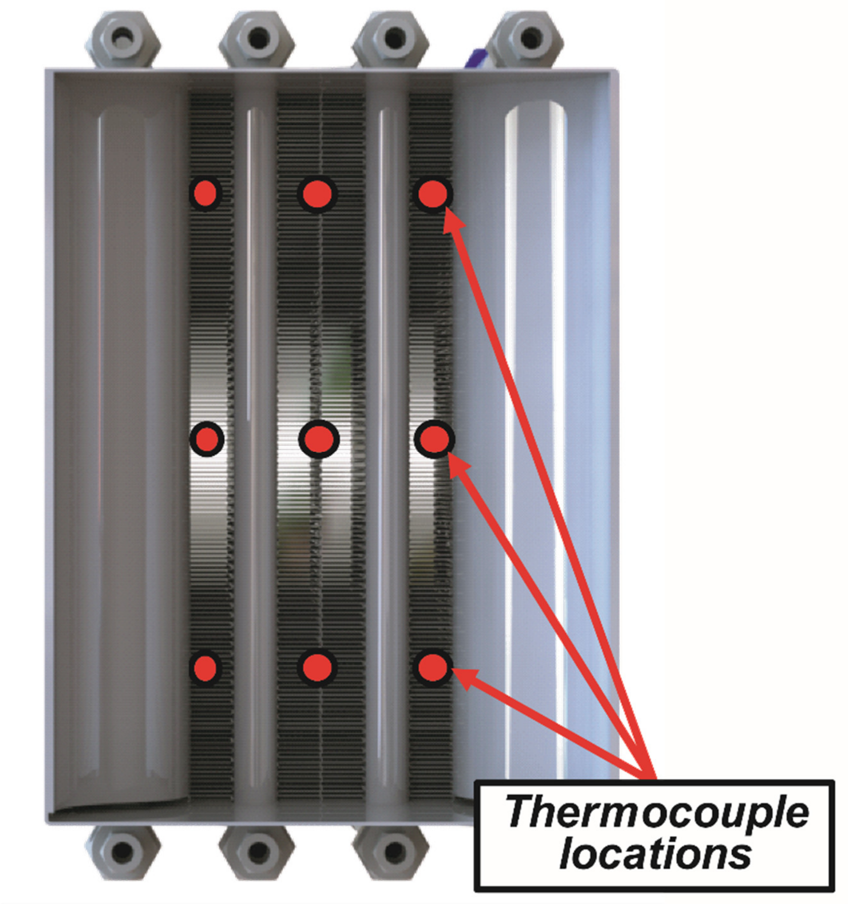

Figure 3.6 Air-side thermocouple locations (front and back)

One of the primary factors driving the design and implementation of air-side enhancement techniques on ACCs is the associated increase in air-side pressure drop. The differential pressure across the ACC test section was measured with a Dwyer low-range differential air pressure sensor (Model: 607-3). The sensor was vibration-isolated from the wind tunnel using a rubber damping mat separating the sensor and the AHU, minimizing fluctuation in the measurements. The differential total pressure was averaged across the width of the wind tunnel at the inlet and exit of the ACC test section with a Dwyer averaging pitot tube (Model: PAFS-1002), approximately 102 mm from the leading and trailing edges of the air channels. Differences in dynamic velocity are minimal in the test section as a result of the constant cross-sectional area through which the differential pressure is measured. The decrease in dynamic pressure is accounted for by calculating the reversible expansion pressure drop as the air passes through the test section and adjusting the measured pressure drop accordingly. Selected tests were repeated to ensure that the use of total pressure difference was valid by measuring the difference based on the static pressure ports, with differences in pressure drop on the order of 1 – 2 Pa relative to the total pressure drop measurement. Table 3.3 details the air-side instruments and their associated uncertainties and measurement ranges.

Table 3.3 Air-Side Instrumentation and Uncertainty Information

Instrument Type	*Manufacturer*	*Model*	*Uncertainty*	*Range*
Absolute Pressure	Omega Engineering, Inc.	PX02K1-26A5T	2.5%	88 – 108 kPa
Differential Pressure	Dwyer Instruments, Inc.	607-3	5.0%	0 – 250 Pa
Temperature	Omega Engineering, Inc.	TT-T-30-SLE	± 0.25°C	10 – 80°C
Relative Humidity	Johnson Controls	HE-67P2-0N00P	2.0%	20 – 80%

3.1.5 Data Acquisition System

A National Instruments CompactDAQ eight-card chassis is used in conjunction with four different National Instruments data acquisition cards to acquire the measurement signals from the water-side and air-side instrumentation. Table 3.4 lists the data acquisition cards used in the DAQ system in the wind tunnel test facility.

Table 3.4 National Instruments Data Acquisition Cards

DAQ Card Type	*Model Number*	*Quantity*
RTD (4-wire)	NI 9216	2
Thermocouple (w/ CJC)	NI 9213	3
Current (± 20 mA)	NI 9203	1
Voltage (± 10 V)	NI 9209	1

The raw measurement signals from the test facility instrumentation are recorded and processed using a data acquisition program developed in NI LabVIEW 2016 (32-bit). The virtual instrument, or VI, consists of the front panel, block diagram, and connector diagram. The VI allows for operator selection of sampling frequency and the number of samples to record, as well as text input fields for defining the data file name and location. Upon starting the test facility VI, the LabVIEW program begins preparing a buffer of test facility measurement data for a user-defined test length which at any point can be output to an excel spreadsheet and copied into EES for data reduction and uncertainty analysis. A screen capture of the test facility data acquisition LabView program is included in Figure 3.7.

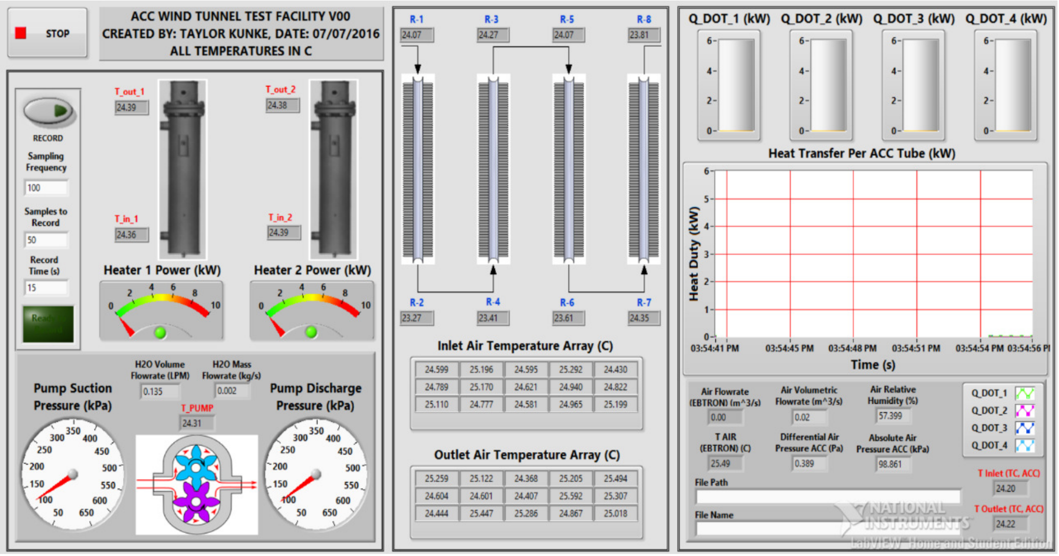
ACC WIND TUNNEL TEST FACILITY V00
CREATED BY: TAYLOR KUNKE, DATE: 07/07/2016
ALL TEMPERATURES IN C

Sampling Frequency: 100
Samples to Record: 50
Record Time (s): 15

T_out_1: 24.39
T_in_1: 24.36
T_out_2: 24.38
T_in_2: 24.39
H2O Volume Flowrate (LPM): 0.135
H2O Mass Flowrate (kg/s): 0.002
T_PUMP: 24.31

R-1: 24.07
R-3: 24.27
R-5: 24.07
R-8: 23.81
R-2: 23.27
R-4: 23.41
R-6: 23.61
R-7: 24.35

Inlet Air Temperature Array (C)

24.599	25.196	24.595	25.292	24.430
24.789	25.170	24.621	24.940	24.822
25.110	24.777	24.581	24.965	25.199

Outlet Air Temperature Array (C)

25.259	25.122	24.368	25.205	25.494
24.604	24.601	24.407	25.592	25.307
24.444	25.447	25.286	24.867	25.018

Air Flowrate (EBTRON) (m^3/s): 0.00
Air Volumetric Flowrate (m^3/s): 0.02
Air Relative Humidity (%): 57.399
T AIR (EBTRON) (C): 25.49
Differential Air Pressure ACC (Pa): 0.389
Absolute Air Pressure ACC (kPa): 98.861
File Path
File Name
T Inlet (TC, ACC): 24.20
T Outlet (TC, ACC): 24.22

Figure 3.7 LabVIEW VI for data acquisition

3.2 Air-Cooled Condenser Test Section Design

An ACC test section was designed and manufactured to simulate the forced air convective heat transfer and pressure drop across a representative section of an air-cooled condenser module.

3.2.1 ACC Test Section Geometry

ACC modules consist of large hydraulic diameter, high aspect ratio condenser tubes with air-side fins on both sides to maximize the air-side heat transfer area. To determine the effectiveness of the AFRs in enhancing the air-side heat transfer coefficient, it was necessary to match the representative outer dimensions for ACC condensation tubes in the lab-scale test section. The ACC test section consists of four individually finned condenser tube sections, each 0.42 m in length. Each tube section has one bank of corrugated aluminum fins on each of its two flat faces. Swagelok stainless steel tube fittings on the end of eight header tubes are used to insert NPT-threaded RTD temperature sensors into the flow. Reducing compression fittings on the inlet and exit tubes of the test section allow for plumbing of the test section to the heated water test facility tubing. Return bends are welded on to the ends of the header tubes to route the flow through the test section. Figure 3.8 shows an isometric view of the ACC test section before installation of the Swagelok fittings, converging section, and sheet metal shroud.

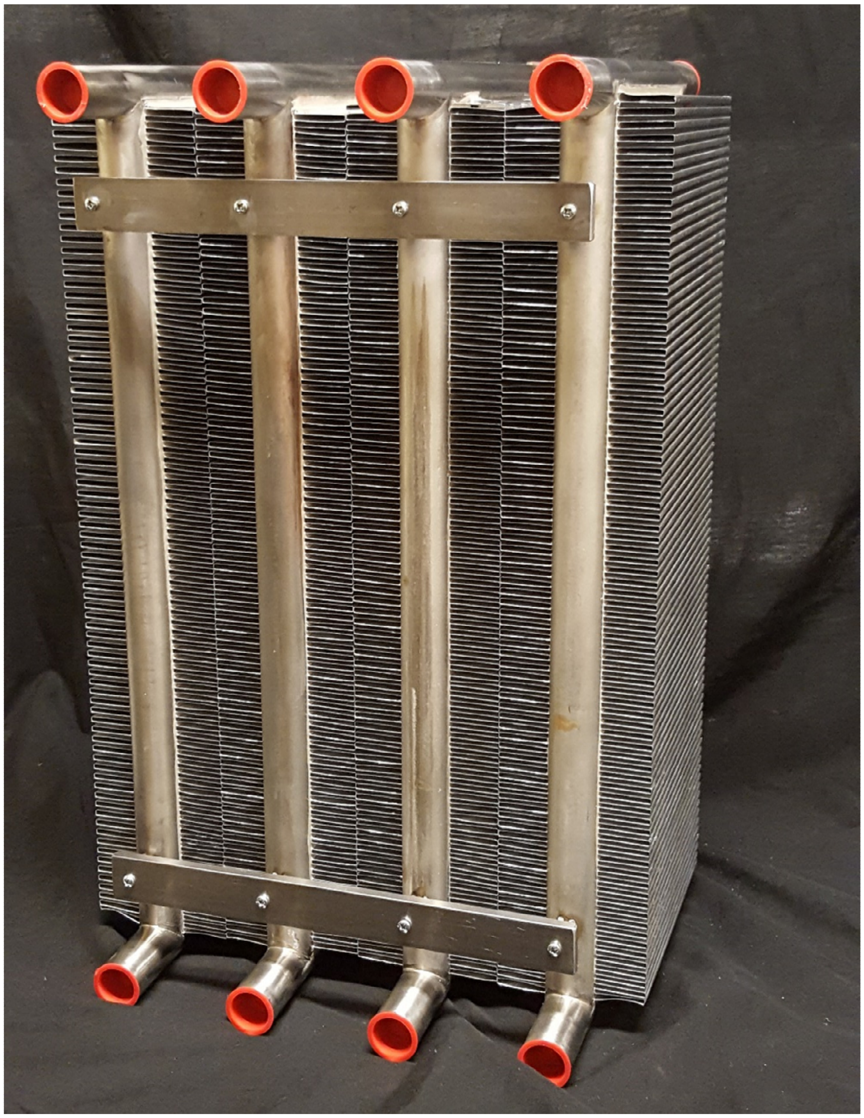

Figure 3.8 ACC test section before installation of fittings and shroud

Several unique design considerations must be accounted for while designing and manufacturing a representative ACC test section. Industry ACCs operate at sub-atmospheric pressures with condensing steam on the inside of the tubes and as such can utilize low tube thicknesses to minimize the conduction thermal resistance through the tube. The test section developed for use in this study uses single-phase water for heat input to minimize heat transfer uncertainty, and with a maximum temperature of approximately 115°C, requires pressurization to prevent boiling or cavitation within the pump. Assuming a water saturation pressure of approximately 170 kPa corresponding to a saturation temperature of 115°C, a design pressure of 400 kPa was selected to ensure adequate margin from boiling in the heaters and test section and to mitigate the risk of damaging the pump due to cavitation. Structural analyses were performed using ANSYS Academic Research software, Release 16.1 to determine the required wall thickness to support the increased internal pressure compared to an ACC tube. Based on this investigation, the tube wall thickness was increased from 1.27 to 4.76 mm to ensure that the flat tubes would not burst or bow during testing. The predicted stresses at the maximum design pressure in the test section were several orders of magnitude lower than the yield strength of stainless steel.

As air-side heat transfer characteristics are the focus of this investigation, the outer dimensions of the ACC tube section matched the dimensions used in power plant air-cooled condensers. Table 3.5 lists the dimensions for the ACC condenser tubes for the wind tunnel test section.

Table 3.5 Test Section Tube Dimensions (Figure 3.9)

Dimension Name	*Dimension Label*	*Value (mm)*
Tube Flat Length	**A**	25.4
Tube Thickness	**B**	4.73
Rib Channel Width	**C**	4.38
Bullnose Diameter	**D**	12.7
Rib Thickness	**E**	1.27

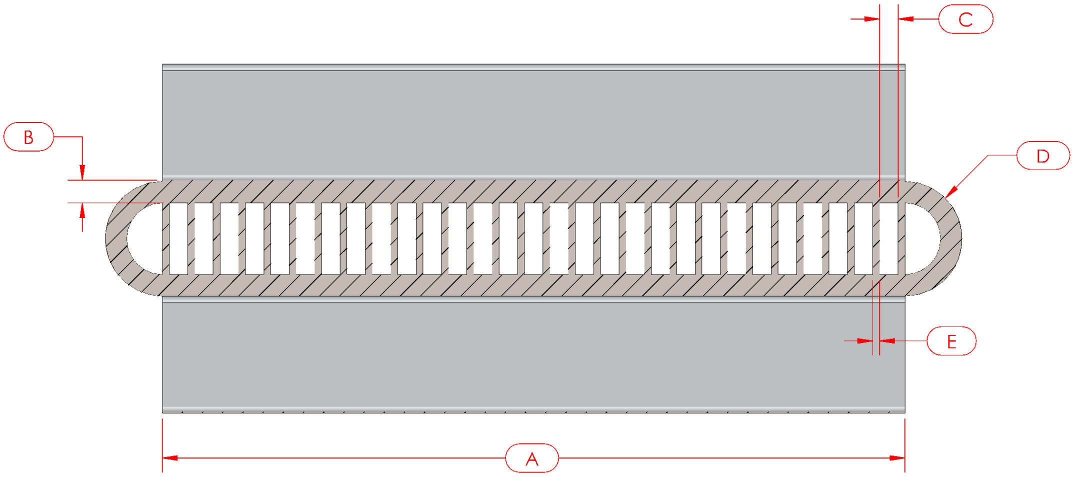

Figure 3.9 Test section dimensions (cross-sectional view)

Fins are installed on both sides of the ACC tubes to increase the effective air-side heat transfer surface area. The corrugated fins that form the air channel walls in the test section were manufactured by folding a thin aluminum sheet into long, rectangular ducts. The ACC test section has a total of six hundred channels through which the air can flow. Table 3.6 lists the fin dimensions for the ACC test section.

Table 3.6 Test Section Fin Dimensions (Figure 3.10)

Dimension Name	*Dimension Label*	*Value (mm)*
Air Channel Width	**A**	2.54
Fin Thickness	**B**	0.254
Fin Height	**C**	25.4

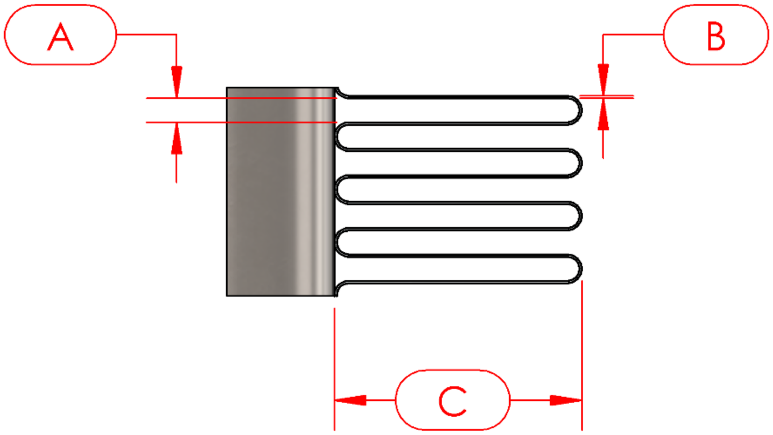

Figure 3.10 Dimensions of air-side fins

The air-side heat transfer coefficient is calculated based on a thermal resistance network between the bulk water and air flows. Therefore, minimizing the water-side thermal resistance is critical to reducing uncertainty in the deduced air-side heat transfer coefficients. By simply increasing the water-side flow rate, the temperature drop along the length of the ACC test section at a given heat rejection rate would decrease and result in an increase in uncertainties in heat duty measurement. Several options for improving the water-side heat transfer performance were considered, including increasing water flow rates and decreasing the tube-side hydraulic diameter to increase the average flow velocity, Reynolds number, and heat transfer coefficient. To minimize the tube-side thermal resistance in the test section, stainless steel strips are brazed to the inside of the ACC tubes, which increase the effective tube-side heat transfer area while simultaneously increasing the average flow velocity and decreasing the hydraulic diameter of the flow passage as illustrated in Figure 3.11.

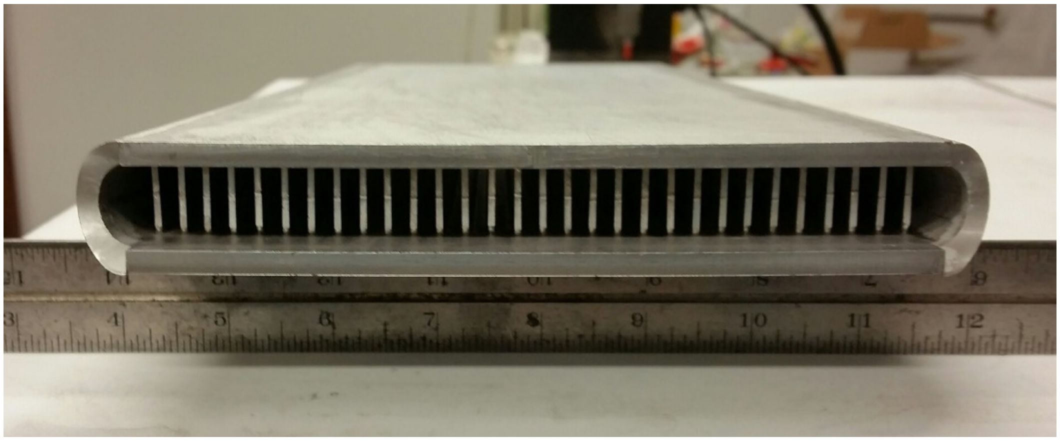

Figure 3.11 View of test section tube during fabrication illustrating rib channels

Decreasing the water-side hydraulic diameter using ribs in the test section results in an increase in the average heat transfer coefficient due to increased flow velocities. The internal rib walls also act as fins on the inside of the tubes, increasing the effective tube-side heat transfer area. The resulting decrease in water-side thermal resistance is important in minimizing the uncertainty in the air-side heat transfer coefficient.

The ACC tube sections were manufactured from stainless steel components to minimize the risk of rusting and other sources of unpredictable fouling resistance buildup between the air and water flows. Flat plates were welded to length-wise ripped pipes to create the flat tube with rounded ends. The fins were folded from a flat sheet of Al 1100 and secured to the flat side of the ACC tube sections using a high thermal conductivity (k = 3.5 W m^{-1} K^{-1}) thermal adhesive, MasterBond Supreme 18TC. A sheet metal enclosure, as shown in Figure 3.12, was designed and fabricated to fit closely around the finned tube array to ensure that the entirety of the air flow would be directed through the test section. The enclosure was assembled around the outermost tubes of the test section before being secured with t-slot framing. The top and bottom of the enclosure had through-holes for air-side thermocouple insertion both 25.4 mm and 76.2 mm from the front fin face allowing for spatial temperature measurements with and without the reed attachment blocks installed. The dimensions for the enclosure height and width were 0.41 m and 0.31 m, respectively.

Manufacturing challenges associated with tolerance runout during assembly brazing resulted in poor channel alignment between tubes one and two, and tubes three and four. Additionally, the outermost bank of air channels on tubes one and four do not have an adjacent tube to secure the outer span of the reed assembly. To manage these issues, the two outermost tubes were blocked with a converging section to redirect the air through only the center tubes. The converging section assembly exploded from tube one is depicted in Figure 3.12.

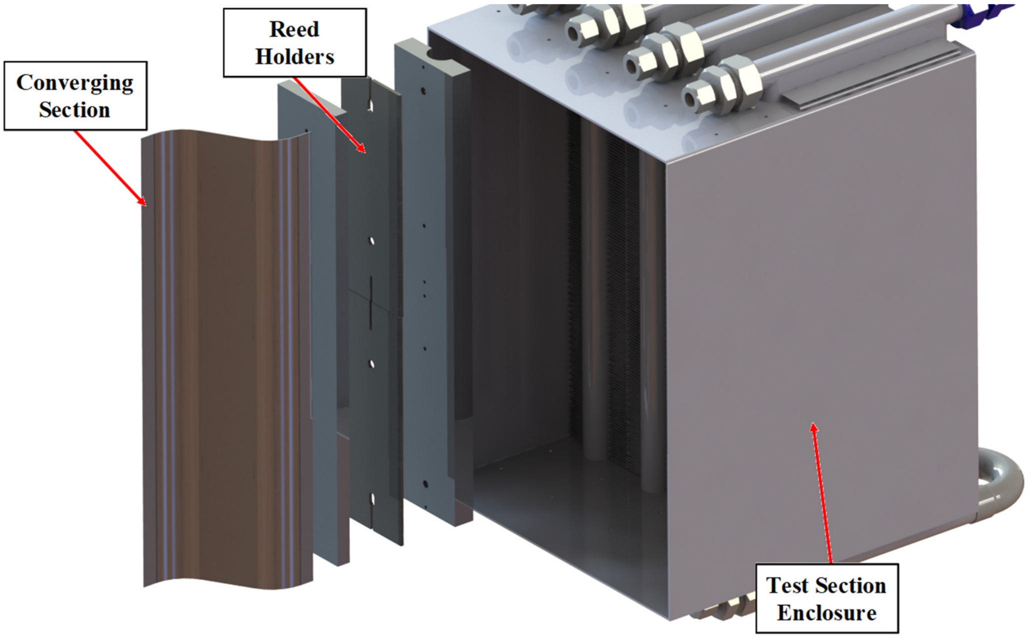

Figure 3.12 Converging section assembly model

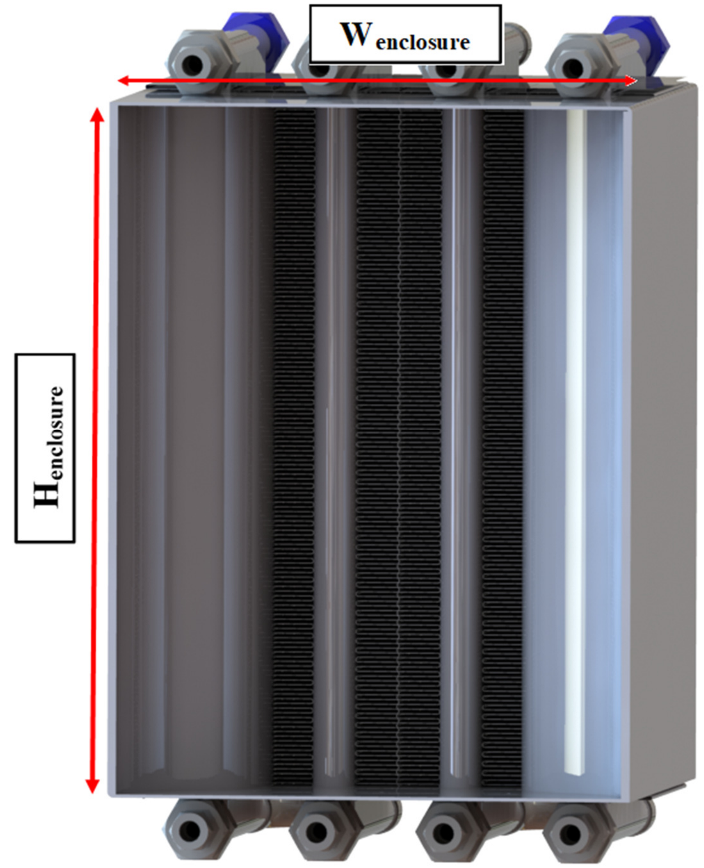

Figure 3.13 Test section assembly model shown with shroud and converging sections installed

The blockage of the outermost tubes allows for the installation of single reed AFR assemblies along the outermost bank of fins on the center two tubes, ensuring that a high percentage of fin channels contain an AFR flag. The converging section assembly includes modified reed holder parts, discussed later in Section 3.2.3, which allow for a single wide reed to be held across the outermost fin channels. Following installation of the converging section, foil tape was used to seal the perimeter of the assembly to the test section shroud and minimize bypass flow around the converging section.

The test section assembly was installed directly downstream of the final flow straightener in the AHU. The forward-most edge of the enclosure was inserted approximately 20 mm into the wind tunnel straight duct, after which it was taped around its perimeter to ensure a proper air flow seal. Ceramic fiber insulation was used to insulate the header regions of the ACC test section, as well as to block any backward recirculation within the wind tunnel. A Morgan Advanced Materials ceramic fiber insulation blanket ($k = 0.06$ W m^{-1} K^{-1}) was also fit to the perimeter of the sheet metal shroud to minimize the heat loss to the ambient air in the wind tunnel, and to ensure accurate air and water heat duty measurements. All penetrations in and out of the wind tunnel were taped to ensure that the system is fully isolated from the rest of the lab environment and to ensure accurate air flow rate measurements from the nozzle flow meter. Figure 3.14 demonstrates the test section location within the wind tunnel test facility.

Figure 3.14 Test section mounted within wind tunnel test facility

3.2.2 Auto-Fluttering Reed Design and Manufacturing

A prototype AFR assembly was developed for testing and analysis in the wind tunnel test facility in collaboration with the Fluid Mechanics Research Lab at Georgia Tech. The AFR assembly consists of two components: two fluttering reeds and a structural post for attachment to the reed attachment block assembly. Each reed was hand cut with a rotary cutter from a sheet of 0.0005” thick PET and then glued to the rigid stainless steel AFR support post. Figure 3.15 illustrates the geometry and dimensions of the AFR and AFR support post.

Table 3.7 Reed assembly dimensions (Figure 3.15)

Dimension Name	*Dimension Label*	*Value (mm)*
Flag Length	**A**	101.6
Flag Width	**B**	19.1
Support Post Length	**C**	57.1
Support Post Width	**D**	2.54

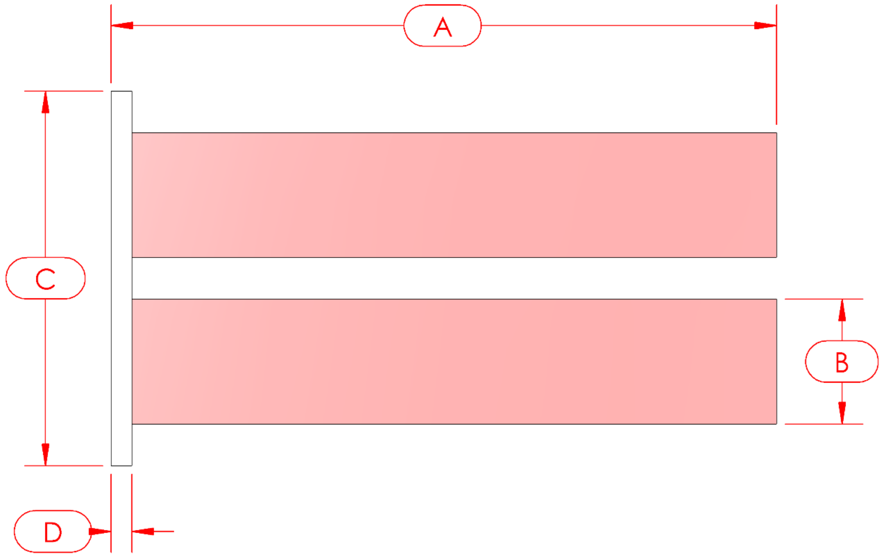

Figure 3.15 Top-view of AFR assembly (flag and support post)

A total of 150 double reed AFR assemblies, each consisting of two independently fluttering reeds, were made and installed into the air channels in between the test section tubes. When channel alignment made installation of the double assembly impractical, one reed was removed from the AFR assembly and a single reed was inserted into the adjacent air channels. In addition to the double reed assemblies, 300 single-reed AFR assemblies were manufactured for installation into the outermost banks of tubes. The flag for the single reed assemblies was of the same dimensions as the double reed assembly, except for a shorter support post 30 mm in length, which was needed to span the width of a single set of air channels on the outermost bank of test section fins. With the inability to insert reeds into each air channel because of channel misalignment, reeds were inserted into approximately 550 out of 600 total air channels.

3.2.3 Reed Attachment Block Design and Manufacturing

A reed attachment block (RAB) assembly was designed and manufactured to align and secure the AFRs inside the air channels during testing without blocking free flow area through the condenser test section. Each tube in the ACC test section had two threaded standoffs welded to the forward-most rounded edge of the tubes, which secured the reed attachment block. The RAB for the center two tubes of the test section, as illustrated in Figure 3.16, consists of four total parts: the base plate (A), upper reed holder (B), lower reed holder (C), and top cap (D). A thin rubber gasket was placed on top of the reed holders before installation of the top cap. During assembly of the RAB, the gasket was pressed into the reed holder cutouts which hold the AFR posts, ensuring that the reed support posts were securely held in place during wind tunnel operation.

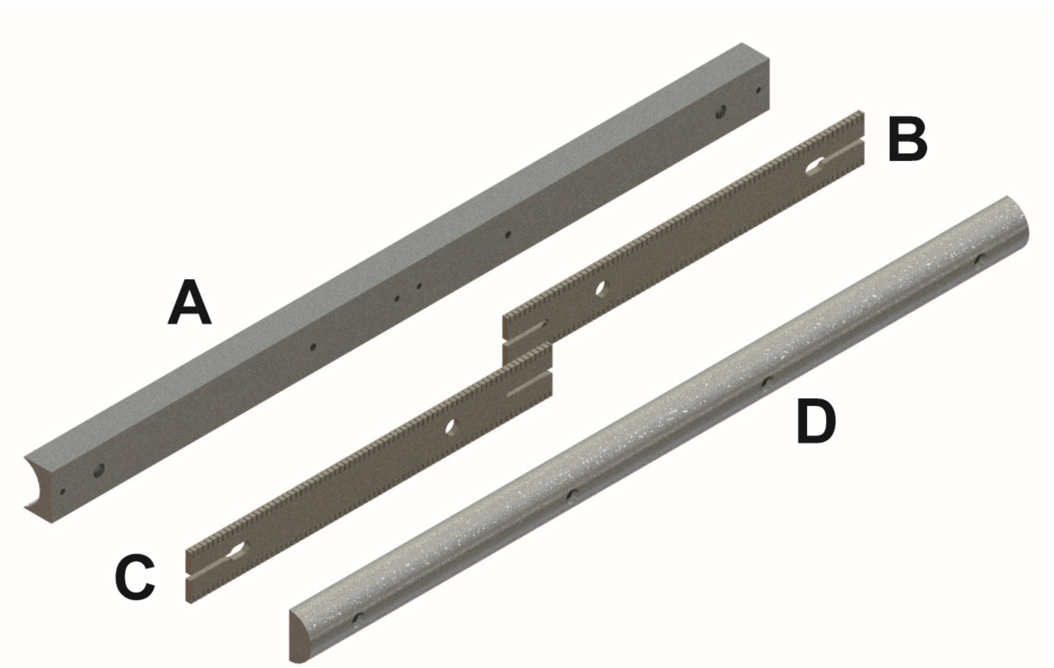

Figure 3.16 Isometric/exploded view of reed attachment block assembly

In addition to the 25.4 mm wide reed holders that fit over the center two test section tubes, 7.62 mm wide reed holders were manufactured for installation within the converging shroud assembly to secure the reeds above the outermost fin channels on the test section. The use of two reed holders, each with a slotted connection allowing for independent translation along the length of the ACC test section tube, made precise adjustment of the reed location within each air channel possible. This adjustment capability was important for the optimization of air-side heat transfer enhancement with AFRs; excessive reed interaction with the walls of the air channel was likely to result in lower AFR performance due to the impulse imparted on the wall reducing the total kinetic energy of the reed. Additionally, reeds in contact with the wall have additional static forces to overcome before unstable oscillation can occur. To mitigate reed-to-wall interactions, as well as to lower the channel velocity associated with the onset of reed flutter, the reeds were carefully aligned towards the top center of the channel for maximum enhancement. The steel reed support posts were cantilevered on either end by the reed holders, which were held between the bottom plate and top cap of the RAB assemblies. The reed holders were adjusted vertically along the length of the test section tubes after reed installation to properly align the reeds within their respective air channels. Figure 3.17 demonstrates the insertion of reeds into the air channels.

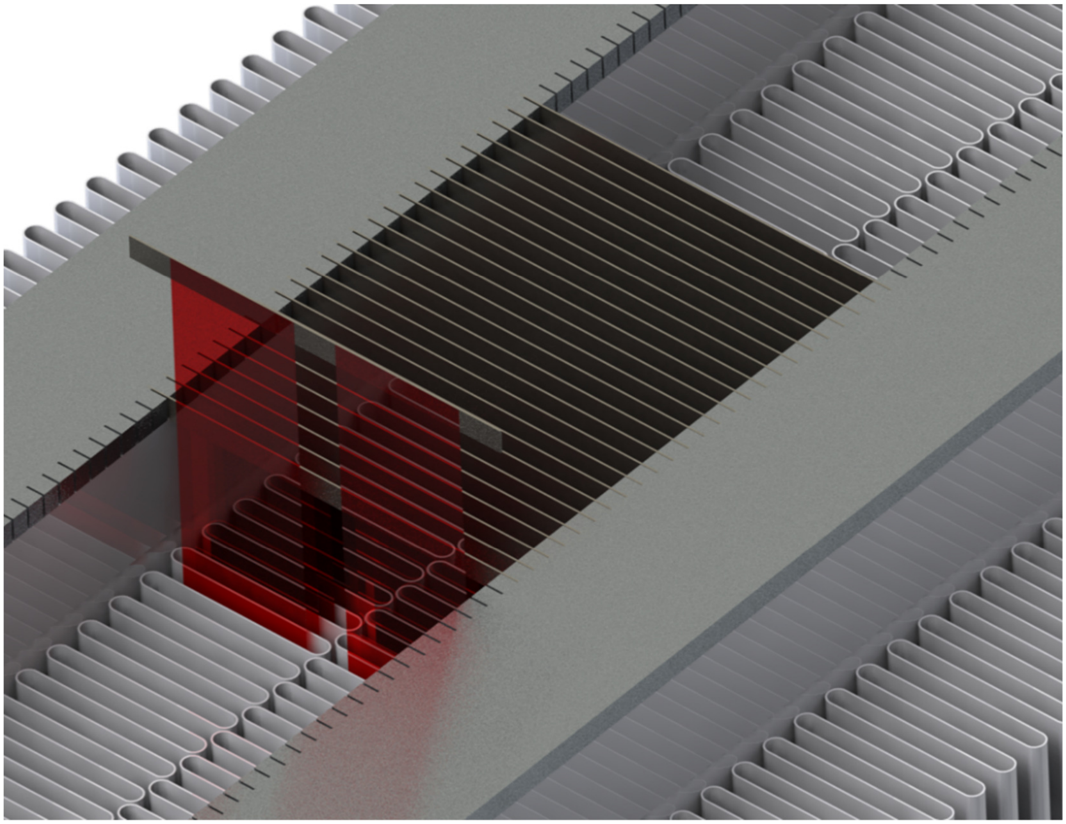

Figure 3.17 Reed attachment and insertion into the center air channels

3.3 Experimental Procedures

The charging process for the water loop is carefully controlled to minimize the ingress of non-condensable gases that would alter water-side heat transfer coefficients and introduce error into the heat transfer coefficient measurements. Figure 3.18 illustrates the overall procedure for acquiring data, followed by a discussion of the specific testing requirements.

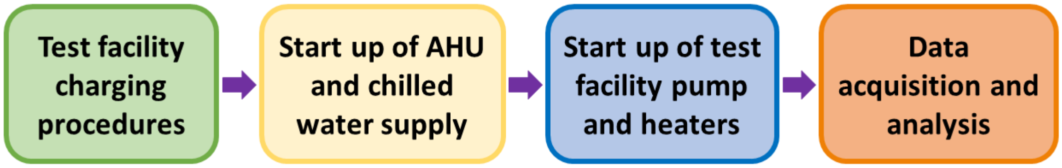

Figure 3.18 Testing procedure

Starting at an uncharged/ambient state, a vacuum pump is connected to the highest point in the system. The piston accumulator is charged with air to the desired system pressure, ensuring the piston is seated against the bottom of the accumulator cylinder. A pressurized water tank is then connected to the low point of the system with the water drain valve closed. Once the air is evacuated from the system, the vacuum pump is turned off and the valve at the top of the test facility is closed. The valve at the water tank is then opened allowing the flow of water into the test facility. Once flow stops, a pressurized nitrogen gas cylinder is used to increase the water tank pressure after which the valve at the highest point of the system is reopened briefly, allowing for a small amount of water to exit into a bucket of water along with any remaining air in the system. The gear pump is then set to the maximum operating speed to entrain any remaining non-condensable gases in the test facility and the top valve in the system is once again opened to allow them to leave the tubing. After the final purge of any non-condensable gasses, all external valves to the test facility are closed and the system was considered fully charged.

To start test facility operation, the gear pump is energized and ramped up to the desired volumetric flow rate as read by the water flow transmitter. The wind tunnel control system is used to close the atmospheric inlet and outlet vents such that the air handling unit is operating in full recirculation mode to ensure precise control over temperature and humidity within the system. The wind tunnel fan is then turned on and the set point varied to reach the desired air-side volumetric flow rate, after which the chilled water valve into the wind tunnel is opened, lowering the recirculating air temperature in the AHU. The chilled water temperature set point is periodically adjusted to pre-cool the air to the desired inlet temperature to the ACC test section.

The high-voltage cutoff switches to the two water-side circulation heaters are then energized and the solid-state relays activated by the PID controllers to control the heat input to the test loop. If necessary for the testing conditions, the switch for the auxiliary cartridge heater is activated to provide an additional 1 kW of heat input to the system. It is critical to ensure proper flow over the electrical heater resistance bundles to mitigate sheath overheating. The system pressure is controlled by bleeding the air pressure reservoir. Adequate water pressure is maintained such that it is at least 20% greater than the saturation pressure associated with the water temperature measured at the gear pump to ensure cavitation does not damage the pump impellors. This pressure margin also ensures boiling does not occur in the electric heaters, which would significantly raise the heater element surface temperature and potentially damage the system. As the test section is heated by the now hot water in the test facility, the inlet air temperature in the AHU increases, requiring continuous adjustment of the valve and temperature set points throughout the testing process.

Data points are collected at steady-state test facility conditions, at a minimum of five minutes following any significant change in flow rate or temperature. This ensures that the test section, which has a relatively high thermal mass, has reached steady state. Selected data points are also analyzed with respect to their temporal variation, ensuring that a steady-state condition is achieved. Data point length and sampling frequency are also important to ensure that the measured data points accurately characterize the test facility conditions. While increased sampling frequency yields data with higher temporal resolution, the intrinsic noise and low amplitude deviations are more significant. A sampling frequency of 40 Hz is selected for data recording with data point lengths ranging from thirty to sixty seconds. The array of data generated in the LabVIEW program is then exported to an Excel file, from which the average channel measurement values are obtained and imported into EES for data reduction purposes.

CHAPTER 4: DATA ANALYSIS

A data reduction program was developed in Engineering Equation Solver (EES) (Klein, 2015) to determine the air-side heat transfer coefficient, friction factor, and associated uncertainties from the data recorded on the ACC test section as described in Chapter 3. EES utilizes an iterative solution scheme to converge implicitly defined equation sets such as those used in the calculation of the heat transfer and fluid mechanics characteristics of the ACC test section.

4.1 Test Facility Calculations

The following sections describe the analysis of the air-side heat transfer and pressure drop in the ACC test section. Sample calculations for all equations included in the data reduction EES code are included in Appendix A.

4.1.1 Control Volume and Thermal Resistance Network

Evaluation of the air-side heat transfer coefficient in the test section requires the accurate calculation of the heat transferred to the air from the air channels that are bonded to the flat sides of the ACC tubes. The steady-state energy balance on the control volume is presented in Equation (4.1), assuming constant specific heats evaluated at the average fluid temperatures across the control volume and that ambient losses were negligible relative to the test section heat duty magnitude.

$$\dot{m}_{water} \cdot \overline{c}_{p,water} \cdot \left(T_{water,in} - T_{water,out}\right) = -\dot{m}_{air} \cdot \overline{c}_{p,air} \cdot \left(T_{air,in} - T_{air,out}\right) \tag{4.1}$$

The thermal resistance network between the water- and air-side bulk fluid temperatures was analyzed to deduce the air-side heat transfer coefficient. Neglecting radiative heat transfer from the surface of the test section to and from the surroundings, the thermal resistance network for one-dimensional heat transfer from the center of the tube to the air flow is comprised of three thermal resistances located in series. The thermal resistances are due to forced convection of water inside the tube, tube wall conduction, and the forced convection from the tube and the fins to the air flowing through the rectangular fin channels, respectively. Fouling buildup on the water-side of the ACC tube sections is not included in the thermal resistance network. The risk of fouling was minimized by using distilled water and primarily stainless steel components within the test facility. Figure 4.1 illustrates the three thermal resistances located in series between the heated water and air.

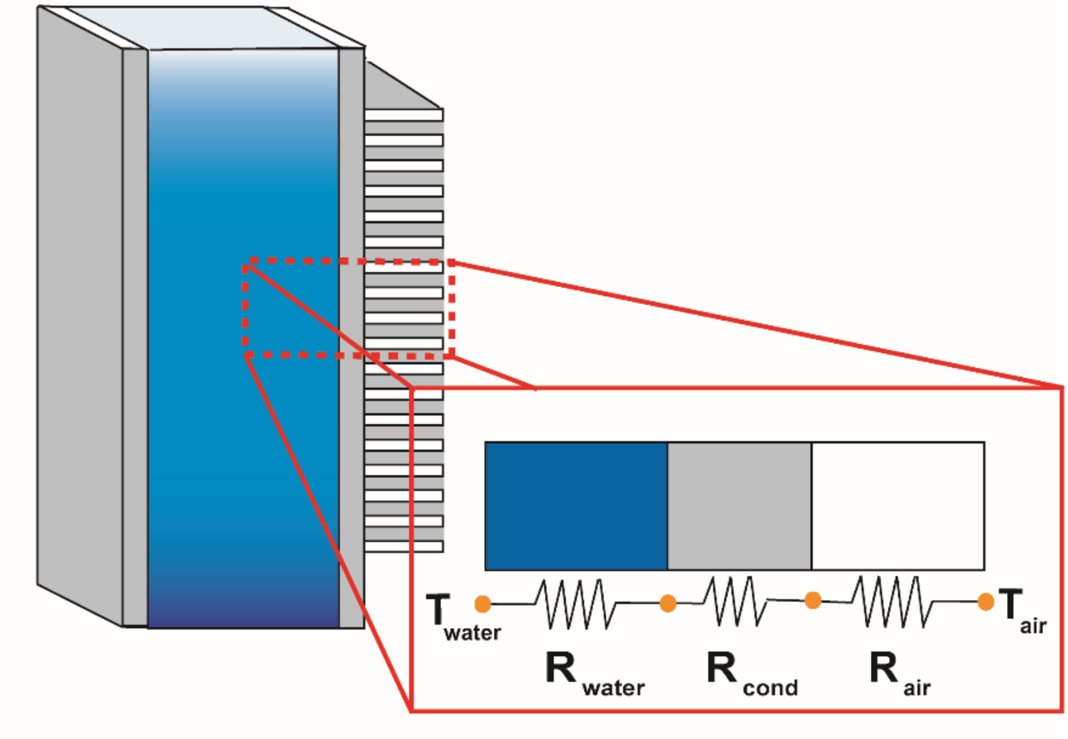

Figure 4.1 Thermal resistance network in finned ACC test section

4.1.2 Water-Side Heat Transfer Calculations

The rib geometry brazed on the inside of the test section forces the water flow through a set of parallel rectangular channels that act as internal fins on the heat transfer surface between the water and air. Equal in cross-sectional area as well as length, the single-phase liquid water evenly distributes amongst the channels assuming a constant channel pressure drop.

It was assumed that the heat transfer from the semi-circular regions on the forward and rear edges of the test section tubes was small relative to the heat transferred through the walls of the air channels. The air-side thermal resistance on the rounded ends is significantly higher than the thermal resistance in the air channels due to the lack of heat transfer surface extensions as well as a lower air velocity and hydraulic diameter in comparison with the rectangular air channels. Assuming uniform water-side flow distribution, the velocities within the semi-circular channels would also be lower due to the increased cross-sectional area relative to the thirty parallel rectangular channels, resulting in lower water-side heat transfer coefficients and a higher effective water-side thermal resistance in the rounded regions of the test section tubes. The increased air- and water-side thermal resistance from the un-finned half-cylinder ends of the ACC tube section would be far greater relative to the thermal resistance from the finned flat walls of the tube section, resulting in primarily one-dimensional heat transfer from the liquid water through the flat walls of the ACC test section tubes. The impact of including the rounded areas in heat transfer coefficient analysis minimal, with rounded areas accounting for less than two percent of the inner and outer heat transfer areas in the condenser. Figure 4.2 includes the air-side, tube-side, and bull-nose areas in a section view of the condenser tube, colored blue, red, and green, respectively.

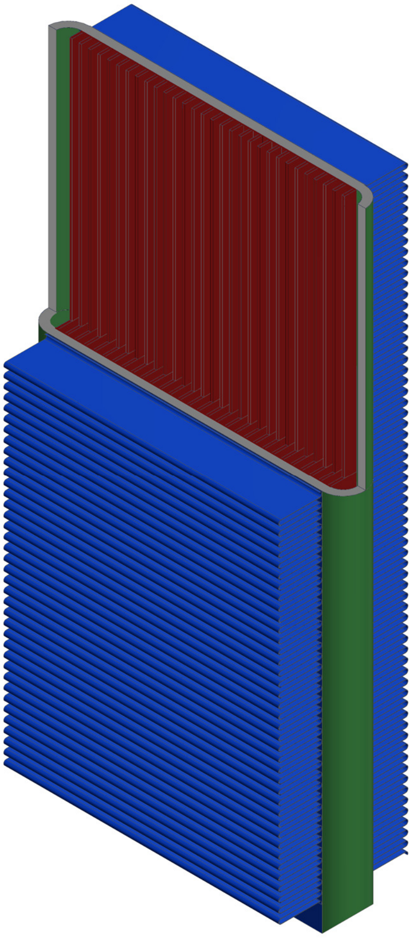

Figure 4.2 Heat transfer areas colored as follows: air-side (blue), tube-side (red), bull-nose area (green)

To determine the water-side heat transfer characteristics, the rectangular channel hydraulic diameter and water-side Reynolds number were calculated using Equations (4.2) – (4.3) based on the rib channel height and width, as well as the thermophysical water properties evaluated at the average water temperature.

$$D_{hy,rib,channel} = \frac{4 \cdot H_{rib} \cdot W_{rib}}{2 \cdot \left(H_{rib} + W_{rib}\right)} \tag{4.2}$$

$$Re_{water} = \frac{\overline{\rho}_{water} \cdot V_{water} \cdot D_{hy,rib,channel}}{\overline{\mu}_{water}} \tag{4.3}$$

The friction factor for internal transitional flow in circular pipes was calculated based on the correlation by Churchill (1977) as a function of the Reynolds number as well as tube roughness and the equivalent circular hydraulic diameter of the flow channel.

$$A=\left(2.457\cdot ln\left(\left(\left(7/Re_{water}\right)^{0.9}+0.27\cdot\varepsilon/D_{hy,rib,channel}\right)^{-1}\right)\right)^{16} \tag{4.4}$$

$$B=\left(\frac{37530}{Re_{water}}\right)^{16} \tag{4.5}$$

$$f_{circ}=8\left(\left(\frac{8}{Re_{water}}\right)^{12}+\left(A+B\right)^{-1.5}\right)^{1/12} \tag{4.6}$$

In Equation (4.6) f_{circ} is the Darcy friction factor for the circular channel based on the hydraulic diameter of the channels formed by the ribs. To correct for the rectangular geometry, the channel aspect ratio α_{rib} was used with the friction factor correction coefficient shown in Equations (4.7) and (4.8) (Bhatti and Shah, 1987).

$$\alpha_{rib,channel}=\frac{W_{rib,channel}}{H_{rib,channel}} \tag{4.7}$$

$$f_{water}=f_{circ}\left(1.0875-0.1125\cdot\alpha_{rib,channel}\right) \tag{4.8}$$

Once the apparent friction factor for rectangular channels, f_{water}, was calculated, the water-side Nusselt number was determined based on the Churchill correlation shown in Equation (4.10) (Churchill, 1977).

$$A=6.3+\frac{0.079\cdot\left(f_{water}/8\right)^{0.5}\cdot Re_{water}\cdot\overline{Pr}_{water}}{\left(1+\overline{Pr}_{water}^{\ 0.8}\right)^{5/6}} \tag{4.9}$$

$$Nu_{water} = \left(4.364^{10} + \left(\frac{exp\left(\frac{2200 - Re_{water}}{365}\right)}{4.364^{2}} + \left(A\right)^{-2} \right)^{-5} \right)^{1/10} \tag{4.10}$$

The water-side heat transfer coefficient through the rectangular ducts, a function of the Nusselt number, rib channel hydraulic diameter, and water thermal conductivity evaluated at the average temperature and pressure of the water within the test section was calculated using Equation (4.11).

$$h_{water} = \frac{Nu_{water} \cdot \bar{k}_{water}}{D_{hy,rib,channel}} \tag{4.11}$$

The internal rib structure acts as an array of fins on the water-side of the test section, increasing the effective area for heat transfer from the water. Given the symmetry in the test section internal rib array, the fin coefficient for the internal ribs on the flat surface of the tubes was calculated assuming the rib was an adiabatically tipped fin with a height equal to half of the rib height, as shown in Equations (4.12) and (4.13).

$$m^{*}_{rib} = \sqrt{\frac{h_{water} \cdot Per_{rib} \cdot \left(H_{rib}/2\right)^{2}}{k_{rib} \cdot A_{cs,rib}}} \tag{4.12}$$

$$\eta_{rib} = \frac{tanh\left(m^{*}_{rib}\right)}{m^{*}_{rib}} \tag{4.13}$$

With the fin efficiency calculated, the thermal resistance for the water-side convection was determined as a function of the exposed base area inside the tube, the rib wall area, the fin efficiency of the ribs, and the water-side heat transfer coefficient, as shown in Equation (4.14).

$$R_{water} = \frac{1}{h_{water} \cdot \left(A_{tube,int,bare} + \eta_{rib} \cdot A_{rib,wall} \right)} \tag{4.14}$$

4.1.3 Tube Conduction Thermal Resistance

In calculating the one-dimensional tube conduction thermal resistance, it was again assumed that negligible heat transfer would occur from the rounded ends of the flat tubes. The ratio of rounded wall area to perpendicular heat transfer area is very low, particularly when the internal ribs and external fins effective areas are included. The rounded area accounts for only two percent of the inner area, and less than one percent of the outer finned heat transfer area. The conduction heat transfer area was defined using Equation (4.15) as the flat wall area of the test section tubes.

$$A_{cond,tube} = 2 \cdot \left(W_{ACC,tube} - H_{ACC,tube} \right) \cdot L_{ACC,tube} \tag{4.15}$$

The thermal resistance for one-dimensional conduction through a flat plate was used to model conduction resistance of the tube as shown in Equation (4.16) as a function of the tube thickness, flat plate heat transfer area, and thermal conductivity of the stainless steel test section tubes.

$$R_{cond} = \frac{t_{ACC,tube}}{\left(k_{tube} \cdot A_{cond,tube} \right)} \tag{4.16}$$

The relative magnitude of both the water-side convection resistance and the tube conduction resistance was minimal compared to the resistance from air-side convection, with air-side convection resistance accounting for over eighty percent of the overall thermal resistance. The water-side thermal resistance accounts for less than 10% of the overall thermal resistance.

4.1.4 Test Section Heat Duty Calculation

The heat duty of the ACC test section was calculated using the water-side temperature measurements to experimentally determine the total thermal resistance. All fluid properties in the heat transfer analysis were evaluated at the average temperature axially along the length of the test section. Water properties do not vary significantly at the temperatures and pressures experienced in the ACC test section. Inlet and exit temperatures for the test section heat duty analysis were evaluated at the top of the first and fourth tube in the test section to ensure that the fluid had adequately mixed, providing an accurate bulk fluid temperature measurement. This also ensured that the heat transferred across the boundary in between adjacent tubes, while relatively minimal, was captured in the heat duty calculation. The use of the RTD measurements at the inlet and exit of the test section was validated through the analysis of the energy balance across the test section. The heat transfer from the test section was calculated as a function of the water mass flow rate, specific heat, and differential test section temperature as measured by the RTD sensors as described in Equation (4.17).

$$\dot{Q}_{tube} = \dot{m}_{water} \cdot \overline{c}_{water} \cdot \left(T_{water,in} - T_{water,out}\right) \tag{4.17}$$

Calculating the air-side heat transfer coefficient of the finned ACC tubes requires knowledge of the overall heat transfer thermal resistance. The effectiveness-NTU method was utilized calculate the total thermal resistance from the heat duty measured in the test section. The air mass flow rate was assumed constant across the face of the test section with the mass flow rate across each of the two test section tubes equal to half of the total flow rate. The flow arrangement was considered cross-flow with both fluid streams unmixed, and minimum/maximum heat capacity rates were calculated as shown in

Equations (4.18) – (4.19) and the corresponding heat capacity rate ratio as shown in Equation (4.20).

$$\dot{C}_{min} = \overline{c}_{air} \cdot \dot{m}_{air} \tag{4.18}$$

$$\dot{C}_{max} = \overline{c}_{water} \cdot \dot{m}_{water} \tag{4.19}$$

$$C_r = \frac{\dot{C}_{min}}{\dot{C}_{max}} \tag{4.20}$$

The heat exchanger tube section effectiveness, defined in Equation (4.21), is a function of the minimum heat capacity rate, the maximum driving temperature difference between fluids (difference between the hot stream inlet and cold stream inlet), and the total heat load rejected from the tube as measured by the facility instrumentation. The inlet air temperature was calculated by taking the arithmetic mean of the six air-side temperature measurements at the inlet of the test section.

$$\varepsilon_{tube} = \frac{\dot{Q}_{water}}{\dot{C}_{min} \cdot \left(T_{water,in} - T_{air,in}\right)} \tag{4.21}$$

Once the test section heat transfer effectiveness was calculated, the effectiveness-NTU relationship was implicitly solved to obtain the number of transfer units. Equation (4.22) describes the effectiveness of a heat exchanger in a cross-flow arrangement with both fluid streams unmixed as a function of the number of transfer units and the heat capacity rate ratio, C_r.

$$\varepsilon_{tube} = 1 - exp\left(\left(1 / C_r\right) \cdot \left(NTU^{0.22}\right) \cdot \left(exp\left(-C_r \cdot \left(NTU^{0.78}\right)\right) - 1\right)\right) \tag{4.22}$$

With the number of transfer units obtained from the above equation, the overall heat transfer coefficient of the ACC tube, $\boldsymbol{UA}$, is calculated. The number of transfer units is related to the overall system thermal conductance, or the inverse of thermal resistance, using Equation (4.23).

$$UA = \dot{C}_{\min} \cdot NTU = \frac{1}{R_{total}} \tag{4.23}$$

4.1.5 Air-Side Heat Transfer Calculations

The total test section thermal resistance calculated using Equation (4.23) is composed of the individual thermal resistances due to the internal water convection, tube conduction, and the external convection through the air channels as shown in Equation (4.24).

$$R_{total} = R_{water} + R_{cond} + R_{air} \tag{4.24}$$

The fins were bonded to the surface of the tubes with a thermal adhesive, which introduces an added thermal resistance in between the surface of the tube and the fin wall. The thermal resistance network for heat transfer from the surface of the tube to the air flow consists of two parallel heat transfer paths as demonstrated in Figure 4.3.

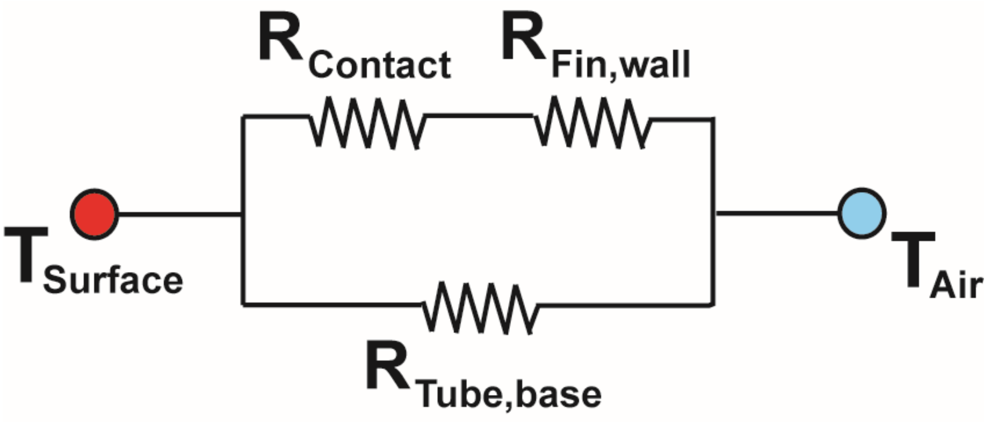

Figure 4.3 Parallel thermal resistance circuit for fins with contact resistance (R_{air} in Figure 4.1)

The fin efficiency, η_{fin}, was calculated using Equations (4.25) and (4.26) assuming an adiabatic fin tip boundary condition.

$$m_{fin}^{*} = \sqrt{\frac{h_{air} \cdot Per_{fin} \cdot \left(H_{fin}\right)^{2}}{k_{fin} \cdot A_{cs,fin}}} \tag{4.25}$$

$$\eta_{fin} = \frac{tanh\left(m_{fin}^{*}\right)}{m_{fin}^{*}} \tag{4.26}$$

Based on the above thermal resistance and fin efficiency formulation, the overall surface efficiency was described using Equations (4.27) and (4.28), where $R^{"}$ is the contact resistance of the thermal adhesive as determined from the material data sheet supplied with the product from the manufacturer.

$$C_{1} = 1 + \eta_{fin} h_{air} \left[\frac{A_{fin} R^{"}}{A_{c,fin}}\right] \tag{4.27}$$

$$\eta_{o,c} = 1 - \frac{A_{fin}}{A_{fin} + A_{bare}}\left[1 - \frac{\eta_{fin}}{C_{1}}\right] \tag{4.28}$$

With the overall surface efficiency calculated, the air-side heat transfer coefficient was calculated using Equation (4.29).

$$h_{air} = \frac{1}{R_{air} \cdot \left[\eta_{o,c}\left(A_{bare} + A_{fin}\right)\right]} \tag{4.29}$$

4.1.6 Air-Side Friction Factor Calculation

Air-side pressure drop measurements were obtained using low-span air-side differential pressure transducers. While the outer geometry of the test section closely matches a power plant ACC, the minor losses across the test section are different from those experienced at an operating power plant. The test section was oriented directly perpendicular to the air flow, whereas an industry ACC has vertically inclined tubes with an apex angle of approximately 60°. Accurate characterization of the minor losses across the test section ensures that only the channel losses are used in calculating an effective fin channel friction factor for comparison between tests with and without the installed AFR assemblies. Figure 4.4 illustrates the air-side pressure profile along the length of the test section.

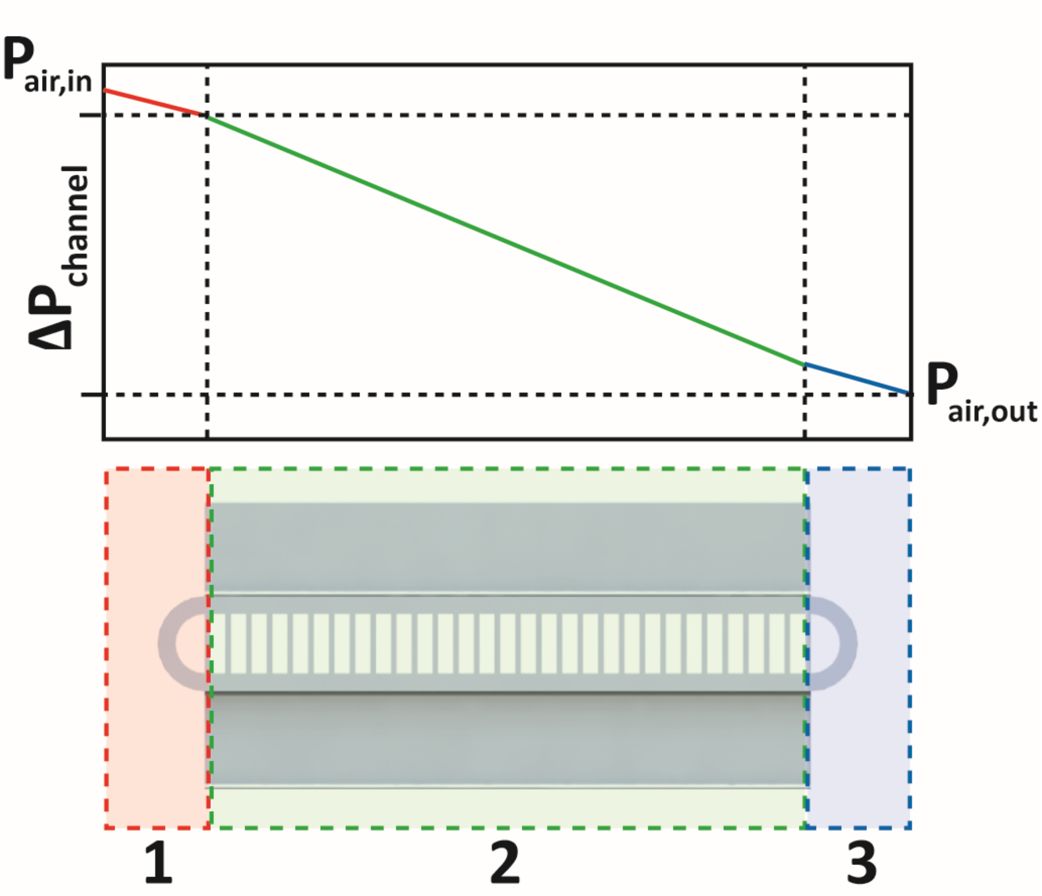

Figure 4.4 Top-down view of ACC tube section illustrating air pressure through the fin channels

The minor losses described above were calculated based on the approach presented by Ghiaasiaan (2007). The inlet contraction losses (corresponding to the losses in the red region of Figure 4.4) were calculated based on the contraction ratio between the air channel area and total frontal area ($\boldsymbol{A_{ff}}$ and $\boldsymbol{A_{fr}}$, respectively). These losses were a result of the irreversibility encountered by the air entering the fin channels. The geometry contraction ratio, σ , was calculated as a function of the total frontal area and the free flow area through the core of the test section as demonstrated in Equation (4.30).

$$\sigma = A_{ff} \,/\, A_{fr} \tag{4.30}$$

The inlet contraction coefficient was calculated based on the expression in Equation (4.31) as a function of the contraction ratio.

$$C_C = 1 - \frac{1-\sigma}{2.08(1-\sigma)+0.5371} \tag{4.31}$$

After calculation of the contraction coefficient, the inlet contraction loss coefficient was calculated as follows in Equation (4.32).

$$K_{con} = \left(\frac{1}{C_C} - 1\right)^2 \tag{4.32}$$

The hydrodynamic losses resulting from the air flow exiting the ACC test section were due to the sudden expansion from the fin channels into the larger flow area as well as the redistribution of the velocity profiles. The outlet loss coefficient of the flow past the back of the ACC test section, K_{eo}, due to the viscous losses in the blue region of Figure 4.4, was calculated using the loss coefficient resulting from a sudden expansion in the flow field, and is a function of the ratio between the minimum and maximum flow areas, as shown in Equation (4.33).

$$K_{eo} = (1-\sigma)^2 \tag{4.33}$$

With the inlet and outlet loss coefficients calculated, the total pressure drop associated with the losses in the inlet and outlet regions was calculated based on the respective air densities and flow velocities entering and leaving the test section, as shown in Equations (4.34) and (4.35).

$$\Delta P_{inlet} = K_{con} \cdot \frac{1}{2} \cdot \rho_{in} \cdot V_{air,in}{}^{2} \tag{4.34}$$

$$\Delta P_{outlet} = K_{eo} \cdot \frac{1}{2} \cdot \rho_{out} \cdot V_{air,out}{}^{2} \tag{4.35}$$

In addition to the contraction and expansion losses through the test section, the fluid core accelerates as it is heated through the length of the test section air channels due to the decrease in bulk density and corresponding expansion of the fluid. The losses associated with the fluid acceleration through the test section are shown in Equation (4.36).

$$\Delta P_{acceleration} = \frac{G_{channel}}{\rho_{air,in}} \left[\frac{\rho_{air,in}}{\rho_{air,out}} - 1 \right] \tag{4.36}$$

With the minor pressure losses through the tests section characterized by the previous sets of equations, the channel-only pressure drop was deduced from the pressure drop across the ACC section as measured by the low-span Dwyer differential pressure transducer by subtracting the minor losses from the total measured pressure drop, as shown in Equation (4.37).

$$\Delta P_{channel} = \Delta P_{measured} - \Delta \mathrm{P}_{\mathrm{inlet}} - \Delta \mathrm{P}_{\mathrm{outlet}} - \Delta \mathrm{P}_{\mathrm{acceleration}} \tag{4.37}$$

Once the corrected pressure drop through the test section fin channel was calculated, the Darcy friction factor associated with the rectangular air channels was determined as shown in Equation (4.38), where the channel velocity is calculated by dividing the volumetric flow rate through the test section by the free-flow cross-sectional flow area through the test section air channels.

$$f_{air} = \frac{2\Delta P_{channel}}{\bar{\rho}_{air} \cdot \left[\frac{L_{fin,channel}}{D_{hy,fin,channel}}\right] \cdot V_{channel}{}^{2}} \tag{4.38}$$

4.2 Predicted Baseline ACC Air-Side Performance

The analytical solution for the heat transfer coefficient in an isothermal rectangular duct was considered for comparison with the data from the present study. The air-side fin channels through which the air flows were assumed to be rectangular ducts with a height of 25.4 mm and a width of 2.54 mm. The resulting height-to-width aspect ratio is 0.1, with a fin pitch of approximately 35.4 fins per m (nine fins per inch). Individual fin channels were assumed to be isolated from adjacent channels such that there was minimal fluid cross-communication from adjacent channels as demonstrated in Figure 4.5, ensuring the applicability of rectangular channel correlations. Note that the curvature at the crown and base of the fins is exaggerated for illustrative purposes.

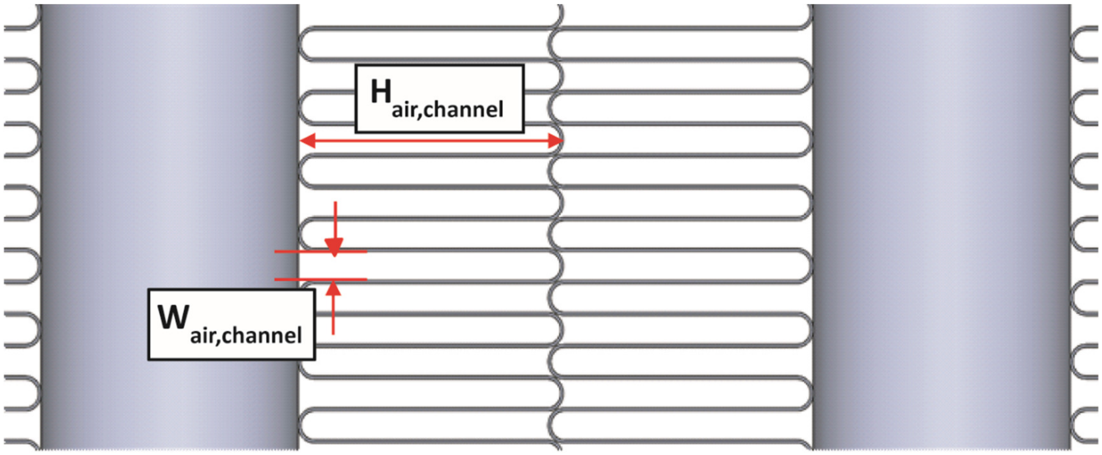

Figure 4.5 Idealized separation of adjacent air channels

Shah and Bhatti (1987) proposed the following polynomial curve fits for the fully-developed Nusselt number and friction factor of convective, internal, and laminar flows through rectangular ducts, where α is the duct aspect ratio and Re_{air} is the channel

Reynolds number calculated with the hydraulic diameter and mean flow velocity through the core of the test section. The aspect ratio α was calculated by dividing the width of fin channel by the height of fin channel as shown in Equation (4.39).

$$\alpha = \frac{W_{air,channel}}{H_{air,channel}} \tag{4.39}$$

$$Nu_{air,SB} = 7.541 \cdot \left(1 - 2.6100 \cdot \alpha + 4.9700 \cdot \alpha^2 - 5.1190 \cdot \alpha^3 + 2.7020 \cdot \alpha^4 - 0.5480 \cdot \alpha^5\right) \tag{4.40}$$

$$f_{air,SB} = \frac{96}{Re_{air}} \cdot \left(1 - 1.3553 \cdot \alpha + 1.9467 \cdot \alpha^2 - 1.7012 \cdot \alpha^3 + 0.9564 \cdot \alpha^4 - 0.2537 \cdot \alpha^5\right) \tag{4.41}$$

These curve-fit relationships are valid for fully-developed laminar flow through square-cornered rectangular ducts with isothermal wall boundary conditions. The Reynolds number range in this investigation was in the range of 600 – 1700, which is considered to be within the laminar flow regime range. While a temperature variation along the length of the fins in the ACC test section exists due to the finite conduction thermal resistance along the fin length, the high thermal conductivity of the aluminum fins results in a fin efficiency of over 80% and the corresponding axial temperature variation along the length of the fin is minor relative to the temperature gradient into the air flow.

In addition to the fully-developed correlation for rectangular duct heat transfer with isothermal walls, the correlations for developing flow within a rectangular duct using the correlations presented by Shah and London (1978) were also evaluated. The correlations for isothermal and constant heat flux boundaries conditions were both considered. These formulations for boundary conditions provide the theoretical bounds for heat transfer coefficient in developing flows through rectangular ducts. In addition to the heat transfer coefficient correlations, the friction factor for developing flow was also evaluated for comparison with the pressure drop results from the test facility.

4.3 ACC Design Code

The ACC design code developed by Lin *et al.* (2016) on the EES platform was modified to accept the input of curve-fit relationships for the heat transfer and pressure drop data collected in the ACC wind tunnel test facility. The design code utilized segmented heat exchanger analysis to calculate standalone ACC module performance in terms of required fan power and steam condensation temperature, as well as the corresponding Rankine cycle efficiency.

Accurate characterization of the steam-side heat transfer and pressure drop characteristics of the ACC condensation tubes is critical to properly calculating the overall cycle efficiency improvements realized through the installation of AFRs. The steam-side heat transfer coefficient in the computational model was calculated using the correlation from Akhavan and Behabadi developed based on data from R-134a condensation in inclined tubes (Akhavan-Behabadi *et al.*, 2007). This correlation represented the average magnitude for condensing heat transfer coefficient evaluated by Mahvi *et al.* (2016), with predictions ranging from approximately 1000 – 4000 W m^{-2} K^{-1} along the length of the condensation tube. To calculate the two-phase Martinelli parameter, the correlation from Jung *et al.* (2003) was used. To calculate the steam-side two-phase pressure drop, the Blasius correlation was used to calculate the single-phase vapor friction factor and the correlation by Lockhart and Martinelli was used to calculate the void fraction (Lockhart and Martinelli, 1949). Trapezoidal integration was employed to calculate the pressure drop across each segment, with the two-phase pressure drop multiplier applied to the single-phase vapor friction factor calculated with the Chisholm correlation (Chisholm, 1967). The segmented condenser model was then iteratively solved within the EES computing environment, at which point the initial temperature difference and air-side pressure drop of the associated standalone ACC module were determined.

The condenser air-side heat transfer coefficient was evaluated based on the results of the ACC test facility curve-fit results. Air-side minor pressure losses through the condenser module constitute a significant portion of the required fan power per ACC cell. The air-side minor losses associated with the ACC cell were calculated based on the approach by Kröger (1998). These minor losses, in conjunction with the channel pressure drop measured in the wind tunnel test facility, were used to calculate the required fan power for steam condensation. Air-side losses upstream and downstream of the fan due to walkways and other obstructions, angled inlet and exit losses into the ACC air channels, jetting losses due to recombination of the flow in between adjacent ACC modules, and outlet losses due to the velocity profile non-uniformity at the exit of the modules were included in the module minor loss evaluation.

The computational results for the standalone air-cooled condenser module were then coupled with a Rankine cycle thermodynamic model to evaluate the plant-level efficiency as a function of the standalone condenser performance. Given the condenser module inlet steam saturation pressure, the turbine pressure ratio was known. The cycle was designed for a net power output of 500 MW after the pump and fan parasitic power losses were subtracted from the total power output from the turbine model.

CHAPTER 5: RESULTS AND DISCUSSION

The results from the heat transfer and pressure drop experiments as well as analyses of the power plant efficiency using those results are discussed in this chapter. A brief discussion of the measurement uncertainty analysis is also provided. A comparison between the baseline and reed-enhanced condenser results is presented. The heat transfer and pressure drop results are incorporated into the plant-level segmented condenser model to predict condenser performance as well as the effect of condenser enhancements on overall plant efficiency and performance.

5.1 Energy Balance

Energy balances between the heat transferred from the heated water and that received by the air stream were first conducted to establish the validity of the results from the experiments. The water-side heat transfer rate was calculated as a function of the water-side flow rate, temperature difference from inlet to exit of the test section, and the specific heat of the water evaluated at the average temperature and pressure in the test section. The air-side heat transfer rate was calculated with the air-side flow rate measured by the nozzle flow meter, average air-side temperature difference across the test section measured by the thermocouple arrays, and the average air specific heat. Figure 5.1 shows a comparison of the air-side and water-side heat transfer rates for the baseline and reed-enhanced experiments. The air and tube-side heat transfer rates were approximately equal throughout the test range, with all data points within ± 5.25%. The average deviation for the energy balance was 0.0409 kW and 0.148 kW for baseline and reed-enhanced cases, respectively, where the total test section heat duty ranged from 6.0 – 9.5 kW depending on the air-side heat capacity rate. The absolute average deviation (AAD) for baseline and reed-enhanced condensers was 0.0963 kW and 0.187 kW, respectively. Both average deviations for the data sets were within the relative measurement uncertainties. The air-side heat transfer rate was generally lower than the water-side heat transfer rate at the lower heat duties corresponding to lower air-side mass flow rates. The heat losses to the ambient space within the wind tunnel are higher relative to the measured heat transfer rate at lower heat duties, which could explain the lower measured air-side heat duties at lower Reynolds number flows. Sample calculations for heat losses from the test section for a representative data point are included in Appendix C. At the lowest Reynolds number test, the heat loss is estimated to be approximately 28 W, which decreases to approximately 17 W at the upper range of evaluated Reynolds numbers. Measurement uncertainties and the effect of air-side maldistribution are more likely to affect the air-side heat duty measurement and may explain the variance in air and tube-side heat duty measurements. Based on the energy balance analysis, the tube-side heat duty data were determined to be accurate, and were used to evaluate the heat transfer rate for each data point (if it was within the energy balance bounds described above) and the corresponding heat transfer coefficient.

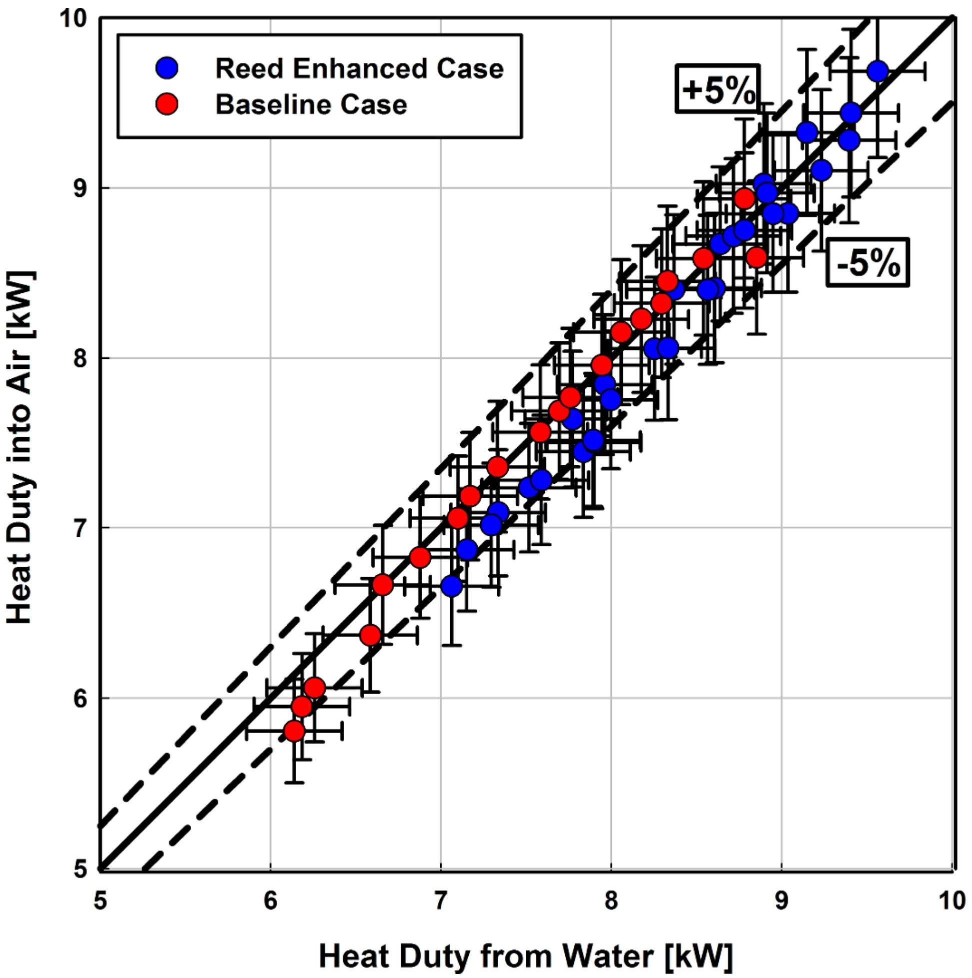

Figure 5.1 Energy balance for baseline and reed enhanced data points

5.1.1 Test Section Energy Balance Uncertainty Analysis

Uncertainty analyses were conducted using the built-in features to perform these calculations in EES. The measurement uncertainties for test facility instruments were set to the experimental uncertainties described in Chapter 3. For tube-side heat transfer rate as well as the air channel heat transfer coefficient, the experimental uncertainties in temperature measurement were the dominant factors in determining the overall uncertainty. The uncertainties provided do not take in to account the random uncertainties associated with the measurements. Random uncertainty was largely mitigated by averaging the data for any point over __ scans over a period of __ seconds, and by repeating data points sporadically during testing to ensure low variation in the results. Table 5.1 illustrates results from uncertainty analysis on a representative water-side heat duty data point.

Table 5.1 Representative uncertainty for water-side heat duty

$\dot{Q}_{RTD}$ = 6.14 [kW] ± 0.2801	
Partial Derivative	Percent of Total Uncertainty (%)
$\frac{\partial \dot{Q}_{water}}{\partial P_{water,in}} = -2.017 \times 10^{-7}$	0.00
$\frac{\partial \dot{Q}_{water}}{\partial P_{water,out}} = -2.017 \times 10^{-7}$	0.00
$\frac{\partial \dot{Q}_{water}}{\partial T_{water,in}} = 1.648$	49.82
$\frac{\partial \dot{Q}_{water}}{\partial T_{water,in}} = -1.65$	49.99
$\frac{\partial \dot{Q}_{water}}{\partial \dot{m}_{water}} = 0.2491$	0.19

5.2 ACC Test Section Heat Transfer Results

The heat transfer characteristics for baseline and reed-enhanced test sections were calculated using the data reduction program developed based on the analysis described in Chapter 4. The following sections detail the Nusselt numbers for baseline and reed-enhanced condensers.

5.2.1 Air-Side Nusselt Number Results

For validation of the baseline Nusselt number measurements in the wind tunnel test facility, the results were compared with three internal flow correlations based on the following boundary conditions: developing/constant heat flux boundary conditions, developing/constant temperature boundary conditions, and fully-developed/constant temperature boundary conditions. Developing flow correlations were calculated using correlations for flow through rectangular ducts presented by Shah and London (1978). The high fin efficiency of the test section air channels results in nearly isothermal walls and as such the fully-developed, constant temperature rectangular duct heat transfer coefficient presented by Shah and Bhatti (1987) is also considered in comparison with the baseline data for validation. The results for the heat transfer coefficients and Nusselt numbers measured in the baseline and reed-enhanced test section, as well as the predicted values from the three correlations described above, are included in Figure 5.2 and Figure 5.3, respectively.

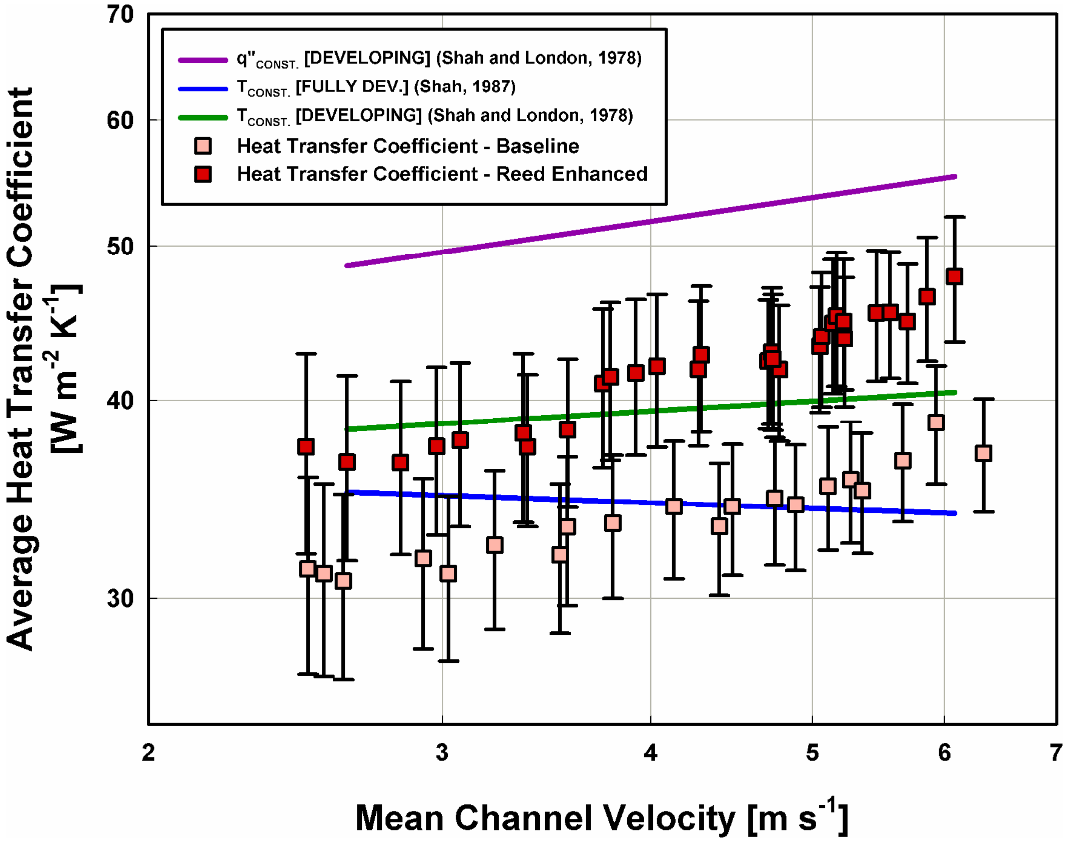

Figure 5.2 Heat transfer coefficient vs. mean channel velocity

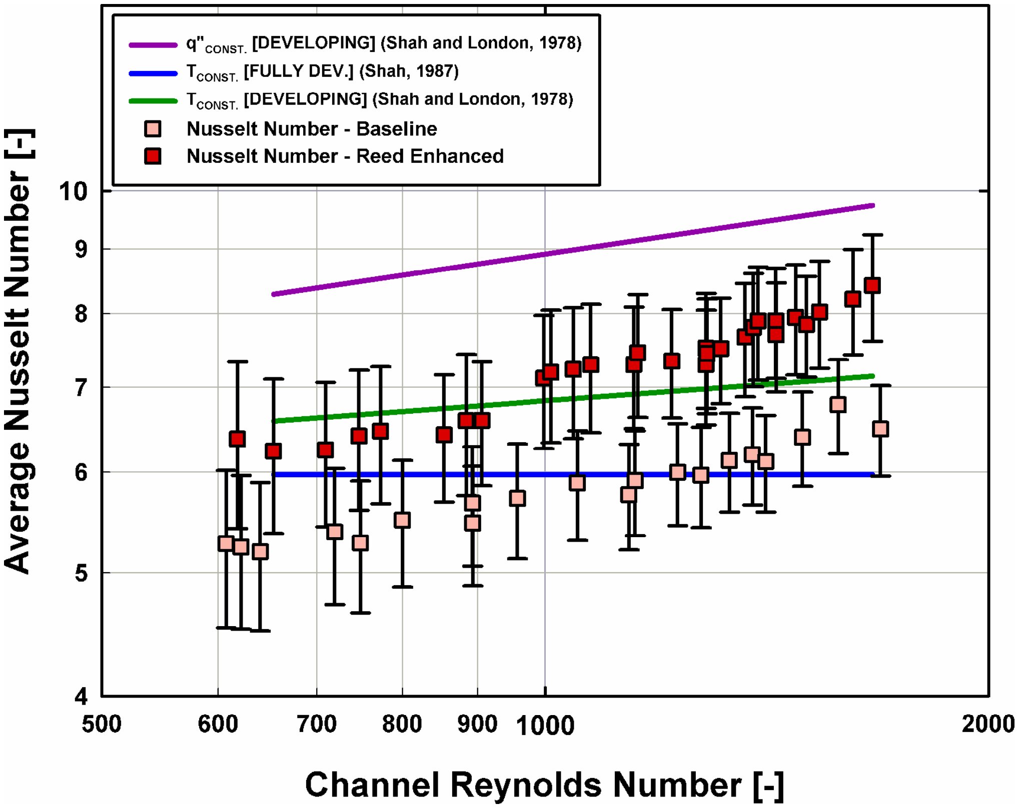

Figure 5.3 Nusselt number vs. Reynolds number

The baseline heat transfer coefficients were lower than the values predicted by the three correlations up until a Reynolds number of approximately 1100. Besides measurement uncertainty, which is higher at lower heat transfer rates, there are several reasons for the lower heat transfer coefficients at low Reynolds numbers, as described below.

The entrance effects resulting from the flow entering the channels after passing over the bullnose portion of the test section are not accounted for in the correlations presented previously. As the flow enters the air channels after flowing over the bullnose portion on the leading edge of the test section, potential separation of the flow and a disruption of the initial developing region could hasten full development, leading to lower heat transfer coefficients.

The thermal adhesive connecting the fins to the test section tubes (MasterBond Supreme 18TC) was assumed to have contact resistances as low as $5 - 7 \times 10^{-6}$ K m^2 W^{-1} under ideal bonding conditions, as described by the material properties data sheet supplied with the product by the manufacturer. Improper surface preparation or bonding procedures could have decreased the effectiveness of the bond, thus increasing the thermal resistance. The presence of air bubbles or increased adhesive thickness would have reduce the effective surface efficiency, resulting in a lower effective air-side surface area. A two-fold increase in the contact resistance used for data reduction from 6×10^{-6} K m^2 W^{-1} to 12×10^{-6} K m^2 W^{-1} would have resulted in a four percent increase in predicted air-side heat transfer coefficient. Additionally, an adhesive film covered the base tube area due to the squeezing of the adhesive resulting from the fins being pressed against the surface during installation and curing which would have increased the base area thermal resistance. This base contact resistance was not included in the heat transfer calculations for air-side surface area as the tube base area accounts for only a small portion of the total air-side area through which heat could be rejected to the air. The decrease in thermal resistance resulting from ideal bonding of the fins would decrease the convective thermal resistance and similarly increase the air-side heat transfer coefficients. Figure 5.4 illustrates the variation in Nusselt number with contact resistance values ranging from $6 - 18 \times 10^{-6}$ K m^2 W^{-1}.

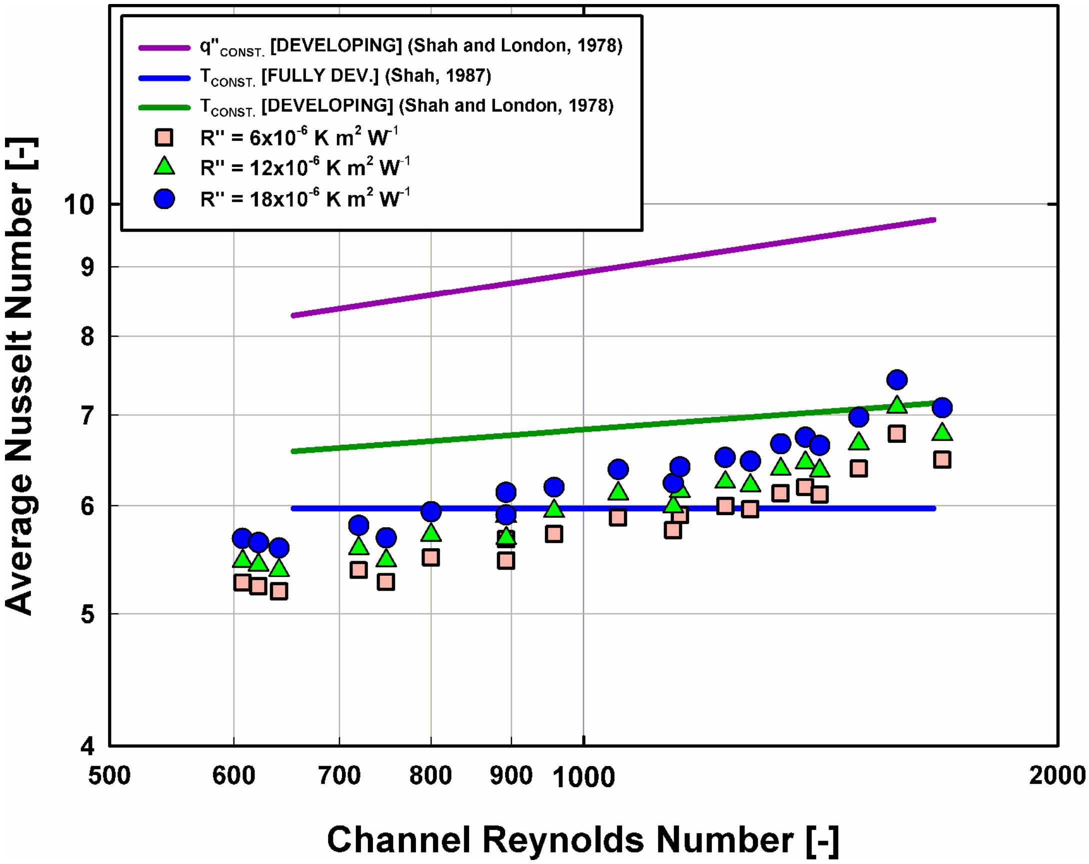

Figure 5.4 Effect of contact resistance variation on Nusselt number

Air-side maldistribution may also have played a role in decreasing the measured air-side heat transfer coefficients. Maldistribution was minimized by adding flow straighteners and lengths of duct work without bends preceding the test section, but could not be entirely avoided due to potential buoyancy effects and obstructions upstream of the flow straightening devices. While measurements of local flow velocities in the wind tunnel demonstrated low relative variation, installation of the test section could have caused local flow nonuniformities to develop across the frontal area. If several channels had lower flow rates than average, it would have resulted in lower local heat transfer coefficients and increased air-side thermal resistance along certain portions of the test section tubes, with slightly higher heat transfer coefficients in regions of higher channel velocity. The Nusselt number for developing flows in rectangular ducts increases more rapidly at lower Reynolds numbers, and as such the relative decrease in lower velocity channels would be greater than the increase in higher velocity channels. As localized measurement of heat transfer coefficient is not possible with the test section fabricated for this investigation, the effect of the maldistribution would be included in the bulk heat transfer coefficient measurement and could have resulted in a decrease in the measured Nusselt number. Previous investigations into air-flow maldistribution in cross-flow heat exchangers have shown significant decreases in heat transfer effectiveness resulting from flow non-uniformities across the face of a cross-flow heat exchanger (Bury, 2012).

The baseline Nusselt number increased throughout the range of Reynolds numbers tested. This monotonical increase is likely a result of developing flow patterns within the air channels. For internal flows of air, the thermal entrance length is approximately equal to the hydrodynamic entrance length. As such, the thermal entrance length for laminar flow in a duct can be approximated as shown in Equation (5.1) (Shah and London, 1978).

$$L_D = D_{hy,channel}\left(0.011\mathrm{Re}_{channel} + \frac{0.315}{1+0.0175\mathrm{Re}_{channel}}\right) \tag{5.1}$$

The calculated thermal development length for Reynolds numbers ranging from 650 to 2000 ranges from approximately 35 – 95 mm. Based on these approximations, thermal development in the air flow occurred in at least 20% of the channel at the lowest Reynolds numbers in the test range and increased to approximately 60% of the channel length at the highest Reynolds numbers, potentially explaining the increasing Nusselt number with Reynolds number. Additionally, the slope of the Nusselt number versus Reynolds number graph is somewhat smaller at lower Reynolds numbers, which can be explained based on the shorter development lengths resulting in longer fully developed portions of the flow with lower heat transfer coefficients. As only an average heat transfer coefficient was deduced from the measured data, these variations in Nusselt number along the air flow direction could not be measured and confirmed.

The AFR enhanced condenser demonstrated an increase in heat transfer coefficient across the range of Reynolds numbers, with a slight step-increase in Nusselt number enhancement at a Reynolds number between 900 and 1000. The increase in Nusselt number is probably caused by an increased number of reeds beginning to flutter around this Reynolds number, a phenomenon that was visually observed in the test facility using a light located upstream of the test section. At lower air-side flow rates, the onset of reed flutter was inhibited by the static forces holding the reed against the air channel walls, resulting in partial channel blockage and a relatively lower measured heat transfer coefficient. The Nusselt number for the reed-enhanced test section data was greater than the baseline Nusselt numbers throughout the range of tested air-side flow rates. The relative increase in Nusselt number is between 17 – 27%, with enhancement factors outside the measurement uncertainty demonstrated above a Reynolds number of approximately 1200. While Nusselt number enhancement was also demonstrated at lower Reynolds numbers, the measurement uncertainty ranges overlapped due to the higher uncertainty at the lower heat duties investigated corresponding to low Reynolds number flows.

5.2.2 Nusselt Number Expressions

The Nusselt number data from the ACC test facility were curve-fit in MATLAB for implementation into the ACC Rankine cycle analysis program. The simplest form for Nusselt number vs. Reynolds number curve-fit relationships is shown in Equation (5.2) and the results of the regression analysis performed on the data are shown in Table 5.2.

$$Nu(\mathrm{Re}) = A \cdot \mathrm{Re}^{B} \tag{5.2}$$

Table 5.2 Baseline and reed-enhanced Nusselt number curve-fit coefficients

Test Case	*A*	*B*	R^2
Baseline	1.161	0.232	0.93
Reed	0.852	0.305	0.95

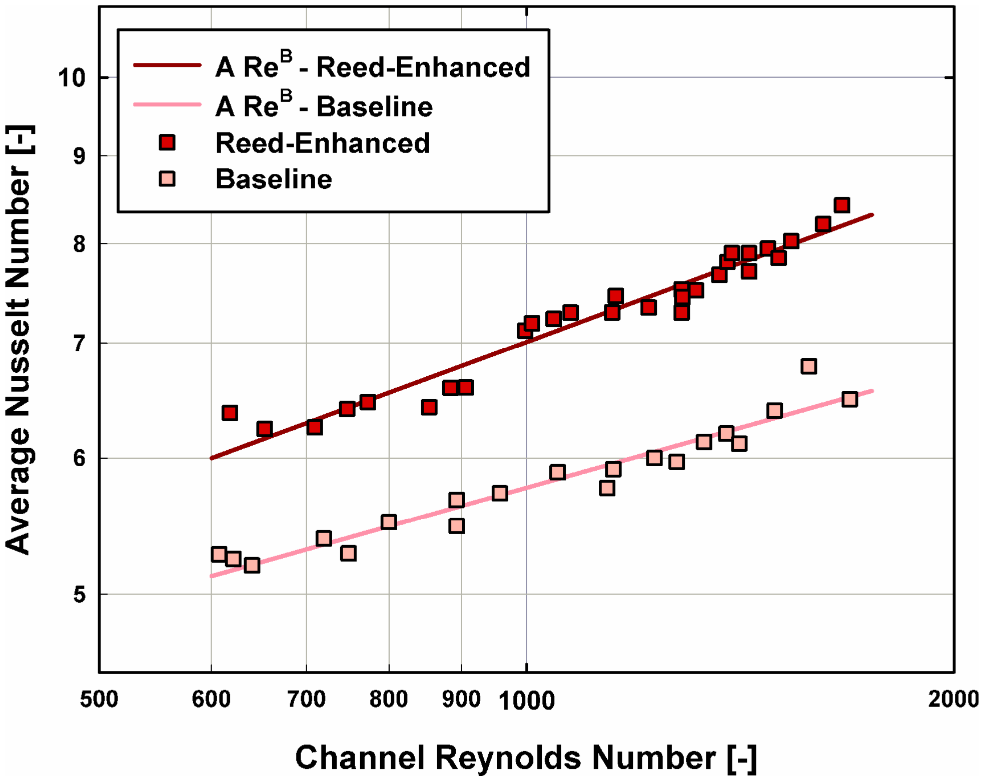

Figure 5.5 Curve-fit Nusselt number results

The average deviation, absolute average deviation, and standard deviation for baseline and reed-enhanced Nusselt number curve-fit equations are shown in Table 5.3.

Table 5.3 Curve-fit figures of merit for Nusselt number

Test Case	*AD*	*AAD*	*SD*
Baseline	-1.12×10^{-3}	8.55×10^{-2}	1.18×10^{-1}
Reed	1.20×10^{-3}	1.17×10^{-1}	1.41×10^{-1}

5.3 Air-Side Pressure Drop Results

The pressure drop and friction factor characteristics of the ACC test section before and after AFR installation are described below.

5.3.1 Friction Factor

The air-side minor losses in the test section were calculated based on the analysis described in Chapter 4. The removal of minor losses from the measured pressure drop is important to characterizing the air-side friction factor. The air-side minor losses due to the inlet contraction, outlet expansion, and fluid acceleration were of significantly lower magnitude than the measured channel losses, and as such, their evaluation was not a significant source of uncertainty in the test section. Inlet contraction losses for the lowest (Re = 607) and highest (Re = 1689) Reynolds numbers considered account for 2.4% and 5.4% of the total measured pressure losses, respectively. Likewise, outlet expansion losses account for only 2.8% and 5.7% of the measured losses, respectively. A standard uncertainty of ±25% was applied to the calculated minor losses but did not significantly impact the overall uncertainty of the pressure drop or friction factor measurements. The minor losses are shown in Figure 5.6 for the lowest and highest air-side Reynolds numbers for the baseline ACC test section.

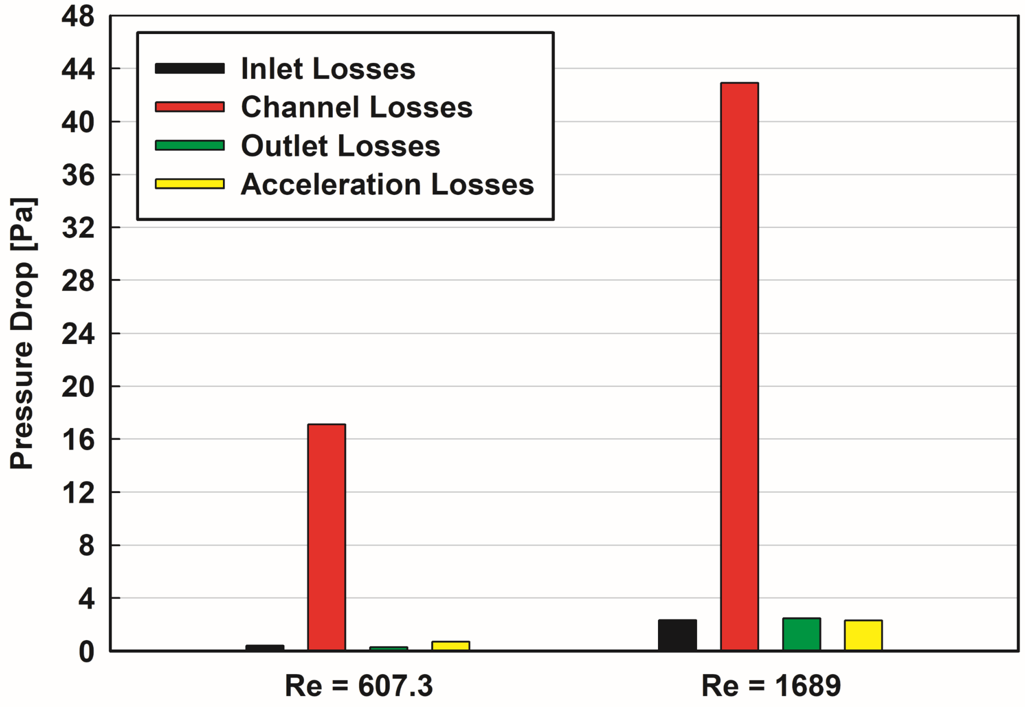

Figure 5.6 Minor losses in baseline ACC test section

As demonstrated by Figure 5.6, the minor losses due to the contraction, expansion, and heated acceleration of the flow were much smaller than the losses through the channel. While the equations for the loss coefficients, defined in Chapter 4, predicted small losses, they were based on ideal contraction and expansion scenarios that were not present in the test section. These losses were small enough that any discrepancies would not significantly impact the accurate characterization of the channel losses.

The measured channel pressure drop, less minor losses across the condenser assembly, is plotted against the mean channel velocity in Figure 5.7 for the baseline and reed-enhanced condensers.

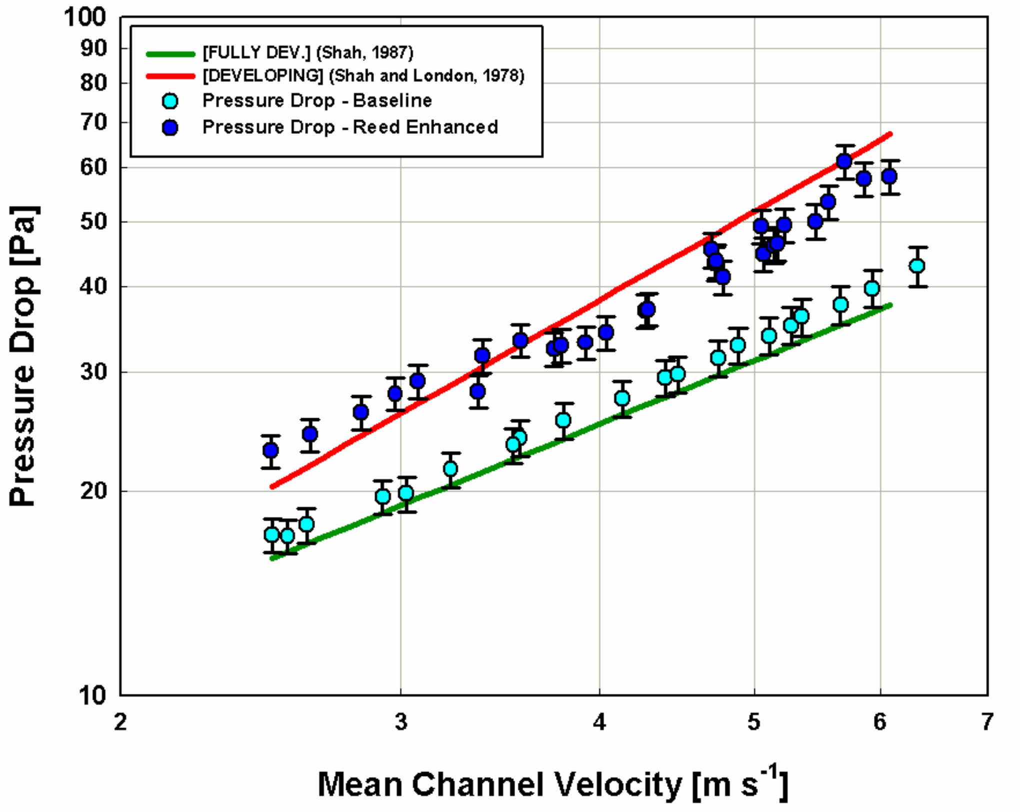

Figure 5.7 Pressure drop vs. channel velocity

The pressure drop data were used to calculate the friction factors through the finned ACC channels. The results for the baseline and reed-enhanced test sections are shown in Figure 5.7. The predicted friction factors for developing (Shah and London, 1971) and fully-developed (Bhatti and Shah, 1987) rectangular duct flow were calculated for comparison with the data from the ACC test facility.

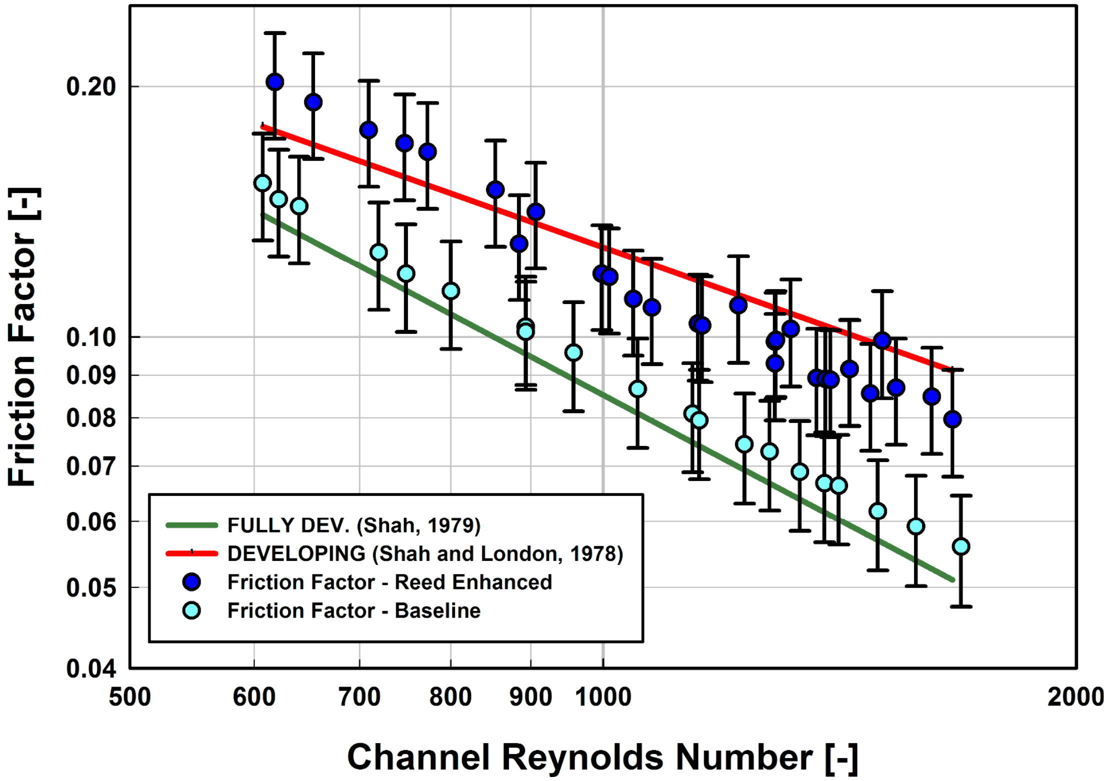

Figure 5.8 Darcy friction factor vs. Reynolds number

The calculated friction factor for the baseline ACC test section was in close agreement with the predicted friction factor results, being slightly higher than the fully developed flow friction factor prediction. The trend followed the predicted friction factor closely, with values representative of a combination of fully-developed and developing flows. As noted in Section 5.2.1, fully developed flow was predicted at the exit of the channel for all test cases, with development lengths ranging from 35 – 95 mm.

A decrease in reed-enhanced channel pressure drop occurred at a mean channel velocity of approximately 3.7 m s^{-1}, corresponding to a channel Reynolds number of approximately 900. As noted previously, an increase in measured Nusselt number occurred at approximately the same flow rate. The decrease in pressure drop is likely due to the onset of reed flutter, after which the pressure drop increased proportionally with respect to channel velocity. Before the reeds began to flutter, they were statically bonded to the channel walls, effectively blocking some of the inlet flow area, which leads to an increase in inlet pressure losses as well as slightly higher local channel velocities. Additionally, adjacent reeds became statically bonded to one another outside the channels, in the region between the reed support post inlet to the air channels, which can lead to the complete blockage of flow through their respective channels until the force imparted by the air is large enough to separate them. These two effects increased the pressure drop as channel velocity increased up until most reeds were fluttering within their respective channels, at which point they no longer interacted with the walls or other reeds in adjacent channels.

Reed-enhanced pressure drop was measured to be greater than baseline channel pressure drop by approximately 30 – 40% across the range of channel velocities measured in the ACC test facility. Baseline pressure drop through the channels ranged from 17.4 – 45.5 Pa, and reed-enhanced measurements demonstrated increased channel losses ranging from 24.4 – 58.7 Pa. The channel pressure drop could further increase in reed-enhanced condensers with reeds in every channel, as the reed-enhanced test section only contained reeds in approximately 92% of channels. The influence of channels without reeds in the reed-enhanced case was not explicitly investigated, although there is potential for higher pressure drop across the test section with reeds in each channel due to the reduced number of low-pressure drop flow paths.

5.3.2 Friction Factor Expressions

The friction factor results were curve-fit for implementation into the ACC Rankine cycle analysis program. Equation (5.3) illustrates the general form of the friction factor expression.

$$f(\mathrm{Re}) = A \cdot \mathrm{Re}^{B} \tag{5.3}$$

Table 5.4 Baseline and reed-enhanced friction factor curve-fit coefficients

Test Case	*A*	*B*	R^2
Baseline	85.53	-0.992	0.998
Reed	102.5	-0.972	0.972

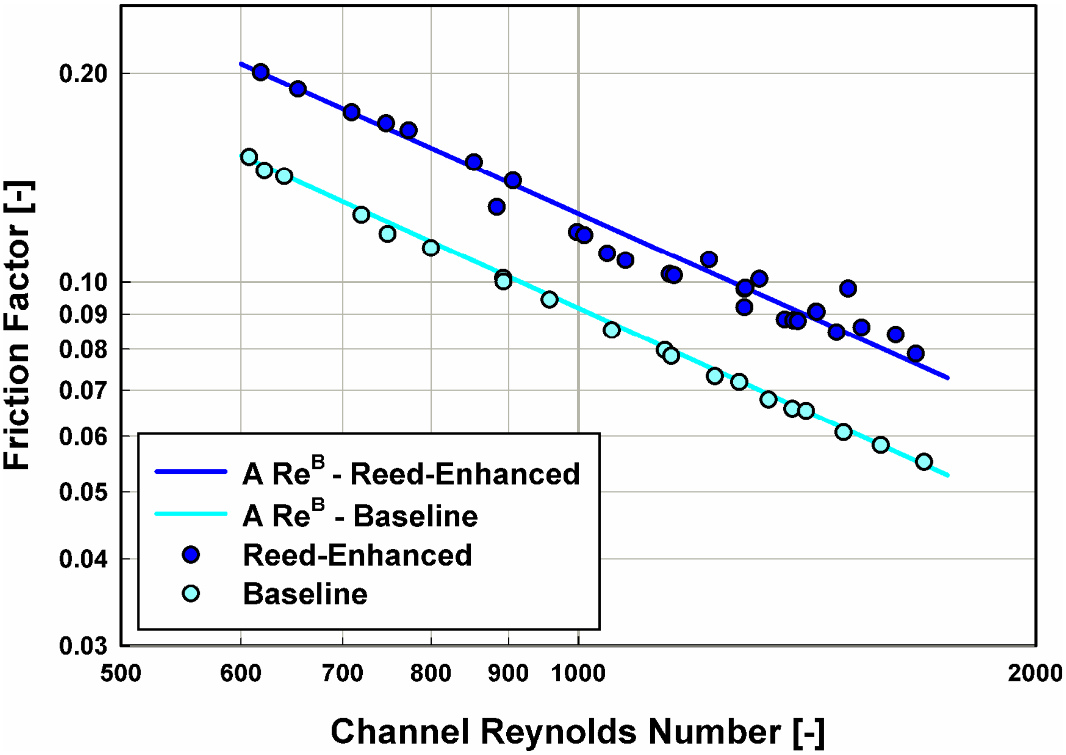

Figure 5.9 Friction factor expressions corresponding to Table 5.4

The curve-fit results for both baseline and reed-enhanced test cases demonstrated close agreement with the measured data points as demonstrated by R^2 values of 0.999 and 0.972, respectively. The average deviation, absolute average deviation, and standard deviation for baseline and reed-enhanced friction factor curve-fits are included in Table 5.5.

Table 5.5 Figures of merit for friction factor curve-fits

Test Case	*AD*	*AAD*	*SD*
Baseline	1.02×10^{-5}	8.33×10^{-4}	1.16×10^{-3}
Reed	8.14×10^{-5}	4.78×10^{-3}	5.77×10^{-3}

5.4 Plant Level Impact of AFR Installation

The goal of this investigation was to experimentally determine the plant level efficiency impact from the installation of auto-fluttering reeds in ACC air flow channels. The curve-fit relationships for Nusselt number and friction factor, from Sections 5.2.2 and 5.3.2 respectively, were implemented into the ACC design code developed by Lin (2016) to analyze the plant-level efficiency impact of AFR installation. The following sections detail the ACC and Rankine cycle input parameters and the effect of AFR installation on power plant performance.

5.4.1 Condenser and Cycle Model Inputs

Inputs to the segmented condenser models were determined based on information provided by EPRI (EPRI, 2013). The A-frame condenser module analyzed has a footprint of 12.2 m × 12.2 m, with an inclined tube length of 10.7 m. Steam is supplied to each condenser module at 7 kg s^{-1}, and the inlet saturation temperature is calculated to satisfy a condenser exit sub-cooling requirement of 2°C. Tube and fin dimensions, as shown in Figure 5.10, are included in Table 5.6.

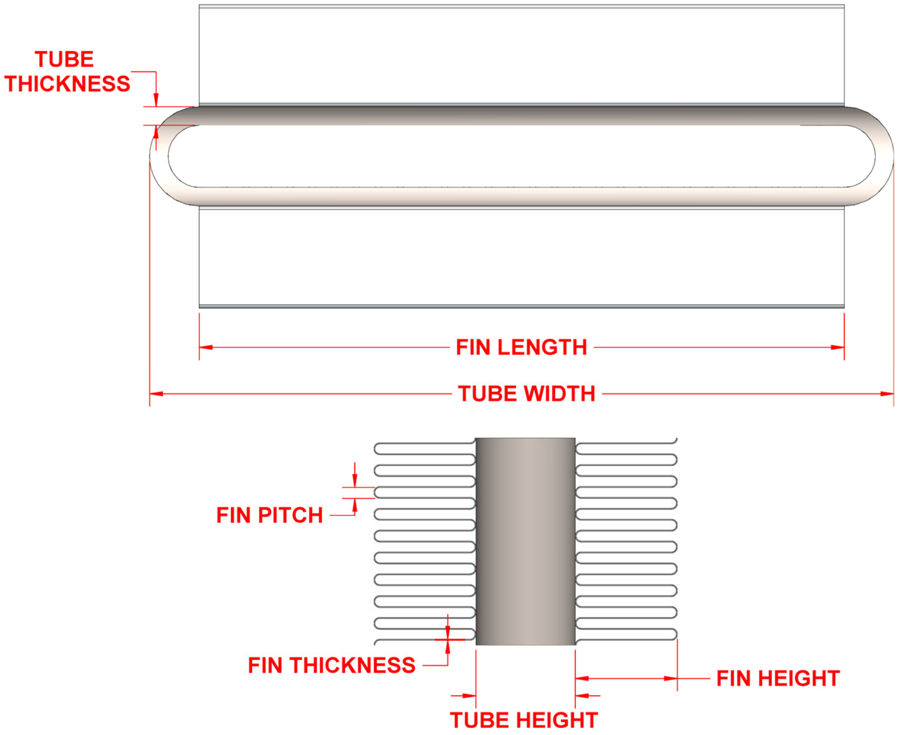

Figure 5.10 Tube and fin geometry

Table 5.6 Tube and fin dimensions

Dimension Name (units)	*Value*
Fin Length (m)	0.165
Fin Thickness (mm)	0.254
Fin Height (mm)	25.4
Fin Pitch (mm)	2.79
Tube Height (m)	0.0254
Tube Width (m)	0.191
Tube Thickness (mm)	1.27

The Rankine cycle model described in Chapter 4 is a simple superheated Rankine cycle with no reheating or regenerative stages with a net plant output of 500 MW that utilizes the data from the previously described test facility to determine plant output parameters as a function of condenser performance. The maximum cycle temperature is 550°C, with a boiler saturation temperature of 350°C. Figure 5.11 shows a schematic of the cycle under consideration in this study. The ambient temperature was assumed to be 30°C, and component efficiencies were based on industry standard values. The number of ACC modules was selected based on the required condensate mass flowrate. Table 5.7 includes the parameters used to calculate the overall plant output parameters.

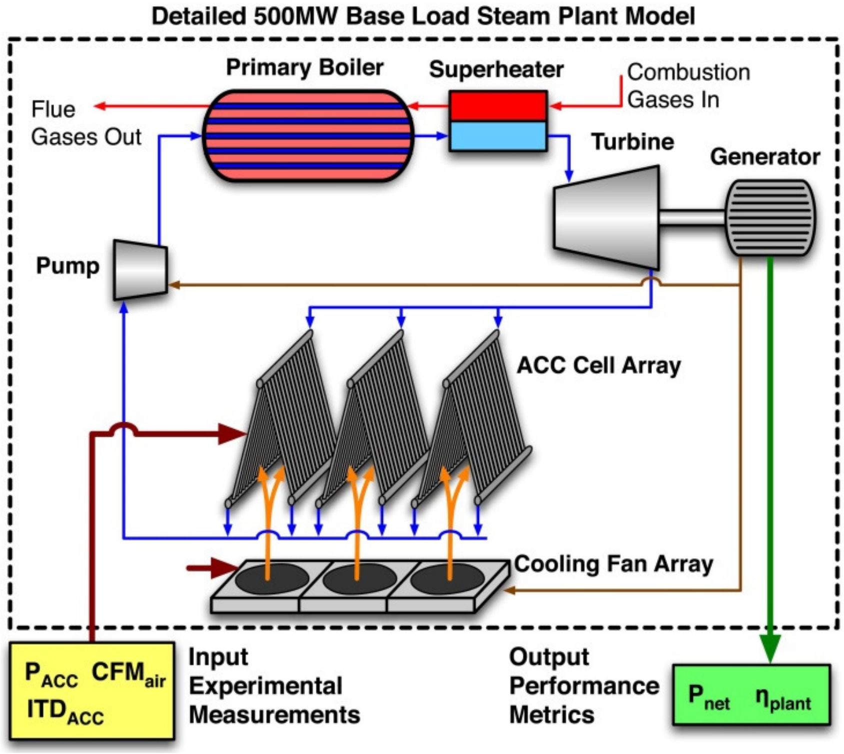

Figure 5.11 Rankine cycle model overview

Table 5.7 Rankine cycle input parameters

$T_{ambient}$ (°C)	Net Work Output (MW)	T_{max} (°C)	Steam Mass Flowrate ($kg\ s^{-1}$)	η_{fan}	$\eta_{turbine}$	η_{pump}
30	500	550	490	0.55	0.85	0.95

5.4.2 ACC Module Pressure Drop Breakdown

The minor losses across the various support structures, debris screens and walkways as well as the losses resulting from the jetting and recombination of air flow between adjacent condenser cells accounted for the most significant portion of the pressure drop in the unit whereas the channel pressure drop only accounted for approximately 20 – 30% of the total losses. Therefore, despite increases in the total channel pressure drop, the overall pressure drop through the condenser cell did not increase sufficiently to result in a reduction of the overall cycle efficiency at low channel Reynolds numbers. Figure 5.12 illustrates the relative pressure drops from the various minor losses and the air channel pressure drop through the condenser module.

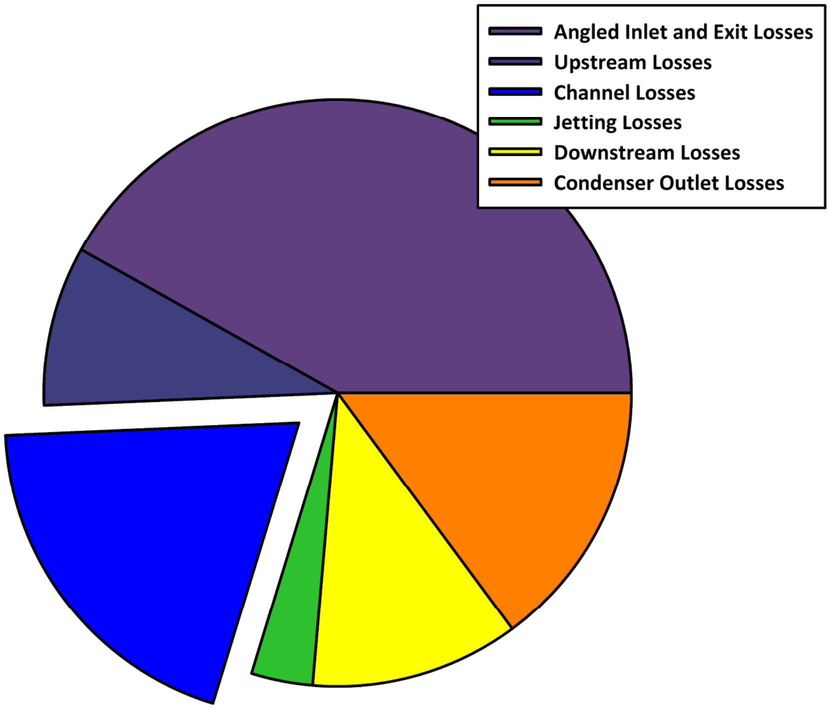

Figure 5.12 Distribution of pressure drop through ACC module

5.4.1 Plant Efficiency Optimization

Parametric optimization for air-side flow rate was performed to determine the maximum cycle efficiency for both the baseline and reed-enhanced condenser geometries. The mass flow rate through a single condenser module was varied from 500 – 880 kg s^{-1} at an ambient temperature of 30°C and the ITD and required fan work were evaluated for the standalone condenser assembly. The ITD and fan work are plotted in Figure 5.13 for the baseline and reed-enhanced condenser geometries.

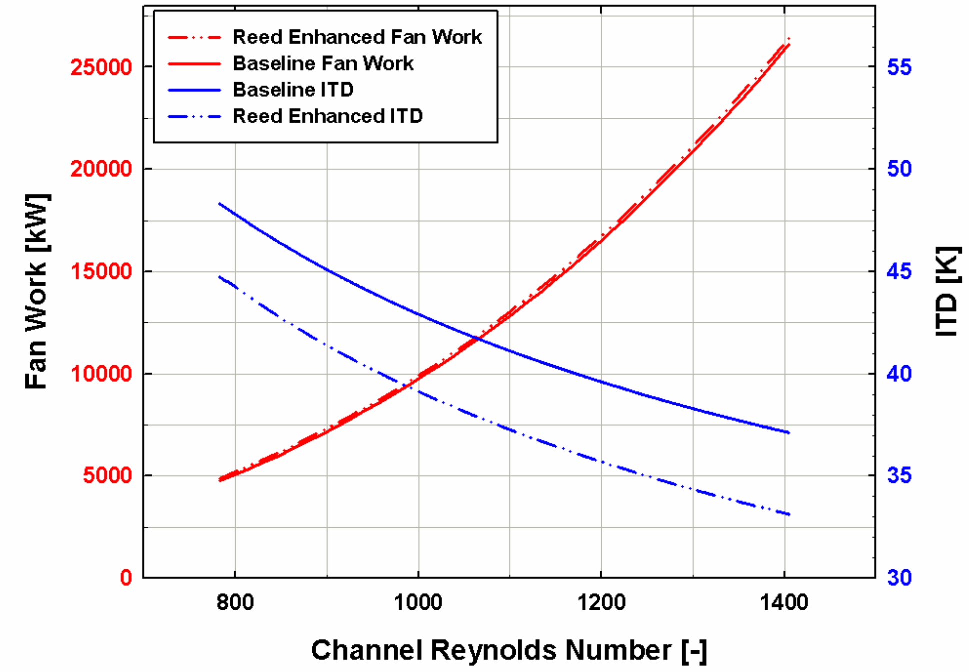

Figure 5.13 Fan work and ITD vs. ACC channel Reynolds number

The required fan work increased significantly as mass flow rate through the module increased, while the ITD decreases rapidly at the lower range of flow rates and slightly less quickly above a Reynolds number of 1000. The trade-off between a decrease in steam saturation temperature, which leads to increased turbine output, and increased electrical work input to the fans was critical to maximizing overall plant efficiency. For the reed-enhanced condenser, the fan work increases with volumetric flow rate in the channels at $d\dot{W}_{fan,total}/d\,\mathrm{Re}\big|_{\mathrm{Re}=800} = 291$ kW, rising to 850 kW at the highest flow rates considered. ITD, however, decreases from $dITD/d\,\mathrm{Re}\big|_{\mathrm{Re}=800}$ = -0.495 K to -0.165 K from the lowest to the highest flow rates, leading to the penalty for increased fan power more than compensating for the lower saturation pressure at higher air-side volumetric flow rates. Figure 5.14 shows the derivative of the ITD and fan work with respect to Reynolds number, illustrating the increasing fan power penalty and the simultaneous diminishing improvement in ITD as Reynolds numbers increase.

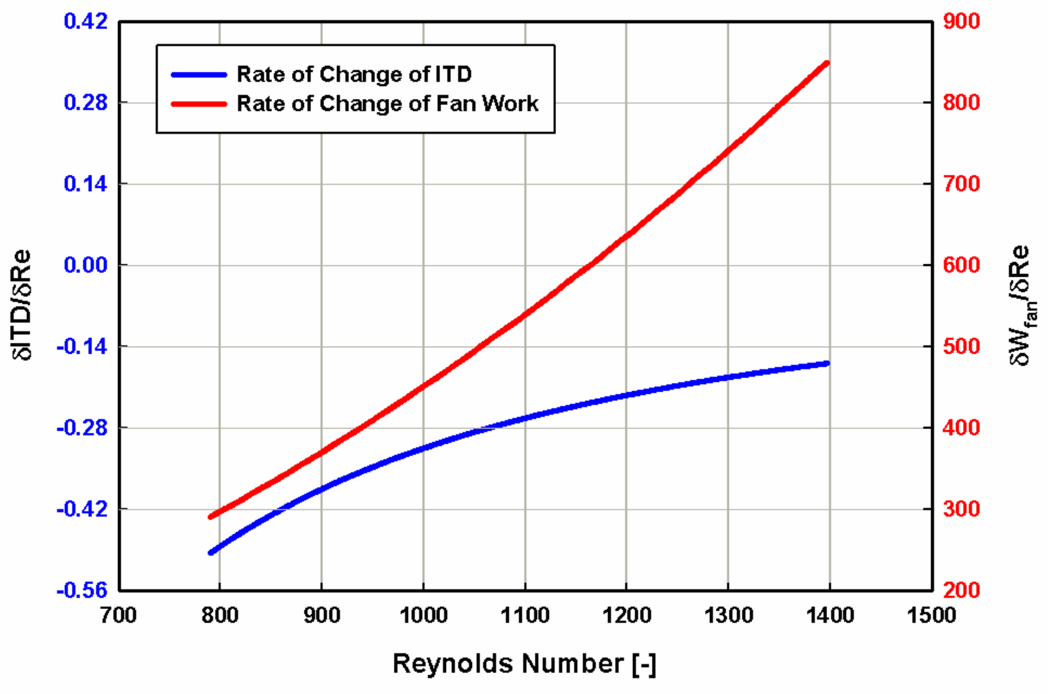

Figure 5.14 Derivatives of ITD and fan work vs. ACC channel Reynolds number

While standalone condenser performance was important in increasing the efficiency of AFR assemblies, the effect of condenser performance on plant-level efficiency is more relevant to plant operators and utilities and drives the potential for the adoption of this technology. Based on the steam condensation temperature required for full condensation along the length of the condenser tubes as well as the fan work input to the cycle to overcome the pressure drop through the air channels at a given volumetric flow rate, the standalone condenser model was coupled with a Rankine cycle model to determine the overall efficiency as a function of the air-side flow rate. The results for plant efficiency optimization with respect to the air-side Reynolds number for the baseline and reed-enhanced condenser geometries are included in Figure 5.15.

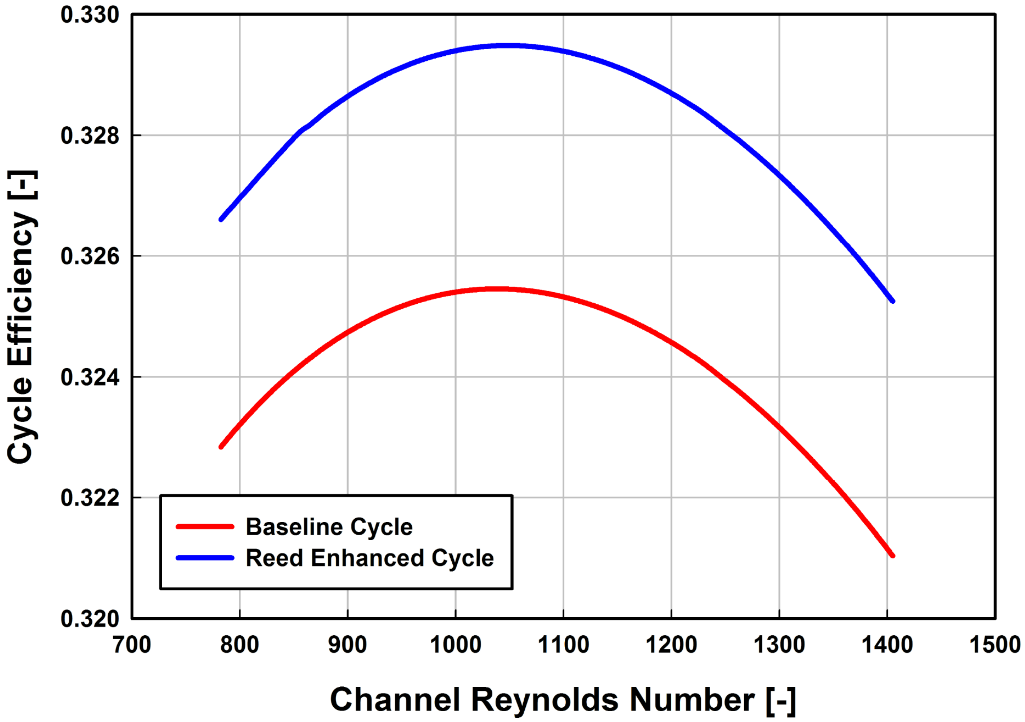

Figure 5.15 Plant efficiency vs. ACC channel Reynolds number

The maximum cycle efficiency occurred at Re = 1038 and Re = 1054 for the baseline and reed-enhanced ACC geometries, respectively. The maximum predicted plant efficiencies for baseline and reed-enhanced condenser geometries were 32.55% and 32.95%, respectively. Reed installation and the associated increase in heat transfer coefficient yielded an overall efficiency gain of approximately 0.4% over the baseline condenser geometry, despite an increase in required fan work input to the ACC array from

10.86 to 11.53 MW. Table 5.8 includes the relevant plant output performance variables from the baseline and reed-enhanced condenser models. Work increases in the turbine due to an increased turbine pressure ratio, but channel losses slightly increase the overall pressure drop and corresponding fan work into the ACC modules.

Table 5.8 Relevant plant variable outputs with baseline and reed-enhanced condensers

Test Case	*ITD (K)*	*Module ΔP (Pa)*	*Total Fan Work (MW)*	*Turbine Work (MW)*	*Turbine Outlet Pressure (kPa)*
Baseline	42.19	149.2	10.86	516.0	34.3
Reed	38.10	155.9	11.52	525.4	28.7

5.4.2 Plant Efficiency as Function of Ambient Temperature

The cycle efficiency for power plants with air-cooled condensers is known to suffer dramatically at elevated ambient conditions, requiring the reduction of plant power output to ensure that the condenser array can meet the required cooling demands without significantly increasing steam-side saturation temperature at the exit of the turbine. Effective condenser enhancement strategies require performance gains across a range of operating conditions including temperature and humidity.

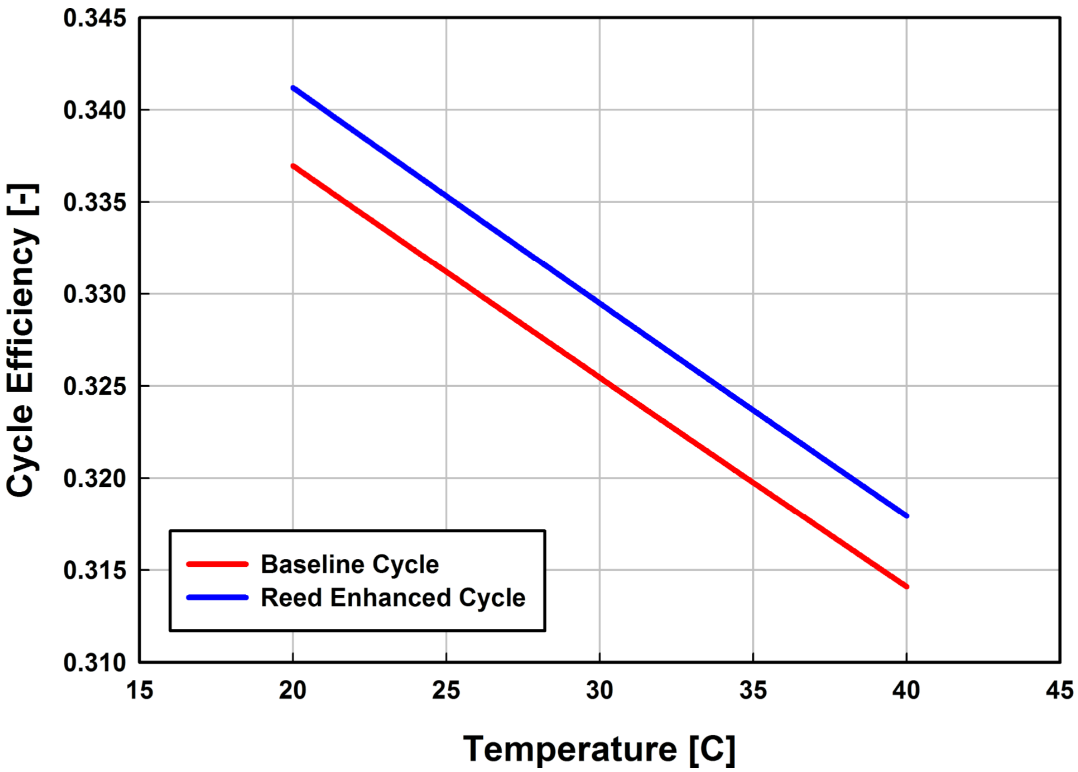

Figure 5.16 Optimized plant efficiency vs. ambient air temperature

Figure 5.16 illustrates the cycle efficiency for baseline and reed-enhanced geometries at varying ambient temperature conditions. While elevated ambient temperatures did result in cycle efficiency decreases, the effect of humidity was not significant in affecting the cycle efficiency for either the reed or baseline cycle predictions, with both predicting a 0.04% increase in cycle efficiency with an increase of relative humidity from 0.1 to 0.7. Additionally, the cycle performance enhancements associated with AFR installation to the ACC array were realized over the entire range of ambient temperatures considered.

5.5 Results Summary

The data from the experiments reported in the previous chapter were analyzed to obtain and correlate Nusselt numbers and friction factors for baseline and reed-enhanced condenser geometries. They were then used in a standalone ACC condenser analysis model to evaluate the improvement in condenser performance and the associated fan power increase due to the installation of the reeds. Finally, the condenser model was coupled with an ACC Rankine cycle analysis model to assess plant level performance for baseline and reed enhanced cases. Nusselt number enhancements of up to 27% were demonstrated at a pressure drop penalty of up to 38%. Power plant efficiency was determined to increase by up to 0.4% at the air-side flow rate corresponding to the optimum cycle performance. Similar gains were demonstrated at elevated ambient temperatures and humidity, demonstrating the plausibility of AFR enhancements to help improve siting options for ACCs in harsher ambient environments.

CHAPTER 6: CONCLUSIONS AND RECOMMENDATIONS

6.1 Conclusions

An investigation of methods to improve air-cooled condenser performance for implementation in power plants was conducted. Specifically, the installation of auto-fluttering reeds in the fin passages of air-cooled condensers was studied, with the objective of enhancing heat transfer, and approaching the performance of conventional wet-cooled power plants. A test section representative of an air-cooled power plant condenser was developed and tested in a wind tunnel test facility capable of supplying hot water for the tube side of the heat exchanger at temperatures up to 115°C and flow rates up to 0.4 kg s^{-1}. Heat transfer and pressure drop characteristics of the fully instrumented test section were measured over a range of air-side Reynolds numbers from 600 – 1700, conditions characteristic of those seen in power plant ACCs. Baseline condenser performance was measured first across the range of operating conditions for ACC modules, followed by the installation of AFR assemblies into the air channels and the same measurements of heat transfer coefficient and pressure drop of this enhanced configuration. The data were analyzed to obtain friction factors and Nusselt numbers as a function of Reynolds number for both configurations. Uncertainty analyses were also performed. Nusselt number and friction factor correlations were developed from the data for use in a condenser design and analysis model, and an ACC Rankine cycle power plant model. Parametric analyses were conducted using these models to assess the improvement in plant performance over a range of air flow rates and operating ambient temperatures.

Nusselt numbers demonstrated the influence of developing flow over a portion of the fin channel length, with values ranging from 5.2 – 6.5 and 6.2 – 8.4, for the baseline and enhanced configurations, respectively. The average enhancement in Nusselt number over the range of conditions tested was approximately 25%. The enhancement increased with Reynolds number due to the continued increase in effectiveness of the reed flutter mechanism at higher channel velocities. Measured friction factors within the test facility increased by 35 – 38% over the baseline values across the range of Reynolds numbers investigated. The data are included for reference in Figure 6.1. The Nusselt number and friction factor enhancement ratios are plotted against the channel Reynolds number in Figure 6.2.

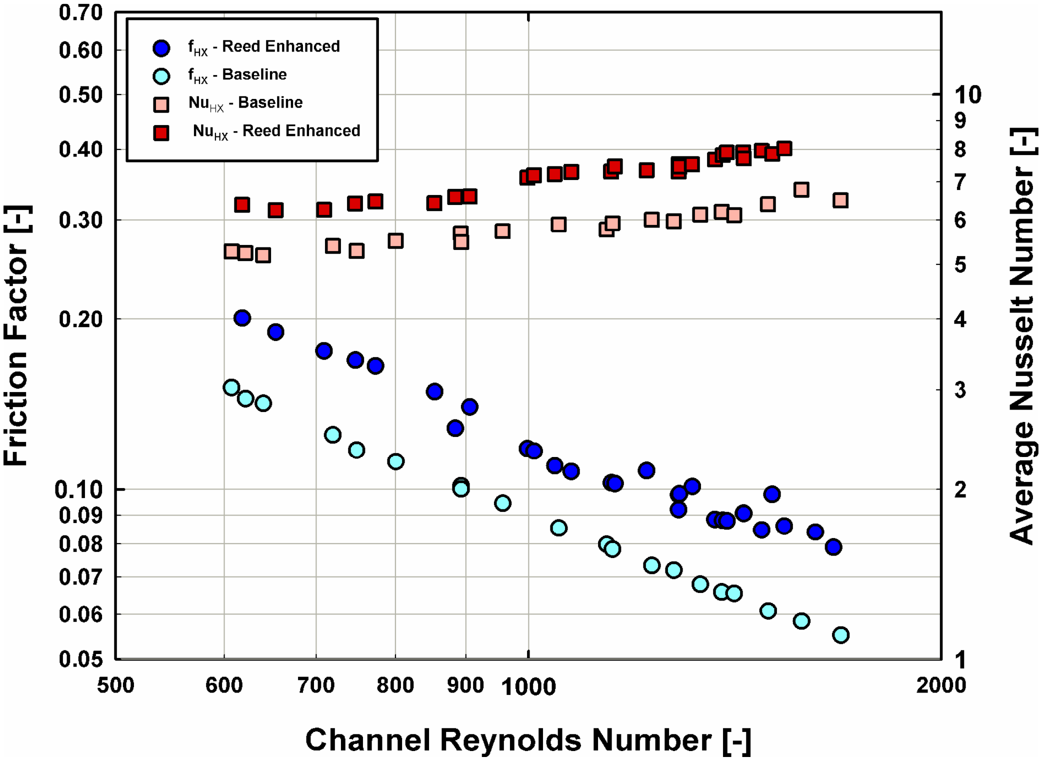

Figure 6.1 Nusselt number and friction factor vs. Reynolds number

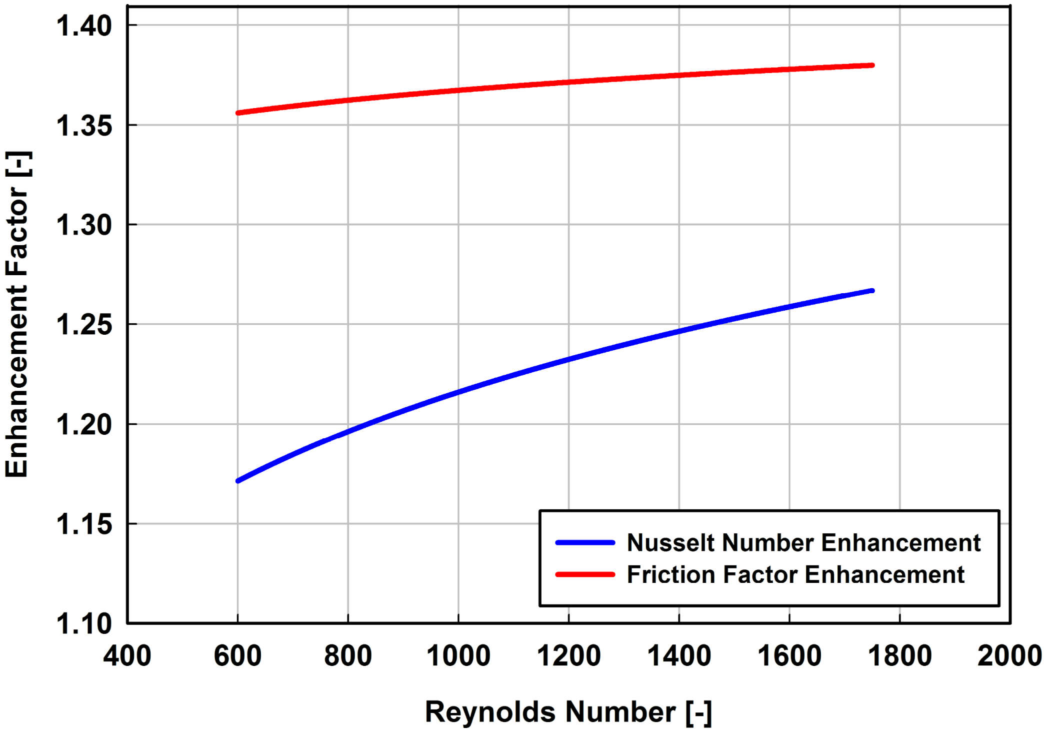

Figure 6.2 Enhancement of Nu and f vs. Reynolds number

The ACC Rankine cycle analysis program developed by Lin (2016) was used in conjunction with the Nusselt number and friction factor correlations developed here to determine the plant-level efficiency gains realized with AFR installation. Parametric evaluation was performed to determine the optimal cycle efficiency as a function of the air-side flow rate through the condenser modules. Figure 6.3 illustrates the relationship between initial temperature difference, defined as the difference between steam condensation temperature and inlet air temperature supplied to the ACC module, and fan work as a function of the air channel Reynolds number.

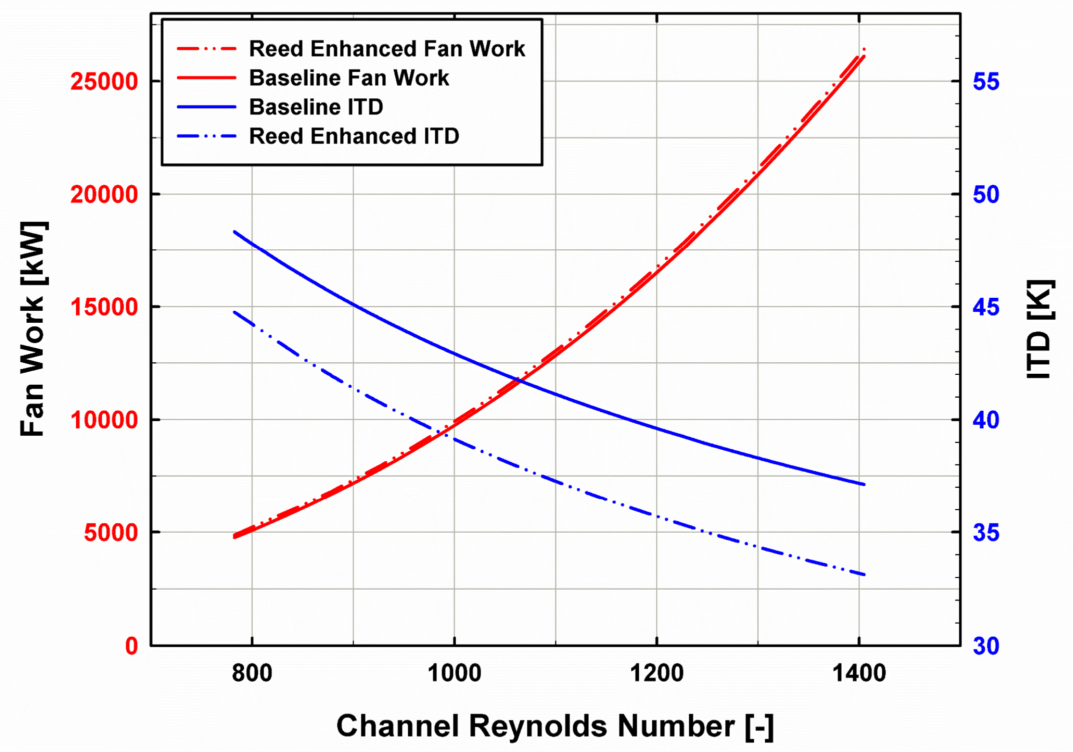

Figure 6.3 ITD and fan work for baseline and reed enhanced condensers

Cycle efficiency increases due to AFR Nusselt number enhancement were counteracted to some extent by the commensurate friction factor and fan power increases, which reduced the net power output for a given cycle heat input. However, increases in the fan work were outweighed by decreases in steam condensation temperature and thus, decreases in turbine back pressure, leading to increased cycle efficiency across the full range of Reynolds numbers considered over the baseline condenser module. A maximum gain in efficiency of 0.4% was demonstrated at the plant-level, with the maximum efficiency occurring at approximately the same air-side flow rate for baseline and reed enhanced condensers. Equivalent cycle efficiency gains were realized at elevated ambient temperatures and humidity, demonstrating the effectiveness of the reeds at a variety of operating conditions and environments. The Rankine cycle efficiency for a 500 MW representative power plant operating at an ambient temperature of 30°C with and without AFR installation on the condenser is shown in Figure 6.4.

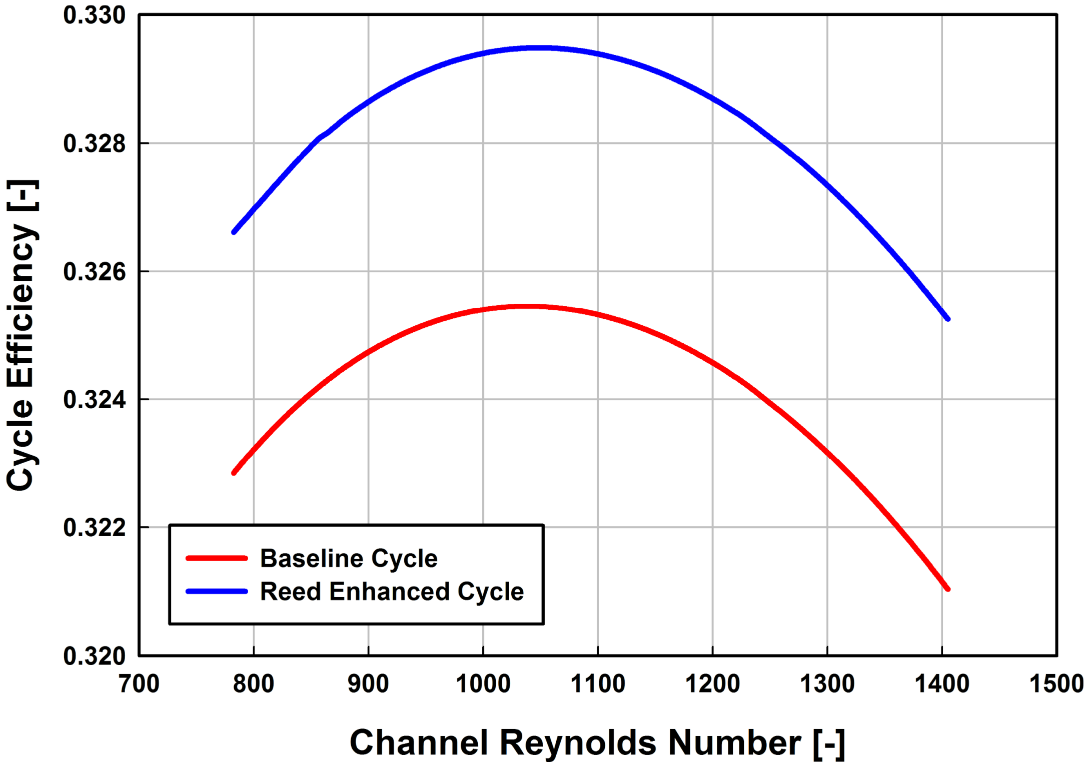

Figure 6.4 Cycle efficiency vs. air-side Reynolds number

It can be seen that AFR installation improves the performance of Rankine cycle thermal power plants with air-cooled condensers. Gains in cycle efficiency lead to lower emissions per unit power output as well as decreased water withdrawal needs, both of which will be ever more significant issues in the coming decades as global power consumption per capita continues to grow.

6.2 Recommendations for Future Work

Based on the initial promise shown for the use of AFR enhanced condensers in ACC power plants, the following recommendations are presented to guide future investigations.

6.2.1 Reed Attachment and Installation

While the efficacy of reed enhancement was demonstrated within the wind tunnel test facility, further work is required before AFR installation in full-scale condenser assemblies can be implemented. The current process for reed installation and attachment is cumbersome, requiring upwards of sixteen man hours for installation of under six hundred AFR assemblies. Each ACC module has approximately 2.44 million air channels in which reeds would have to be secured. It is infeasible to employ manual installation of so many assemblies, and an automated manufacturing and installation process would have to be developed to efficiently install the reeds during production of the tubes. New reed geometries for improved ease of installation could also simultaneously employ different reed shapes that might further improve heat transfer performance without a commensurate increase in pressure drop.

Along with the development of reed installation mechanisms to minimize cost and time, a modified attachment scheme would be needed to secure AFRs within the channels even when channels are not precisely aligned. Reed attachment schemes that have self-alignment ability within the air channels would be beneficial to mitigating the difficulties of installation with poorly aligned channels. Such a scheme could take several forms, including but not limited to, clip-on style or magnetic attachments. Self-aligning attachment mechanisms would allow for straight-forward retrofitting of current ACC fleets, improving their performance at a low cost of investment. Additionally, self-centering reed attachments would ensure proper reed flutter mechanics and lower pressure drop penalties for a given heat transfer enhancement by minimizing the reed-to-wall interactions that detrimentally affect the performance of the reed-enhancement scheme.

6.2.2 Economic Feasibility

Economic analysis of AFR technology is necessary to prove that the capital costs of AFR installation in an ACC module are outweighed by increased plant efficiency and lower operating costs. While material costs of both the reed and attachment mechanism are expected to be minimal relative to the cost of the condenser array, installation cost and increased manufacturing time should be estimated to determine the real economic potential. Increasing cost of water withdrawal, and maintenance and potential replacement of AFR modules on a regular schedule should also be considered in such analyses. The option to use water spray on such enhanced ACCs on the days with very high ambient temperatures should also be considered, so that extreme ambient cases can also be handled without the installation of conventional wet-cooled condensers. These factors are heavily dependent on the attachment and installation schemes.

6.2.3 Tube-side Heat Transfer Enhancement

With increased air-side heat transfer coefficients, the tube-side thermal resistance may become a more significant portion of the overall thermal resistance between the condensing steam and air. Thus, improvements in tube-side heat transfer coefficient would make a considerable impact on steam condensation temperature without commensurate increases in electrical input to the ACC fans. With previous investigations demonstrating that tube-side heat transfer resistance could become significant when air-side resistances are decreased by up to 50%, techniques for tube side enhancement should be investigated. Finned surfaces, acoustic enhancement of condensation, and surface coatings all have been demonstrated to increase condensation rates in tubes without large increases in tube-side pressure drop.

APPENDIX A

SAMPLE CALCULATIONS

Fin and Tube Dimensions:

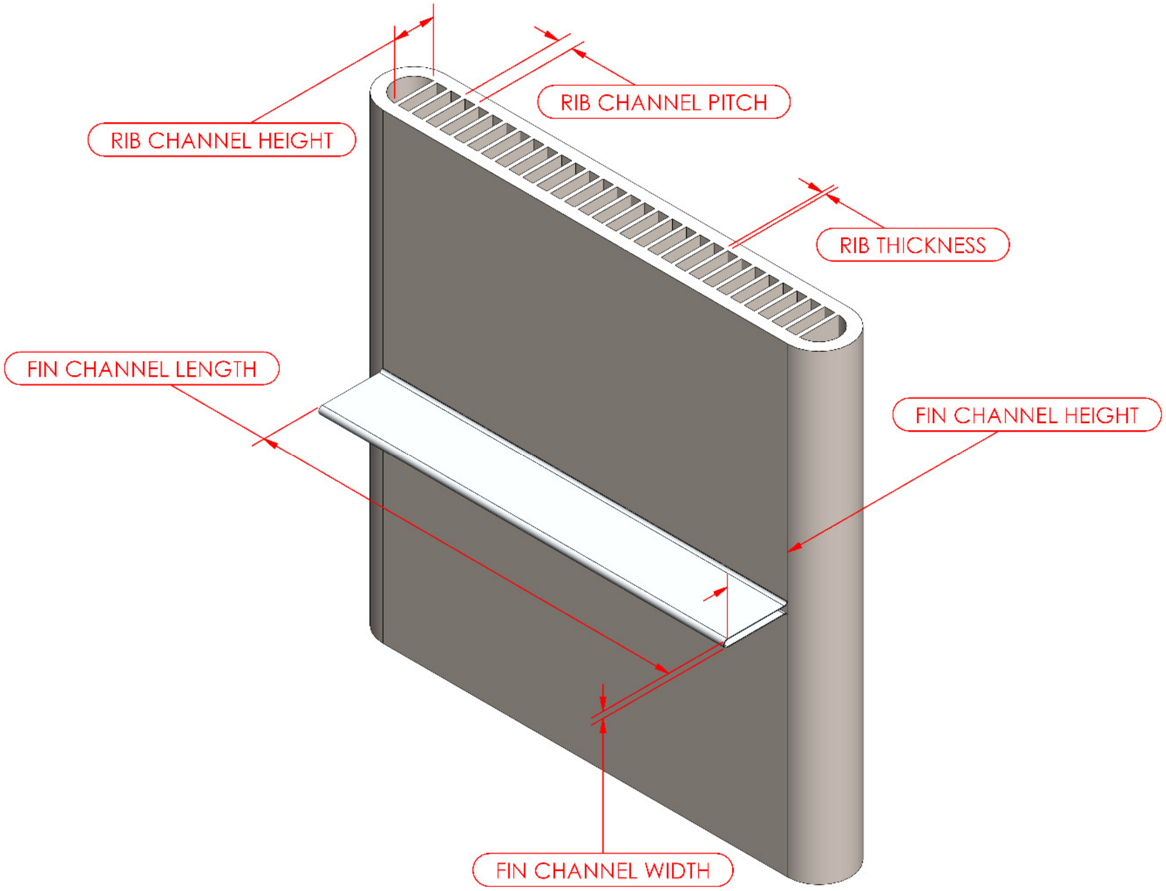

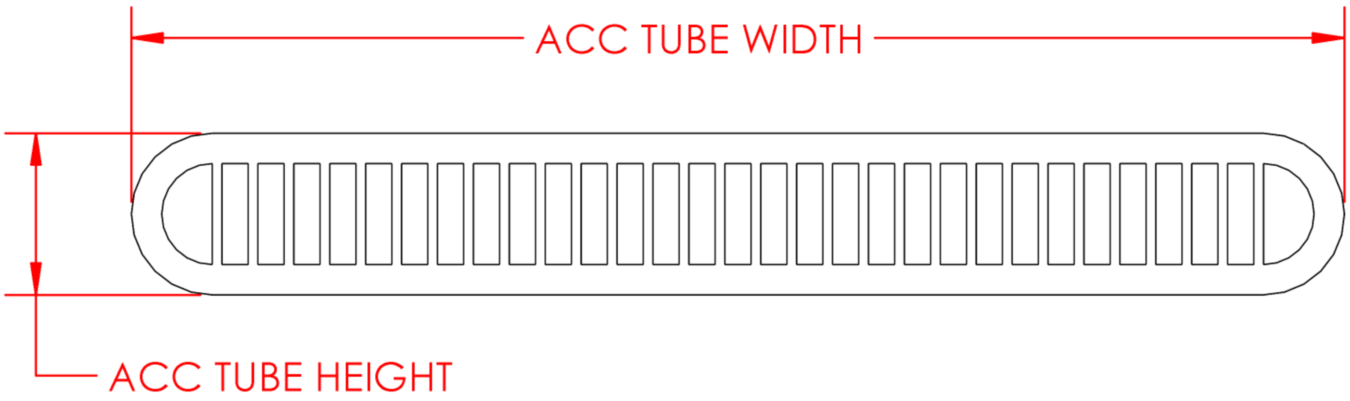

Internal Tube Geometry Sample Calculations		
Inputs	**Equations**	**Results**
Internal Surface Area Calculations		
$\boldsymbol{W}_{ACC,tube} = 0.1905$ m $\boldsymbol{H}_{ACC,tube} = 0.0254$ m $\boldsymbol{t}_{ACC,tube} = 4.8 \times 10^{-3}$ m $\boldsymbol{L}_{ACC,tube} = 0.4191$ m $\boldsymbol{n}_{ribs} = 30$	Rib Cross-sectional Area (single rib) $A_{rib,CS} = t_{rib} \cdot L_{rib}$	6.19×10^{-4} m
	Internal Tube Bare Surface Area (total heat exchanger) $A_{tube,int,bare} = A_{tube,\text{int}} - n_{tubes} \cdot \left(2 \cdot n_{ribs} \cdot L_{rib} \cdot t_{rib}\right)$	0.2025 m^2
	Internal Rib Surface Area (total heat exchanger) $A_{rib,wall} = n_{tubes} \cdot \left(n_{ribs} \cdot \left(2 \cdot H_{rib} \cdot L_{rib}\right)\right)$	0.7742 m^2

Internal Tube Geometry Sample Calculations

Inputs	Equations	Results
$n_{tubes} = 2$ $t_{rib} = 1.524$ mm $L_{rib} = 0.4064$ m $H_{rib} = 15.88$ mm	Cross-sectional Flow Area Blocked by Ribs (single tube) $A_{rib,blocked} = H_{rib} \cdot t_{rib} \cdot n_{ribs}$	7.26×10^{-4} m^2
	Water Flow Cross-sectional Area (single tube) $A_{tube,CS} = \underbrace{\frac{\pi}{4} \cdot \left(H_{ACC,tube} - 2 \cdot t_{ACC,tube}\right)^2}_{\text{Bullnose Area}} + \underbrace{\left(W_{ACC,tube} - H_{ACC,tube}\right) \cdot \left(H_{ACC,tube} - 2 \cdot t_{ACC,tube}\right)}_{\text{Rectangular Area}} - A_{rib,blocked}$	2.09×10^{-3} m^2

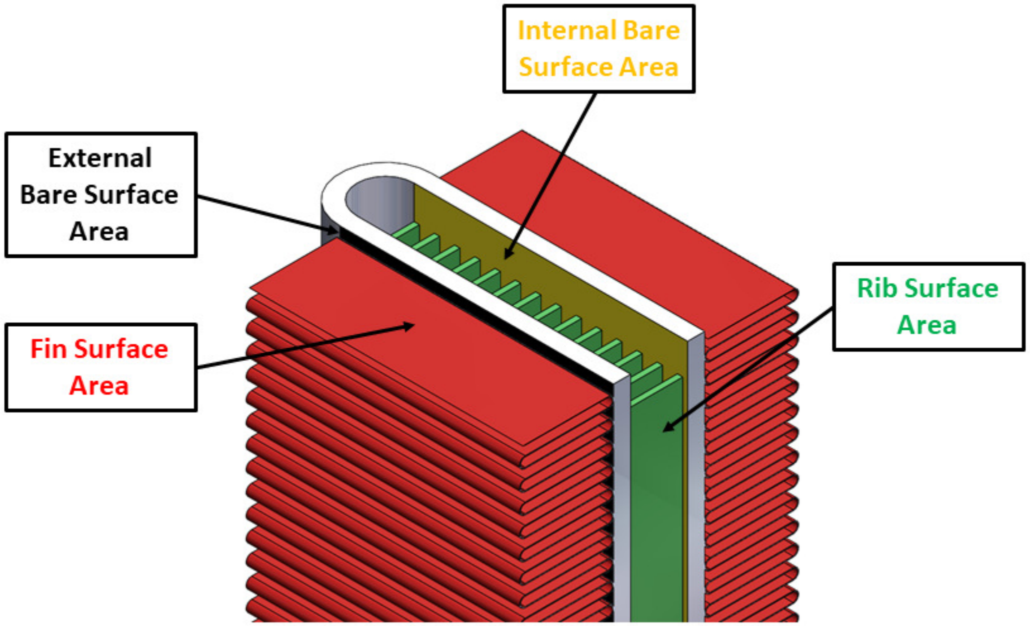

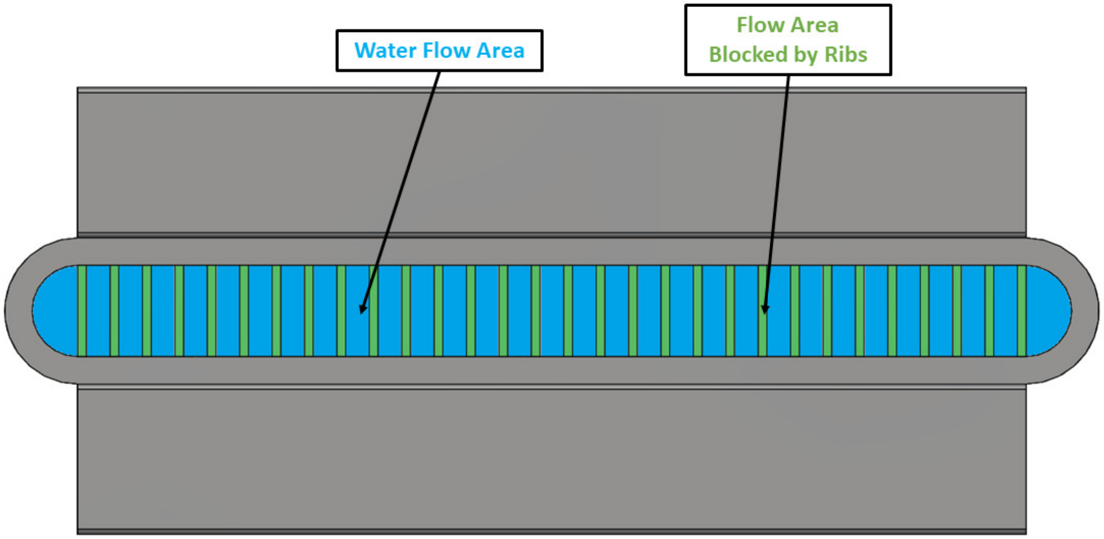

Air-Side Fin Geometry Sample Calculations		
Inputs	**Equations**	**Results**
Air-side Fin Area Calculations		
$W_{fin,channel} = 2.54$ mm $H_{fin,channel} = 0.0267$ m $L_{fin,channel} = 0.1651$ m	Fin Cross-sectional Area (single fin) $A_{fin,CS} = L_{fin,channel} \cdot t_{fin}$	4.19×10^{-5} m^2
	Fin Perimeter (single fin) $per_{fin} = 2 \cdot \left(L_{fin,channel} + t_{fin}\right)$	0.3307 m

Air-Side Fin Geometry Sample Calculations

Inputs	Equations	Results
$L_{ACC,tube} = 0.4191$ m $t_{fin} = 0.254$ mm $n_{fins} = 150$ $n_{tubes} = 2$	External Tube Flat Surface Area (total heat exchanger) $A_{tube,outer} = n_{tubes} \cdot \left(2 \cdot L_{fin,channel} \cdot L_{ACC,tube}\right)$	0.2768 m^2
	Fin Base Area on Tube (total heat exchanger) $A_{fin,base} = n_{tubes} \cdot \left(2 \cdot A_{fin,CS} \cdot n_{fins}\right)$	0.02516 m^2
	External Tube Bare Surface Area (total heat exchanger) $A_{tube,outer,bare} = A_{tube,outer} - A_{fin,base}$	0.2516 m^2
	Air Channel Hydraulic Diameter (single air channel) $D_{hy,fin,channel} = \frac{4 \cdot W_{fin,channel} \cdot H_{fin,channel}}{2 \cdot \left(W_{fin,channel} + H_{fin,channel}\right)}$	4.64×10^{-3} m
	Air Channel Cross-sectional Area (single air channel) $A_{fin,channel,CS} = W_{fin,channel} \cdot H_{fin,channel}$	6.77×10^{-5} m^2
	Fin Surface Area (total heat exchanger) $A_{fin} = n_{tubes} \cdot 2\left[\left(2 \cdot H_{fin,channel} \cdot L_{fin,channel}\right) \cdot n_{fins}\right]$	5.284 m

Water-Side Thermal Resistance Sample Calculations		
Inputs	**Equations**	**Results**
Tube-side Heat Transfer Analysis		
$n_{ribs} = 30$ $H_{rib} = 15.88$ mm $t_{rib} = 1.524$ mm $L_{rib} = 0.4064$ m $\varepsilon = 15 \times 10^{-6}$ m $per_{rib} = 0.8158$ m $A_{tube,CS} = 0.0021$ m^2 $A_{tube,\text{int},bare} = 0.2025$ m^2 $A_{rib,total} = 0.7742$ m^2 $\dot{m}_{water} = 0.3895$ kg s^{-1}	Rib Pitch (adjacent rib spacing plus thickness) $pitch_{rib} = \frac{\left(W_{ACC,tube} - H_{ACC,tube}\right) - t_{rib}}{n_{ribs} - 1}$	0.00564 m
	Rib Channel Hydraulic Diameter (single channel) $D_{hy,rib,channel} = \frac{4 \cdot H_{rib} \cdot (pitch_{rib} - t_{rib})}{2 \cdot \left(H_{rib} + (pitch_{rib} - t_{rib})\right)}$	0.02203 m
	Rib Channel Cross-sectional Area (single water channel) $A_{rib,channel,CS} = \left(pitch_{rib} - t_{rib}\right) \cdot H_{rib}$	6.54 × 10^{-5} m^2
	Rib Perimeter (single rib) $per_{rib} = 2 \cdot \left(t_{rib} + L_{rib}\right)$	0.8158 m
	Rib Channel Mass Flowrate (single water channel) $\dot{m}_{rib,channel} = \dot{m}_{water} \cdot \frac{A_{rib,channel,CS}}{A_{tube,CS}}$	0.01216 kg s^{-1}

Water-Side Thermal Resistance Sample Calculations

Inputs	Equations	Results
Thermophysical Properties: k_{rib} = 15 W m^{-1} K^{-1} $\bar{\rho}_{water}$ = 948.1 kg m^{-3} $\bar{\mu}_{water}$ = 0.000246 kg m^{-1} s^{-1} Pr_{water} = 1.523 $\bar{k}_{water}$ = 0.6826 W m^{-1} k^{-1}	Average Rib Channel Velocity (single water channel) $V_{water} = \frac{\dot{m}_{rib,channel}}{\bar{\rho}_{water} \cdot A_{rib,channel,CS}}$	0.1963 m s^{-1}
	Rib Channel Reynolds Number (single channel) $Re_{water} = \frac{\bar{\rho}_{water} \cdot V_{water} \cdot D_{hy,rib,channel}}{\bar{\mu}_{water}}$	4955
	Rib Channel Equivalent Circular Friction Factor (single channel) $A = \left(2.457 \cdot ln\left(\left((7/Re_{water})^{0.9} + 0.27 \cdot \varepsilon / D_{hy,rib,channel}\right)^{-1}\right)\right)^{16}$ $B = (37530/Re_{water})^{16}$ $f_{circ} = 8 \cdot \left((8/Re_{water})^{12} + (A+B)^{-1.5}\right)^{1/12}$	A = 2.197 × 10^{18} B = 1.173 × 10^{14} f_{circ} = 0.04077
	Rib Channel Aspect Ratio (single channel) $\alpha = \frac{(pitch_{rib} - t_{rib})}{H_{rib}}$	0.2593

Water-Side Thermal Resistance Sample Calculations		
Inputs	**Equations**	**Results**
	Effective Friction Factor with Bhatti-Shah Correction (single channel) $f = f_{circ} \cdot (1.0875 - 0.1125 \cdot \alpha)$	0.04315
	Rib Channel Nusselt Number (single channel) $A = \dfrac{1}{\left(6.3 + \dfrac{0.079 \cdot (f/8)^{0.5} \cdot Re_{water} \cdot Pr_{water}}{\left(1 + Pr_{water}{}^{0.8}\right)^{5/6}}\right)^{2}}$ $Nu_t = \left(4.364^{10} + \left(\dfrac{exp\left(\dfrac{2200 - Re_{water}}{365}\right)}{4.364^{2}} + A\right)^{-5}\right)^{1/10}$	27.13
	Rib Channel Heat Transfer Coefficient (single channel) $h_{water} = \dfrac{Nu_t \cdot \overline{k}_{water}}{D_{hy,rib,channel}}$	2832 W m^{-2} K^{-1}

Water-Side Thermal Resistance Sample Calculations

Inputs	Equations	Results
	Rib Channel Fin Coefficient (single rib) $m_{rib}^{*} = \sqrt{\dfrac{h_{water} \cdot per_{rib}}{k_{rib} \cdot A_{rib,CS}}}$	498.7 m^{-1}
	Rib Channel Fin Coefficient (times length) [single rib] $m_{rib}^{*}L = \sqrt{\dfrac{h_{water} \cdot per_{rib}}{k_{rib} \cdot A_{rib,CS}}} \cdot \left(\dfrac{H_{rib}}{2}\right)$	3.959
	Rib Channel Fin Efficiency (single rib) $\eta_{rib} = \dfrac{tanh\left(m_{rib}^{*}L\right)}{m_{rib}^{*}L}$	0.2524
	Tube-side Thermal Resistance (total heat exchanger) $R_{water} = \dfrac{1}{h_{water} \cdot \left(A_{\text{int},bare} + \eta_{rib} \cdot A_{rib,wall}\right)}$	0.0008874 K W^{-1}

Tube Conduction Thermal Resistance Sample Calculations		
Inputs	**Equations**	**Results**
Planar Conduction Thermal Resistance		
$n_{ribs} = 30$ $\boldsymbol{W}_{ACC,tube} = 0.1905$ m $\boldsymbol{H}_{ACC,tube} = 0.0254$ m $\boldsymbol{t}_{ACC,tube} = 4.762 \times 10^{-3}$ m $\boldsymbol{L}_{ACC,tube} = 0.4191$ m **Thermophysical Properties:** $\boldsymbol{k}_{tube} = 15$ W m^{-1} K^{-1}	Tube Conduction Surface Area (total heat exchanger) $A_{cond} = n_{tubes} \cdot \left(2 \cdot \left(W_{ACC,tube} - H_{ACC,tube}\right) \cdot L_{ACC,tube}\right)$	0.2768 m^2
	Tube Conduction Thermal Resistance (total heat exchanger) $R_{cond} = \dfrac{t_{ACC,tube}}{k_{tube} \cdot A_{cond}}$	0.001147 K W^{-1}

Heat Transfer Sample Calculations		
Inputs	**Equations**	**Results**
Effectiveness-NTU Heat Transfer Analysis		
$\dot{\boldsymbol{m}}_{water} = 0.375$ kg s^{-1} $\dot{\boldsymbol{m}}_{air} = 0.09878$ kg s^{-1} $\boldsymbol{T}_{water,in} = 115.7$°C	Tube Heat Duty (single tube) $\dot{Q}_{water} = \dot{m}_{water} \cdot \bar{c}_{water} \cdot \left(T_{water,in} - T_{water,out}\right)$	6.14 kW
	Minimum Heat Capacity Rate (air-side) $\dot{C}_{min} = \bar{c}_{air} \cdot \dot{m}_{air}$	0.1070 kJ K^{-1} s^{-1}

Heat Transfer Sample Calculations		
Inputs	**Equations**	**Results**
$\boldsymbol{T}_{water,out}$ = 112.0°C $\boldsymbol{T}_{air,in}$ = 22.5°C $\boldsymbol{T}_{air,out}$ = 77.24°C **Thermophysical** **Properties:** $\bar{\boldsymbol{c}}_{water}$ = 4.233 kJ kg^{-1} K^{-1} $\bar{\boldsymbol{c}}_{air}$ = 1.084 kJ kg^{-1} K^{-1}	Maximum Heat Capacity Rate (water-side) $\dot{C}_{max} = \bar{c}_{water} \cdot \dot{m}_{water}$	1.649 kJ K^{-1} s^{-1}
	Heat Capacity Rate Ratio $C_r = \frac{\dot{C}_{min}}{\dot{C}_{max}}$	0.06491
	Tube Heat Transfer Effectiveness (total heat exchanger) $\varepsilon_{tube} = \frac{\dot{Q}_{water}}{\dot{C}_{min,} \cdot \left(T_{water,in} - T_{air,in}\right)}$	0.62
	Tube NTU Calculation (implicitly defined equation) $\varepsilon_{tube} = 1 - exp\left(\left(1/C_r\right) \cdot \left(NTU^{0.22}\right) \cdot \left(exp\left(-C_r \cdot \left(NTU^{0.78}\right)\right) - 1\right)\right)$	NTU = 0.99
	Overall Heat Transfer Coefficient (total heat exchanger) $UA = \dot{C}_{min} \cdot NTU$	106.5 W K^{-1}
	Overall Thermal Resistance (total heat exchanger) $R_{total} = \frac{1}{UA}$	0.009393 K W^{-1}

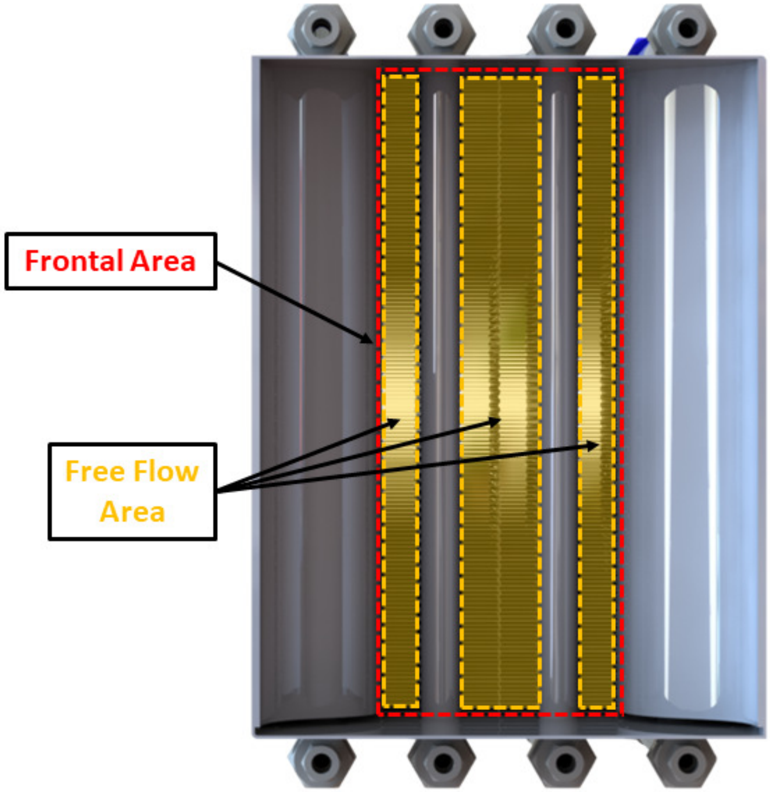

Air-Side Thermal Resistance/Heat Transfer Coefficient Sample Calculations		
Inputs	**Equations**	**Results**
Air-side Heat Transfer Coefficient Calculations		
$H_{fin,channel} = 0.0267$ m $W_{fin,channel} = 0.00254$ m	Channel Hydraulic Diameter (single air channel) $D_{hy,fin,channel} = \frac{4 \cdot W_{fin,channel} \cdot H_{fin,channel}}{2 \cdot \left(W_{fin,channel} + H_{fin,channel}\right)}$	0.004638 m

Air-Side Thermal Resistance/Heat Transfer Coefficient Sample Calculations		
Inputs	**Equations**	**Results**
$H_{ACC,tube} = 0.0254$ m $L_{ACC,tube} = 0.4191$ m $t_{fin} = 0.254$ mm $A_{tube,bare} = 0.1592$ m^2 $A_{fin,tube} = 2.516$ m^2 $per_{fin} = 0.3307$ m $R_{water} = 0.0008874$ K W^{-1} $R_{cond} = 0.001147$ K W^{-1} $\dot{V}_{air} = 0.1103$ m^3 s^{-1} $A_{ff} = 0.04065$ m^2 **Thermophysical Properties:**	Number of Air Channels Along Height $n_{fin,channels,H} = \dfrac{L_{ACC,tube}}{W_{fin,channel} + t_{fin}}$	150
	Number of Air Channels Along Width $n_{fin,channels,W} = 2 \cdot n_{tubes}$	4
	Total Number of Air Channels in Full Heat Exchanger $n_{fin,channels} = n_{fin,channels,H} \cdot n_{fin,channels,W}$	600
	Total Frontal Flow Area (total heat exchanger) $A_{fr} = L_{ACC,tube} \cdot n_{tubes} \cdot \left(2 \cdot H_{fin,channel} + H_{ACC,tube}\right)$	0.0660 m^2
	Minimum Free Flow Area (core area through heat exchanger) $A_{ff} = H_{fin,channel} \cdot W_{fin,channel} \cdot n_{fin,channels}$	0.0406 m^2
	Air Channel Velocity (average) $V_{channel} = \dfrac{\dot{V}_{air}}{A_{ff}}$	2.493 m s^{-1}

Air-Side Thermal Resistance/Heat Transfer Coefficient Sample Calculations

Inputs	Equations	Results
$k_{fin} = 220\ \mathrm{W\ m^{-1}\ K^{-1}}$ $\bar{\rho}_{air} = 1.026\ \mathrm{kg\ m^{-3}}$ $\bar{\mu}_{air} = 1.954 \times 10^{-5}\ \mathrm{kg\ m^{-1}\ s^{-1}}$ $R'' = 6 \times 10^{-6}\ \mathrm{m^2\ K\ W^{-1}}$	Air Channel Reynolds Number (single channel) $Re_{fin,channel} = \dfrac{\bar{\rho}_{air} \cdot V_{channel} \cdot D_{hy,fin,channel}}{\bar{\mu}_{air}}$	607.3
	Air Channel Fin Coefficient (single fin) $m^*_{fin} = \sqrt{\dfrac{h_{air} \cdot per_{fin}}{k_{fin} \cdot A_{c,fin}}}$	$33.50\ \mathrm{m^{-1}}$
	Air Channel Fin Coefficient (times length) [single fin] $m^*_{fin}L = \sqrt{\dfrac{h_{air} \cdot per_{fin}}{k_{fin} \cdot A_{c,fin}}} \cdot H_{fin,channel}$	0.8935
	Air Channel Fin Efficiency (single fin) $\eta_{fin} = \dfrac{tanh\left(m^*_{fin}L\right)}{m^*_{fin}L}$	0.7981
	Surface Efficiency Constant (overall surface) $C_1 = 1 + \eta_{fin} h_{air} \left[\dfrac{A_{fin}R''}{A_{c,fin}}\right]$	1.031

Air-Side Thermal Resistance/Heat Transfer Coefficient Sample Calculations

Inputs	Equations	Results
	Surface Efficiency (overall surface) $\eta_{o,c} = 1 - \frac{A_{fin}}{A_{fin} + A_{tube,outer,bare}} \left[1 - \frac{\eta_{fin}}{C_1} \right]$	0.784
	Surface Efficiency with zero contact resistance (overall surface) $\eta_o = 1 - \frac{A_{fin}}{A_{fin} + A_{tube,outer,bare}} \left[1 - \eta_{fin} \right]$	0.812
	Air Channel Thermal Resistance (total heat exchanger) $R_{air} = R_{total} - R_{water} - R_{cond}$	0.007358 K W^{-1}
	Air Channel Heat Transfer Coefficient (total heat exchanger) $h_{air} = \frac{1}{R_{air} \cdot \eta_{o,c} \left(A_{tube,outer,bare} + A_{fin} \right)}$	31.31 W m^{-2} K^{-1}

Air-side Friction Factor Sample Calculations		
Inputs	**Equations**	**Results**
Minor Loss Subtraction from Measured Pressure Drop		
$\dot{m}_{air} = 0.09878\ \text{kg s}^{-1}$ $L_{fin,channel} = 0.1651\ \text{m}$ $D_{hy,fin,channel} = 4.638\ \text{mm}$ $\Delta P_{measured} = 18.82\ \text{Pa}$ $A_{ff} = 0.0406\ \text{m}^2$ $A_{fr} = 0.0660\ \text{m}^2$ **Thermophysical Properties:** $\rho_{air,in} = 1.153\ \text{kg m}^{-3}$ $\rho_{air,out} = 0.8986\ \text{kg m}^{-3}$	Flow Velocity in Duct Preceding and Trailing Test Section $V_{air,frontal} = \dfrac{\dot{m}_{air}}{\rho_{air,in} \cdot A_{fr}}$	1.298 m s^{-1}
	Inlet Flow Velocity (immediately after entering air channel) $V_{air,in} = \dfrac{\dot{m}_{air}}{\rho_{air,in} \cdot A_{ff}}$	2.107 m s^{-1}
	Outlet Flow Velocity (immediately before exiting air channel) $V_{air,out} = \dfrac{\dot{m}_{air}}{\rho_{air,out} \cdot A_{ff}}$	2.705 m s^{-1}
	Contraction Ratio (from full flow to core area) $\sigma = A_{ff} \ / \ A_{fr}$	0.6158
	Contraction Coefficient $C_C = 1 - \dfrac{1-\sigma}{2.08(1-\sigma)+0.5371}$	0.7125

Air-side Friction Factor Sample Calculations		
Inputs	**Equations**	**Results**
	Inlet Contraction Loss Coefficient $K_{con} = \left(\frac{1}{C_C} - 1 \right)^2$	0.1628
	Outlet Expansion Loss Coefficient $K_{eo} = (1 - \sigma)^2$	0.1478
	Inlet Contraction Pressure Drop $\Delta P_{inlet} = K_{con} \cdot \frac{1}{2} \cdot \rho_{air,in} \cdot V_{air,in}{}^2$	0.4169 Pa
	Outlet Expansion Pressure Drop $\Delta P_{outlet} = K_{eo} \cdot \frac{1}{2} \cdot \rho_{air,out} \cdot V_{air,out}{}^2$	0.4851 Pa
	Channel Mass Flux (average) $G_{channel} = \frac{\dot{m}_{air}}{A_{ff}}$	2.43 kg s^{-1}

Air-side Friction Factor Sample Calculations

Inputs	Equations	Results
	Air-side Acceleration Pressure Drop $\Delta P_{accel} = \frac{G_{channel}^{2}}{2\rho_{air,in}} \cdot \left[\frac{\rho_{air,in}}{\rho_{air,out}} - 1 \right]$	0.7259 Pa
	Air-Side Frictional Pressure Drop $\Delta P_{channel} = \Delta P_{measured} - \Delta \mathrm{P}_{\mathrm{inlet}} - \Delta \mathrm{P}_{\mathrm{outlet}} - \Delta \mathrm{P}_{\mathrm{accel}}$	17.19 Pa
	Air Channel Friction Factor $f_{air,ACC} = \frac{\Delta P_{channel}}{\frac{1}{2} \cdot \left(\frac{L_{fin,channel}}{D_{hy,fin,channel}} \right) \cdot \overline{\rho}_{air} \cdot V_{air}^{2}}$	0.1514

Discharge Coefficient Calculations

Inputs	Equations	Results
Nozzle Discharge Coefficient Calculations		
$\mathrm{Re}_{nozzle} = 36337$	Predicted Discharge Coefficient $C_D = 1 - 6.92 \cdot \mathrm{Re}_{nozzle}^{-0.5}$	0.9637

APPENDIX B

EQUIPMENT INFORMATION

INSTRUMENTATION:

Instrument Type	*Manufacturer*	*Model*	*Uncertainty*	*Range*
Air-side Instrumentation				
Absolute Pressure	Omega Engineering, Inc.	PX02K1-26A5T	2.5%	88 – 108 kPa
Differential Pressure (nozzle)	Dwyer Instruments, Inc.	607-3	10.0%	0 – 250 Pa
Differential Pressure (test section)	Dwyer Instruments, Inc.	607-3	5.0%	0 – 250 Pa
Temperature	Omega Engineering, Inc.	TT-T-30-SLE	± 0.25°C	10 – 80°C
Relative Humidity	Johnson Controls	HE-67P2-0N00P	2.0%	20 – 80%
Water-side Instrumentation				
Absolute Pressure	Rosemount, Inc.	2088	2.5%	0 – 5515 kPa
Volumetric Flowrate	MicroMotion, Inc.	CMF050	0.2%	0 – 30 Lpm
Temperature (TC)	Omega Engineering, Inc.	TT-T-30-SLE	± 0.25°C	50 – 120°C
Temperature (RTD)	Omega Engineering, Inc.	P-M-A-1/4-9-1/2-PS-12	± 0.12°C	50 – 120°C

DATA ACQUISITION EQUIPMENT:

DAQ Card Type	*Model Number*	*Quantity*
RTD (4-wire)	NI 9216	2

Thermocouple (w/ CJC)	NI 9213	3
Current (± 20 mA)	NI 9203	1
Voltage (± 10 V)	NI 9209	1

HEATED WATER LOOP EQUIPMENT:

Facility Component	*Manufacturer*	*Model Number*
Pump Head	Liquiflo	H7F
Pump Motor	Leeson Motors	C4D17FC42B
Piston Accumulator	Parker	ACP05
Circulation Heater	Watlow	CBDNF29R3S
PID Controller	Watlow	PM6C2CJ
Solid-state Relay (SSR)	Watlow	DB20-24C0

APPENDIX C

ESTIMATION OF HEAT LOSSES

In the calculation of test section heat duties and the validation of an energy balance between the tube-side and the air-side, heat losses from the test facility were not considered, assuming that they would represent a small fraction of the test section heat duty. This assumption is validated here through the estimation of heat losses for a representative data point.

The internal convective heat transfer coefficient was determined using developing flow correlations within an isothermal duct (Shah and London, 1978). To approximate the natural convection heat transfer coefficients on the different faces of the test section, the enclosure surrounding the test section is assumed to be an externally insulated rectangular duct with a height of 0.41 m, width of 0.31 m, and thickness of 0.00254 m. The insulation is assumed to have a constant thickness of 25.4 mm, with a thermal conductivity of 0.06 W m^{-1} K^{-1}. It was assumed that the outer surface of the insulation is exposed to ambient natural convection and radiative exchange with an emissivity equal to 1. The natural convection heat transfer coefficient is calculated using the correlation developed by Elsherbiny *et al.* (2017). While the bottom of the test section sits on a small shelf within the wind tunnel, resulting in conductive losses through the floor, it is assumed that the natural convection and radiative boundary condition is valid on all external surfaces of the test section.

The thermal resistance network between the internal forced air and external ambient environment consists of five resistances, as shown below in a frontal view of the test section enclosure (shown in grey).

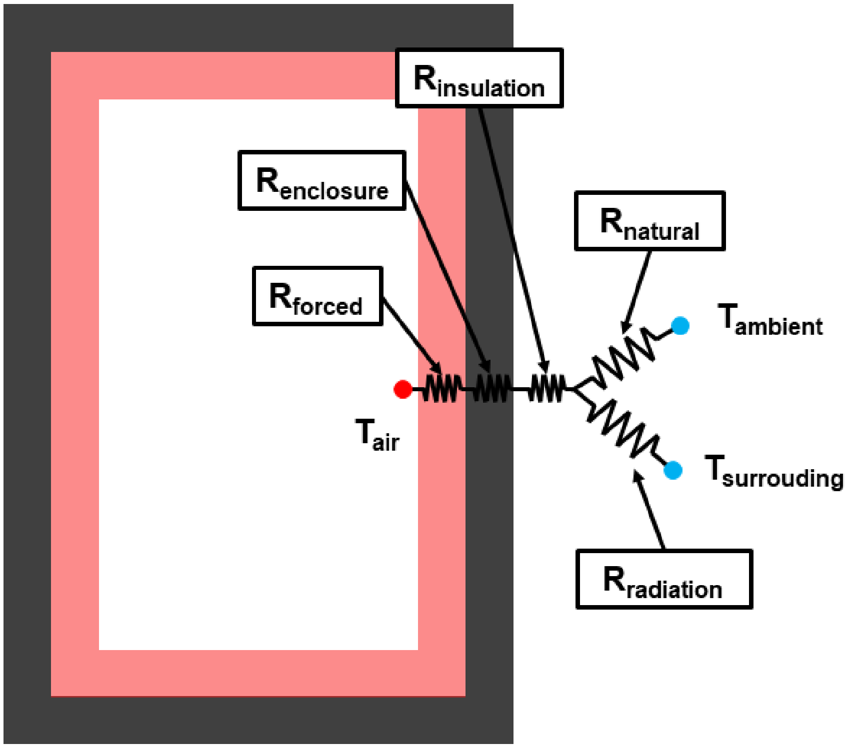

The predicted heat loss from the test section decreases from 24 – 14 W depending on the average air temperature from which heat is being rejected to the environment, where the total measured test section heat duty ranged from 6.14 kW – 8.78 kW. The ambient losses represent less than 0.2 – 0.4% of the measured test section losses, depending on the air-side flow rate and tube-side heat duty. As such, the heat loss is small enough to validate the assumption of negligible heat losses, and the use of tube-side duty to represent the test section heat duty. The following table shows heat loss calculations for a representative data point.

Heat Leakage Calculations		
Inputs	**Equations**	**Results**
$L_{ACC,tube} = 0.4191$ m $W_{enclosure} = 0.315$ m $W_{ACC,tube} = 0.1905$ m $h_{air,in} = 8.234$ W m^{-2} K^{-1} $h_{air,out} = 8.534$ W m^{-2} K^{-1} $h_{air} = 8.379$ W m^{-2} K^{-1} $t_{enclosure} = 0.00254$ m $t_{insulation} = 0.0254$ m $T_{ambient} = 20°C$ $T_{air,average} = 49.87°C$ **Thermophysical Properties:** $k_{insulation} = 0.06$ W m^{-1} K^{-1} $k_{conduction} = 200$ W m^{-1} K^{-1} $\beta_{air} = 0.8986$ K^{-1} $\mu_{film} = 1.85 \times 10^{-5}$ kg m^{-1} s^{-1}	Heat Transfer Area Perpendicular to Heat Flow Path $A_{enclosure} = 2 \cdot \underbrace{\left(L_{ACC,tube} + W_{enclosure}\right)}_{Perimeter} \cdot \underbrace{W_{ACC,tube}}_{Depth}$	0.2797 m^2
	Forced Convection Thermal Resistance $R_{air,forced} = \dfrac{1}{h_{air} \cdot A_{enclosure}}$	0.4267 K W^{-1}
	Enclosure Conduction Thermal Resistance $R_{cond,enclosure} = \dfrac{t_{enclosure}}{K_{enclosure} \cdot A_{enclosure}}$	0.000045 K W^{-1}
	Insulation Conduction Thermal Resistance $R_{cond,ins} = \dfrac{t_{ins}}{K_{ins} \cdot A_{enclosure}}$	1.514 K W^{-1}
	Outer Surface Grashof Number $Gr = \dfrac{g \cdot \beta_{air} \cdot \left(T_s - T_{ambient}\right) \cdot L_{ACC,tube}{}^3}{\left(\mu_{film} / \rho_{film}\right)^2}$	1.032×10^8
	Outer Surface Nusselt Number $Nu_{air,natural} = 0.384 \cdot Gr^{0.252}$	40.16

Heat Leakage Calculations		
Inputs	**Equations**	**Results**
ρ_{film} = 1.18 kg m^{-3} $\varepsilon = 1$	Outer Surface Heat Transfer Coefficient $h_{air,natural} = \frac{Nu_{air,natural} \cdot \overline{K}_{air}}{L_{steam,tube}}$	2.445 W m^{-2} K^{-1}
	Outer Surface Radiative Heat Transfer Coefficient $h_{rad} = \varepsilon\sigma_b \cdot \left(T_{s,K}{}^2 + T_{amb,K}{}^2\right) \cdot \left(T_{s,K} + T_{amb,K}\right)$	6.064 W m^{-2} K^{-1}
	Outer Surface Radiative Thermal Resistance $R_{rad} = \frac{1}{h_{rad} \cdot A_{enclosure}}$	0.5897 K W^{-1}
	Outer Surface Natural Convection Thermal Resistance $R_{air,natural} = \frac{1}{h_{natural} \cdot A_{enclosure}}$	1.415 K W^{-1}
	Ambient Thermal Resistance (combination of natural convection and radiation resistances) $R_{ambient} = \frac{R_{air,natural} \cdot R_{rad}}{R_{air,natural} + R_{rad}}$	0.4162 K W^{-1}
	Total Thermal Resistance $R_{total,loss} = R_{air,forced} + R_{cond,enclosure} + R_{cond,ins} + R_{ambient}$	2.044 K W^{-1}

Heat Leakage Calculations		
Inputs	**Equations**	**Results**
	Outer Surface Temperature $T_s = T_{ambient} + \dot{Q}_{leakage} \cdot R_{ambient}$	31.66°C
	Total Heat Loss Through Enclosure $\dot{Q}_{leakage} = \frac{\left[T_{air,average} - T_{ambient}\right]}{R_{total,enclosure}}$	24 W

REFERENCES

Akhavan-Behabadi, M., R. Kumar and S. Mohseni (2007), "Condensation Heat Transfer of R-134a inside a Microfin Tube with Different Tube Inclinations," *International Journal of Heat and Mass Transfer* Vol. 50(23) pp. 4864-4871

Allen, P. and T. Karayiannis (1995), "Electrohydrodynamic Enhancement of Heat Transfer and Fluid Flow," *Heat Recovery Systems and CHP* Vol. 15(5) pp. 389-423

Argentina, M. and L. Mahadevan (2005), "Fluid-Flow-Induced Flutter of a Flag," *Proceedings of the National academy of Sciences of the United States of America* Vol. 102(6) pp. 1829-1834

Bhatti, M. S. and R. K. Shah (1987). *Handbook of Single-Phase Convective Heat Transfer*. New York, John Wiley and Sons.

Blanco-Marigorta, A. M., M. Victoria Sanchez-Henríquez and J. A. Peña-Quintana (2011), "Exergetic Comparison of Two Different Cooling Technologies for the Power Cycle of a Thermal Power Plant," *Energy* Vol. 36(4) pp. 1966-1972 DOI: http://dx.doi.org/10.1016/j.energy.2010.09.033.

Bury, T. (2012). *Impact of a Medium Flow Maldistribution on a Cross-Flow Heat Exchanger Performance*, INTECH Open Access Publisher.

Bushart, S. (2014). *Advanced Cooling Technologies for Water Savings at Coal-Fired Power Plants*, Cornerstone, Vol. 2017.

Bustamante, J. G., A. S. Rattner and S. Garimella (2015), "Achieving near-Water-Cooled Power Plant Performance with Air-Cooled Condensers," *Applied Thermal Engineering*

Caruso, G. (2005), "Condensation of Steam-Gas Mixtures in Horizontal and Inclined Tubes," Caruso, G., D. Vitale Di Maio and A. Naviglio (2013), "Film Condensation in Inclined Tubes with Noncondensable Gases: An Experimental Study on the Local Heat Transfer Coefficient," *International Communications in Heat and Mass Transfer* Vol. 45 pp. 1-10 DOI: http://dx.doi.org/10.1016/j.icheatmasstransfer.2013.04.010.

Chen, S., F. Gerner and C. Tien (1987), "General Film Condensation Correlations," *Experimental Heat Transfer An International Journal* Vol. 1(2) pp. 93-107

Chen, Y., K.-S. Yang and C.-C. Wang (2002), "An Empirical Correlation for Two-Phase Frictional Performance in Small Diameter Tubes," *International Journal of Heat and Mass Transfer* Vol. 45(17) pp. 3667-3671

Chisholm, D. (1967), "A Theoretical Basis for the Lockhart-Martinelli Correlation for Two-Phase Flow," *International Journal of Heat and Mass Transfer* Vol. 10(12) pp. 1767-1778

Churchill, S. W. (1977), "Comprehensive Correlating Equations for Heat, Mass and Momentum Transfer in Fully Developed Flow in Smooth Tubes," *Industrial & Engineering Chemistry Fundamentals* Vol. 16(1) pp. 109-116

Davies, E. G., P. Kyle and J. A. Edmonds (2013), "An Integrated Assessment of Global and Regional Water Demands for Electricity Generation to 2095," *Advances in Water Resources* Vol. 52 pp. 296-313

Davis, G. (2002), "Comparison of Alternate Cooling Technologies for California Power Plants Economic, Environmental and Other Tradeoffs,"

Dechamps, P. (1996), "Advanced Combined Cycle Alternatives with the Latest Gas Turbines," *ASME 1996 Turbo Asia Conference*, American Society of Mechanical Engineers, pp. V001T004A006-V001T004A006.

Elsherbiny, S. M., M. A. Teamah and A. R. Moussa (2017), "Natural Convection Heat Transfer from an Isothermal Horizontal Square Cylinder," *Alexandria Engineering Journal* Vol. 56(1) pp. 181-187

EPRI (2013). Power Plant Cooling System Overview for Researchers and Technology Developers. EPRI, 3002001915p.

Force, C. A. T. (2003), "The Last Straw: Water Use by Power Plants in the Arid West," *The Hewlett Foundation.* http://tinyurl. *com/LastStrawWater*

Forinash, D. (2015). *Novel Air-Coupled Heat Exchangers for Waste Heat-Driven Absorption Heat Pumps*. Mechanical Engineering, Georgia Institute of Technology, Vol. Master of Science in Mechanical Engineering.

Friedel, L. (1979), "Improved Friction Pressure Drop Correlations for Horizontal and Vertical Two-Phase Pipe Flow," *European two-phase flow group meeting, Paper E*, p. 1979.

Gadhamshetty, V., N. Nirmalakhandan, M. Myint and C. Ricketts (2006), "Improving Air-Cooled Condenser Performance in Combined Cycle Power Plants," *Journal of Energy Engineering* Vol. 132(2) pp. 81-88

Ghiaasiaan, S. M. (2007). *Two-Phase Flow, Boiling, and Condensation: In Conventional and Miniature Systems*, Cambridge University Press.

Go, J. S. (2003), "Design of a Microfin Array Heat Sink Using Flow-Induced Vibration to Enhance the Heat Transfer in the Laminar Flow Regime," *Sensors and Actuators A: Physical* Vol. 105(2) pp. 201-210 DOI: http://dx.doi.org/10.1016/S0924-4247(03)00101-8.

Habib, M. and S. Zubair (1992), "Second-Law-Based Thermodynamic Analysis of Regenerative-Reheat Rankine-Cycle Power Plants," *Energy* Vol. 17(3) pp. 295-301

Hall, G. (1959), "Application of Boundary Layer Theory to Explain Some Nozzle and Venturi Flow Peculiarities," *Proceedings of the Institution of Mechanical Engineers* Vol. 173(1) pp. 837-870

Herrault, F., P. Hidalgo, C.-H. Ji, A. Glezer and M. Allen (2012), "Cooling Performance of Micromachined Self-Oscillating Reed Actuators in Heat Transfer Channels with Integrated Diagnostics," *Micro Electro Mechanical Systems (MEMS), 2012 IEEE 25th International Conference on*, IEEE, pp. 1217-1220.

Hidalgo, P., F. Herrault, A. Glezer, M. Allen, S. Kaslusky and B. S. Rock (2010), "Heat Transfer Enhancement in High-Power Heat Sinks Using Active Reed Technology," *Thermal Investigations of ICs and Systems (THERMINIC), 2010 16th International Workshop on*, IEEE, pp. 1-6.

Hidalgo, P., S. Jha and A. Glezer (2015), "Enhanced Heat Transfer in Air Cooled Heat Sinks Using Aeroelastically Fluttering Reeds," *Thermal Investigations of ICs and Systems (THERMINIC), 2015 21st International Workshop on*, IEEE, pp. 1-6.

Jacobi, A. and R. Shah (1995), "Heat Transfer Surface Enhancement through the Use of Longitudinal Vortices: A Review of Recent Progress," *Experimental Thermal and Fluid Science* Vol. 11(3) pp. 295-309

Jung, D., K.-h. Song, Y. Cho and S.-j. Kim (2003), "Flow Condensation Heat Transfer Coefficients of Pure Refrigerants," *International Journal of Refrigeration* Vol. 26(1) pp. 4-11

Klein, S. (2015), "Engineering Equation Solver," *F-Chart Software, Madison, WI*

Kröger, D. (1998). *Air-Cooled Heat Exchangers and Cooling Tower: Thermal-Flow Performance and Design*. Matieland, South Africa, Dept. of Mechanical Engineering, University of Stellenbosch.

Lin, J. (2016). *Air-Cooled Condensers for Thermoelectric Power Generation*. School of Mechanical Engineering, Georgia Institute of Technology, Vol. Master of Science.

Lin, J., A. Mahvi, T. Kunke and S. Garimella (2016), "Improving Air-Side Heat Transfer Performance in Air-Cooled Power Plant Condensers,"

Lockhart, R. and R. Martinelli (1949), "Proposed Correlation of Data for Isothermal Two-Phase, Two-Component Flow in Pipes," *Chem. Eng. Prog* Vol. 45(1) pp. 39-48

Mahvi, A., A. S. Rattner, J. Lin and S. Garimella (2015), "Steam-Side Pressure Drop and Heat Transfer Characteristics in Air-Cooled Power Plant Condensers and Their Effects on Plant Performance," *ASME International Mechanical Engineering Congress and Exposition*, Houston, Texas

Mahvi, A., A. S. Rattner, J. Lin, T. Kunke and S. Garimella (2016), "Challenges in Predicting Steam-Side Pressure Drop and Heat Transfer Characteristics in Air-Cooled Power Plant Condensers,"

Maulbetsch, J. and M. DiFilippo (2003), "Spray Enhancement of Air Cooled Condensers," *EPRI, Palo Alto, CA, California Energy Commision, Sacramento, CA and Crockett Cogeneration*

Maulbetsch, J. S. and M. N. DiFilippo (2006), "Cost and Value of Water Use at Combined Cycle Power Plants," *California Energy Commission*

Maulbetsch, J. S., M. N. DiFilippo, M. Owen and D. G. Kroger (2010), "Wind Effects on Air-Cooled Condensers for Power Plant Cooling," *2010 14th International Heat Transfer Conference*, American Society of Mechanical Engineers, pp. 809-816.

Maupin, M. A., J. F. Kenny, S. S. Hutson, J. K. Lovelace, N. L. Barber and K. S. Linsey (2014). Estimated Use of Water in the United States in 2010. US Geological Survey, 2330-5703p.

Mortensen, K. (2011). Improved Performance of an Air Cooled Condenser (Acc) Using Spx Wind Guide Technology at Coal-Based Thermoelectric Power Plants, 47 p.

Shah, M. (1979), "A General Correlation for Heat Transfer During Film Condensation inside Pipes," *International Journal of heat and mass transfer* Vol. 22(4) pp. 547-556

Shah, R. and A. London (1978). *Laminar Flow Forced Convection in Ducts: A Sourcebook for Compact Heat Transfer Exchange Analytical Data*, Academic Press.

Shah, R. K. and M. S. Bhatti (1987), "Laminar Convective Heat Transfer in Ducts," *Handbook of single-phase convective heat transfer* Vol. 3

Shah, R. K. and A. L. London (1971). Laminar Flow Forced Convection Heat Transfer and Flow Friction in Straight and Curved Ducts-a Summary of Analytical Solutions. DTIC Documentp.

Sohal, M. and J. O'Brien (2001), "Improving Air-Cooled Condenser Performance Using Winglets and Oval Tubes in a Geothermal Power Plant," *Geothermal resources council transactions* Vol. 25(26-29) pp. 1-7

SPX (2015). *Air Cooled Condensers*, SPX Corporation.

Steinke, M. E. and S. G. Kandlikar (2004), "Single-Phase Heat Transfer Enhancement Techniques in Microchannel and Minichannel Flows," *ASME 2004 2nd International*

Conference on Microchannels and Minichannels, American Society of Mechanical Engineers, pp. 141-148.

Torii, K., K. Kwak and K. Nishino (2002), "Heat Transfer Enhancement Accompanying Pressure-Loss Reduction with Winglet-Type Vortex Generators for Fin-Tube Heat Exchangers," *International Journal of Heat and Mass Transfer* Vol. 45(18) pp. 3795-3801

World Nuclear Association (2016). *Cooling Power Plants*. W. N. Associatoin.

Yang, L., Y. Asako, Y. Yamaguchi and M. Faghri (1997), "Numerical Prediction of Transitional Characteristics of Flow and Heat Transfer in a Corrugated Duct," *Journal of heat transfer* Vol. 119(1) pp. 62-69

Zhai, H. and E. S. Rubin (2010), "Performance and Cost of Wet and Dry Cooling Systems for Pulverized Coal Power Plants with and without Carbon Capture and Storage," *Energy Policy* Vol. 38(10) pp. 5653-5660